UC San Diego
UC San Diego Electronic Theses and Dissertations

Title
An advanced gray-scale technology and its applications to micro-devices

Permalink
https://escholarship.org/uc/item/8sc77714

Author
Zhou, Zhou

Publication Date
2009

Peer reviewed|Thesis/dissertation

eScholarship.org Powered by the California Digital Library
University of California

UNIVERSITY OF CALIFORNIA, SAN DIEGO

An Advanced Gray-Scale Technology and Its Applications to Micro-Devices

A dissertation submitted in partial satisfaction of the

requirements for the degree Doctor of Philosophy

in

Electrical Engineering (Photonics)

by

Zhou Zhou

Committee in charge:

Professor Sing H. Lee, Chair
Professor Yeshaiyahu Fainman
Professor Andrew C. Kummel
Professor Yu-Hwa Lo
Professor Frank E. Talke

2009

Copyright

Zhou Zhou, 2009

All rights reserved.

The dissertation of Zhou Zhou is approved, and it is acceptable in quality and form for publication on microfilm and electronically:

____

____

____

____

____

Chair

University of California, San Diego

2009

To

My Family

Table of Contents

Signature Page…………………………………………………………iii

Dedication……………………………………………………………...iv

Table of Contents………………………………………………………v

List of Figures…………………………………………………………viii

List of Tables…………………………………………………………..xi

Acknowledgements……………………………………………………xii

Vita………………………………………………………………………xiii

Publications and Pending Patent Applications……………………………...xiv

Abstract of the Dissertation.…………………………………………..xvii

1. Introduction ……………………………………………………….......1
   1.1 Motivations of gray-scale lithography…………………………………....1
   1.2 HEBS mask and binary half-tone (BHT) mask …………………………4
      1.2.1 HEBS gray-scale mask…………………………………………..4
      1.2.2 Binary half-tone (BHT) mask……………………………………6
   1.3 Improved carbon-based gray-scale mask…………………………………8
      1.3.1 Introduction of the improved carbon-based gray-scale mask………8
      1.3.2 Larger optical density at shorter wavelength (DUV range)……….10
      1.3.3 Higher resolution capacity by using shorter wavelength………….10
   1.4 Comparison of HEBS, BHT and our new gray-scale masks……………11
   1.5 Latest developments of gray-scale technologies and applications……...12
   1.6 E-beam systems used in this dissertation………………………………..25
   1.7 Structure of the dissertation……………………………………………..26

2. Material and process of improved gray-scale mask………………………...27
   2.1 Motivations of improved gray-scale technology………………………..27
   2.2 New mask material for improved gray-scale technology……………….28
   2.3 Fabrication process of new gray-scale mask…………………………...28
   2.4 Conclusion……………………………………………………………33

3. Two-beam-current method for e-beam writing gray-scale masks and its application to high-resolution micro-structures……………………………..34
3.1 Introduction……………………………………………………………...34
3.2 The two-beam-current method of writing gray scale masks……………37
3.2.1 Dynamic range increase for gray-scale mask……………………..39
3.2.2 Writing time reduction for gray-scale mask………………………41
3.2.3 Criteria for choosing the two currents…………………………….44
3.3 Gray-scale mask fabrication ……………………………………………45
3.3.1 E-beam resist and its preparation…………………………………45
3.3.2 E-beam writing process and ZEP7000A resist development……..46
3.3.3 Dry etching for gray-scale mask…………………………………..47
3.3.4 Experimental results………………………………………………48
3.4 Fabricating micro-optical devices……………………………………….51
3.4.1 The optical lithography process…………………………………...52
3.4.2 Dry-etching for fabricating optical devices……………………….54
3.4.3 Experimental results………………………………………………55
3.5 Discussions……………………………………………………………...59
3.5.1 The effect of recalibration of e-beam system required by the two-current method on writing time reduction……………………59
3.5.2 Alignment and stitching issues in using two-beam-current Method……………………………………………………………60
3.5.3 The effects of the accuracy of e-beam clock frequency on dynamic range…………………………………………………63
3.5.4 Extension to three-beam-current method …………………………64
3.6 Conclusion………………………………………………………………64

4. Applications of improved gray-scale technology to micro-devices with deep structures………………………………………………………66
4.1 Introduction……………………………………………………………...66
4.2 Device design……………………………………………………………73
4.3 Device Fabrication………………………………………………………76
4.3.1 The optical lithography process…………………………………...77
4.3.2 Dry-etching process……………………………………………….80
4.4 Experimental results and discussions…………………………………...82
4.4.1 Device fabricated………………………………………………….82
4.4.2 Comparison of device shape to design……………………………87
4.4.3 Potential application of our new gray-scale technology in MEMS devices……………………………………………………89
4.5 Conclusion………………………………………………………………89

5. Review of other research ideas and progress in this project………………..91
5.1 LIGA Process and LIGA-like Process…………………………………91

5.1.1 Deep X-ray Lithography and Mask Technology…………………….92
5.1.2 Electro-deposition…………………………………………………93
5.1.3 Plastics Molding…………………………………………………..93
5.1.4 Existing LIGA-like Process in PIDC…………………………...94
5.1.5 Proposed LIGA-like Process for Deep Gray-scale Devices………95
5.1.6 Brief Review of Latest Progress and Applications of Laser LIGA-like process……………………………………………...96
5.2 Asymmetric Resonant Cavity (ARC) Device………………………….101
5.2.1 Overview of Concept of Asymmetric Resonant Cavity (ARC)…101
5.2.2 Proposed ARC Structures to Be Fabricated Using Gray-Scale Technology…………………………………………………………102

6. Discussions and summary…………………………………………………107
6.1 Differences between gray-scale and binary technologies……………...107
6.1.1 E-beam lithography……………………………………………...107
6.1.2 Mask fabrication…………………………………………………108
6.1.3 Optical lithography………………………………………………109
6.1.4 Dry etching in device fabrication………………………………..109
6.1.5 Wavelength of optical lithography………………………………109
6.2 Issues of surface quality of devices in gray-scale technology…………110
6.3 Review of dry etching techniques and progress for deep structures in Si/SiO_2…………………………………………………………………113
6.4 Future/further development of our technology and applications………126

Appendices……………………………………………………………….........129

Appendix A Reprint of “Fabrication of an improved gray-scale mask for refractive micro- and meso-optics”……………...129

Appendix B Reprint of “Two-beam-current method for e-beam writing gray-scale masks and its application to high-resolution micro-structures”…………………………132

Appendix C Experimental Details: E-beam writing job file and clock files …………………………………………………141

References…………………………………………………………………...155

List of Figures

Figure 1.1 Comparison of binary and gray-scale technologies…………………..2

Figure 1.2 The process of fabricating a lens by reflowing resist…………….......3

Figure 1.3 Illustration of binary half-tone (BHT) mask……………………….....6

Figure 1.4 Fabrication process of the gray-scale mask……………………….....8

Figure 1.5 Optical density comparison for HEBS and LAF…………………....10

Figure 2.1 Axicon in LAF measured by atomic force microscopy………….....30

Figure 2.2 (a) Actual transmission compared to the designed LAF thickness….31

Figure 2.2 (b) Transmission comparisons between the designed and the fabricated gray-scale steps on the mask…..……………………..32

Figure 3.1 Illustration of two-beam-current method of e-beam writing………..35

Figure 3.2 The exposure characteristic of ZEP 7000A e-beam resist is shown in the dotted line. Also shown is the comparison of dosage dynamic range between single current I_s and two currents I_1 and I_2…………37

Figure 3.3 Time saving for the two-beam-current method calculated from the online Parameter Calculator (provided by IBM [2]) for Leica VB-6HR e-beam system. The slope of the line in this figure is about 1.3 min/mm^2. ……………………………………….......43

Figure 3.4 The measured depth profiles of the calibration steps in the e-beam resist. The depths at step #64 are about 510nm and 400nm for two-current and single-current method respectively………………..49

Figure 3.5 Optical densities of the calibration steps at 248nm. The maximum optical densities (at step #64) achieved in two-current and single-current methods are 3.02 and 2.30 respectively……………...50

Figure 3.6 The fabrication processes of high-resolution micro-devices using our improved gray-scale masks……………………………….51

Figure 3.7 Exposure characteristic of PMGI-SF11 resist……………………….54

Figure 3.8 SEM picture showing a resolution of 0.2 micron in UV5 by 248nm lithography…………………………………………………….56

Figure 3.9 AFM picture of a portion of an off-axis Fresnel lens on quartz ……57

Figure 3.10 An AFM picture of a 3-D topographic map on LAF………………..58

Figure 3.11 (a) Microscopic pictures of axicons on the gray-scale mask………..61

Figure 3.11 (b) The microscopic pattern on PMGI resist ……………………….62

Figure 4.1 Spherical aberration of a normal spherical lens……………………..68

Figure 4.2 Comparison of a normal spherical lens (lower) and an aspheric lens (upper) with zero spherical aberration…………………………69

Figure 4.3 Working principle of a 2-dimentional retro-reflector……………….70

Figure 4.4 A 3-dimentional retro-reflector (also called corner-cube, corner-reflector)…………………………………………………71

Figure 4.5 Via/Pad structures in a typical multi-layer PCB board……………..72

Figure 4.6 A smooth surface with a slope of H/W can be approximated by many quantized steps. Its surface roughness X can be calculated as a function of H, W and the number of quantized steps (N)………74

Figure 4.7 The relationship between the theoretic surface roughness X and the number of gray levels……………...………………………..75

Figure 4.8 Flow chart of the procedure for fabricating gray-scale devices.........77

Figure 4.9 Exposure characteristic of Shipley photoresist SPR 220-3.0……….79

Figure 4.10 SEM picture of a parabolic lens fabricated in silicon………………82

Figure 4.11 SEM picture of a retro-reflector array………………………………83

Figure 4.12 SEM picture of a retro-reflector……………………………………84

Figure 4.13 Picture of the retro-reflector structure on mask……………………..85

Figure 4.14 SEM picture of a via/pad structure………………………………….86

Figure 4.15 (a) Comparison of fabricated aspheric lens shape to the design……87

Figure 4.15 (b) Cross-correlation of fabricated aspheric lens shape to designed. 88

Figure 5.1 Micro optical reflectors for ARCs…………………………………104

Figure 5.2 A collection of the proposed 3D oval or stadium-shape cross-section ARCs and gray-scale-side wall photonics components…...106

Figure 6.1 Effects of under-etching and over-etching of gray-scale mask……108

List of Tables

Table 1.1 Comparison of different masks…………………………………………...12

Table 3.1 Processing parameters of UV5 resist………………………………..53

Table 3.2 Processing parameters of PMGI-SF11 resist………………………..53

Table 3.3 Parameters for etching PMGI into quartz…………………………...55

Table 4.1 Processing parameters of SPR220-3.0 resist………………………..78

Table 4.2 ICP-RIE Etching parameters used to obtain the etch ratio of 5:1 between silicon and SPR 220-3.0 resist………………………...81

Acknowledgements

This dissertation would not be possible without the help and encouragement of many people. I owe greatest appreciation to my advisor, Prof. Sing H. Lee, who firmly supported me during the course of this research. My success is from the encouragement, guidance and wisdom that he provided to me throughout my entire graduate study. Appreciation also goes to my committee members: Professor Yeshaiyahu (Shaya) Fainman, Professor Yu-Hwa Lo, Professor Andrew C. Kummel and Professor Frank E. Talke for providing helpful suggestions and other perspectives related to this work.

Thanks to all of these colleagues and friends for their generous help to me in these days: Rong Liu, Christian Chovino, Yumin Chen, Mike Jin, Samhita Dasgupta, Joseph Ford, Silvanus. S. Lau, Bernard Kress, Alan Bleier, David Spencer, Matthew Banet, James Yu, and many others.

Finally I owe enormous gratitude to my parents, wife and two sons. Without their endless love and support, I could not achieve this step.

Appendix A, in full, is a reprint of the material as it appears in Optics Letters, Vol. 29 (5), 2004. Appendix B, in full, is a reprint of the material as it appears in Applied Optics, Vol. 47 (19), 2008. The dissertation author was the first author of these two papers.

Vita

1989	B.S., Electronic Engineering, Southeast University, China
1989-1999	Assistant Research Professor and then Associate Research Professor, Institute of Semiconductors, Chinese Academy of Sciences, China
1999-2005	Graduate Student Researcher and Teaching Assistant, University of California, San Diego
2001	M.S., Electrical Engineering (Photonics), University of California, San Diego
2003	Research Intern, GE Global Research Center, Niskayuna, New York
2005-present	Senior Scientist, Triage Wireless Inc., San Diego, California
2009	Ph.D., Electrical Engineering (Photonics), University of California, San Diego

Publications

Zhou Zhou and Sing H. Lee, "Two-beam-current method for e-beam writing gray-scale masks and its application to high-resolution micro-structures", Applied Optics, Vol. 47 (17), pp.3177-3184 (2008)

Zhou Zhou and Sing H. Lee, "Fabrication of an improved gray-scale mask for refractive micro- and meso-optics", Optics Letters, Vol. 29 (5), pp.457-458 (2004)

Pending Patent Applications

Sing H. Lee and Zhou Zhou, "Two-beam-current method of e-beam writing of gray-scale mask for manufacturing multi-level micro-structures", USA patent application under preparation, UCSD Docket No.SD2008-287

Zhou Zhou and Matthew Banet, "Adjustable cuff for measuring blood pressure", U.S.S.N. 60/984,424, filed on 11/01/2007

Matthew Banet and Zhou Zhou, "Patch sensor for measuring vital signs", U.S.S.N. 11/930,881, filed 10/31/2007

Marshal Dhillon, Zhou Zhou, Matthew Banet, Robert Kopotic, Andrew Terry, Henk Visser and Kenneth Hunt "Vital sign monitor for measuring blood pressure using optical, electrical, and pressure waveforms", U.S.S.N. 60/983,198, filed on 10/28/2007

Matthew Banet, Zhou Zhou, Robert Kopotic, Marshal Dhillon, Andrew Terry and Henk Visser, "Device and method for determining respiratory rate", U.S.S.N. 60/949,052, filed on 7/11/2007

Matthew Banet, Zhou Zhou, Kenneth Hunt and Henk Visser, "Body-worn sensor featuring a low-power processor and multi-sensor array for measuring blood pressure", U.S.S.N. 60/946,036, filed on 6/25/2007

Matthew Banet, Zhou Zhou, Kenneth Hunt and Henk Visser, "Multi-sensor array for measuring blood pressure", U.S.S.N. 60/943,660, filed on 6/13/2007

Matthew Banet, Zhou Zhou, Robert Kopotic, Marshal Dhillon and Andrew Terry, "Vital sign monitor for cufflessly measuring blood pressure using a pulse transit time corrected for vascular index", U.S.S.N. 60/943,523, filed on 6/12/2007

Matthew Banet, Zhou Zhou, Robert Kopotic, Marshal Dhillon and Andrew Terry, "Device and method for determining blood pressure using 'hybrid' pulse transit time measurement", U.S.S.N. 60/943,464, filed on 6/12/2007

Zhou Zhou, Marshal Dhillon, Henk Visser, Andrew Terry and Matthew Banet, "Vital sign monitor for cufflessly measuring blood pressure without using an external calibration", U.S.S.N. 11/682,228, filed on 3/05/2007

Zhou Zhou, Marshal Dhillon, Henk Visser, Andrew Terry, Matthew Banet, Kenneth Hunt and Adam Fleming, "Monitor for measuring vital signs and rendering video images", U.S.S.N. 11/682,177, filed on 3/05/2007

Matthew Banet, Zhou Zhou and Kenneth Hunt, "Two-part patch sensor for monitoring vital signs", U.S.S.N. 11/558,538, filed on 11/10/2006

Matthew Banet, Michael Thompson and Zhou Zhou, "Blood pressure monitor", U.S.S.N. 11/530,076, filed on 9/08/2006

Matthew Banet, Michael Thompson, Zhou Zhou, Henk Visser, Adam Fleming, Marshal Dhillon and Andrew Terry, "Hand-held vital sign monitor", U.S.S.N. 11/470,708, filed on 9/07/2006

Matthew Banet, Michael Thompson, Zhou Zhou and Henk Visser, "Bilateral device, system and method for monitoring vital signs", U.S.S.N. 11/420,744, filed on 5/27/2006

Matthew Banet, Michael Thompson, Zhou Zhou, Henk Visser and Kenneth Hunt, "System for measuring vital signs using bilateral pulse transit time", U.S.S.N. 11/420,652, filed on 5/26/2006

Matthew Banet, Michael Thompson, Zhou Zhou and Henk Visser, "Bilateral device, system and method for monitoring vital signs", U.S.S.N. 11/420,281, filed on 5/25/2006

Zhou Zhou, Michael Thompson and Matthew Banet, "System for measuring vital signs using an optical module featuring a green light source", U.S.S.N. 11/307,375, filed on 2/03/2006

Matthew Banet, Michael Thompson and Zhou Zhou, "Chest strap for measuring vital signs", U.S.S.N. 11/306,243, filed on 12/20/2005

Matthew Banet and Zhou Zhou, "Hand-held monitor for measuring vital signs", U.S.S.N. 11/162,742, filed on 9/21/2005

Matthew Banet and Zhou Zhou, "Patch sensor for measuring vital signs", U.S.S.N. 11/160,957, filed 7/18/2005

ABSTRACT OF THE DISSERTATION

An Advanced Gray-scale Technology and Its Applications to Micro-Devices

by

Zhou Zhou

Doctor in Philosophy in Electrical Engineering (Photonics)
University of California, San Diego, 2009

Professor Sing H. Lee, Chair

This dissertation introduces a kind of new gray-scale technology. The new gray-scale technology uses a carbon-based light-attenuating material. This material can reach a very high optical density (~3.0) for deep ultraviolet (DUV) lithography applications. This property is out the reach of the often-used High-Energy-Beam-Sensitive (HEBS) gray-scale mask. HEBS gray-scale mask cannot be used for wavelength below 300 nm and it cannot provide enough optical density at wavelengths shorter than 350 nm for high-resolution component fabrication. Higher optical density at shorter wavelengths means that the components of more levels and with higher resolution are achievable. Compared with Binary Half-Tone (BHT) gray-scale mask, the new mask offers a much higher resolution.

Two-beam-current method is invented for the e-beam writing in the fabrication of gray-scale masks. Compared with the simpler single-current method,

two-beam-current method offers two important advantages. First it can achieve a much larger dynamic range for the e-beam exposure. The second advantage is the writing time for a gray-scale mask could be reduced significantly when a large pattern is to be written.

By applying the new gray-scale mask in DUV and UV lithography respectively, gray-scale patterns were successfully generated in optical resists. Finally devices were fabricated after the gray-scale patterns in resists were transferred into the substrate material in the etching step. Different micro-structures with different resolution and depth requirements have been fabricated successfully.

The carbon-based material has a big hardness, comparable to diamond film, and stays at the quartz surface very firmly. The life time of the mask is comparable to the normal chrome mask used in semiconductor industry, and thus pretty long. This new gray-scale technology could also lead to lower-cost mass production of higher quality micro- and meso-scale micro-devices in different substrates, e.g. quartz and silicon et al..

1. Introduction

This dissertation documents the development of an improved gray-scale technology and the applications of this technology to various micro-devices. The motivations of developing gray-scale technology are presented in Section 1.1. In Section 1.2, two often-used gray-scale mask technologies are reviewed. In Section 1.3 our improved gray-scale mask, based on a new carbon attenuation material, is introduced briefly. In section 1.4 a comparison between our mask and other two masks is presented. Other latest developments of gray-scale technology are reviewed briefly in Section 1.5. In Section 1.6 the two different e-beam systems used in this dissertation are explained. At the end of this introduction chapter, the structure of this dissertation is presented briefly.

1.1 Motivations of gray-scale technology

To fabricate micro-devices of many phase levels with traditional binary masking techniques, multiple masks must be used, and multiple alignments, exposures and processing steps must be performed [1, 2]. This technique needs N masks and N processing steps to achieve 2^N gray levels, so a high production cost would come from the need for the multiple lithography and processing steps. Misalignments between masks and between lithography steps also lead to

degradation in resolution. Consequently an improved process based on gray-scale masks was developed. Gray-scale photolithography process allows the fabrication of an N-level profile by using only one single mask and one single processing step [3, 4, 5, and 6]. Alignment error is thus avoided and fabrication cost becomes lower.

Figure 1.1 illustrates the differences between binary lithography and gray-scale lithography. The binary lithography, on the left, is often used for fabricating normal MEMS, semiconductor devices and other micro-devices with binary/rectangular profiles. The 4-level gray-scale mask, shown on right side, is used to produce a 4-level structure in one single lithography step.

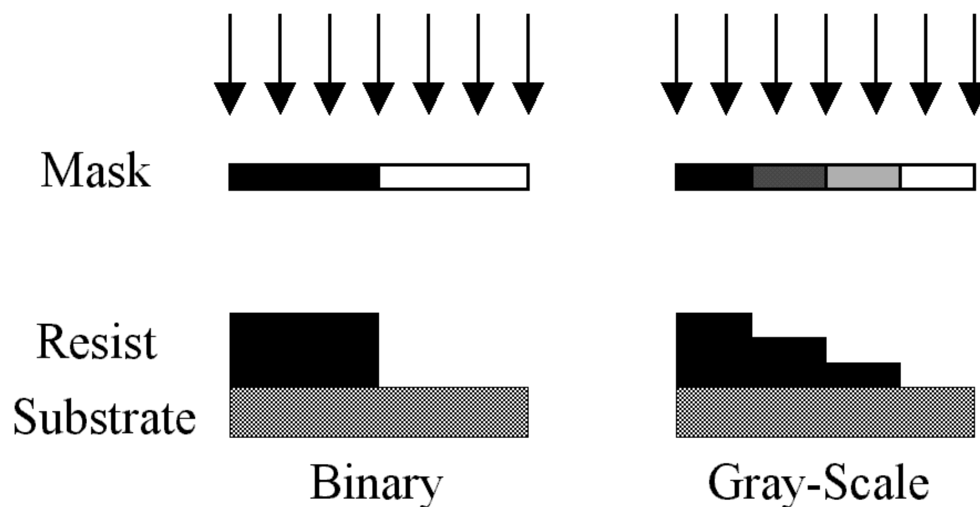

Figure 1.1 Comparison of binary and gray-scale technologies

Very often, the addition of more levels to closely approximate an analog contour is a prerequisite for many devices, such as refractive optical devices and some analog MEMS devices, which require a smooth surface profile. For diffractive optical elements (DOE), the addition of more levels will enhance the performance of diffractive optical elements (DOEs) because the efficiency (η) of a DOE increases with the number (N) of phase-levels according to the following relation:

$$\eta=\mathrm{sinc}^2(\pi/N) \tag{1.1}$$

When N increases from 4 to 8, the theoretical efficiency η will increase from 81% to 95%, approximately.

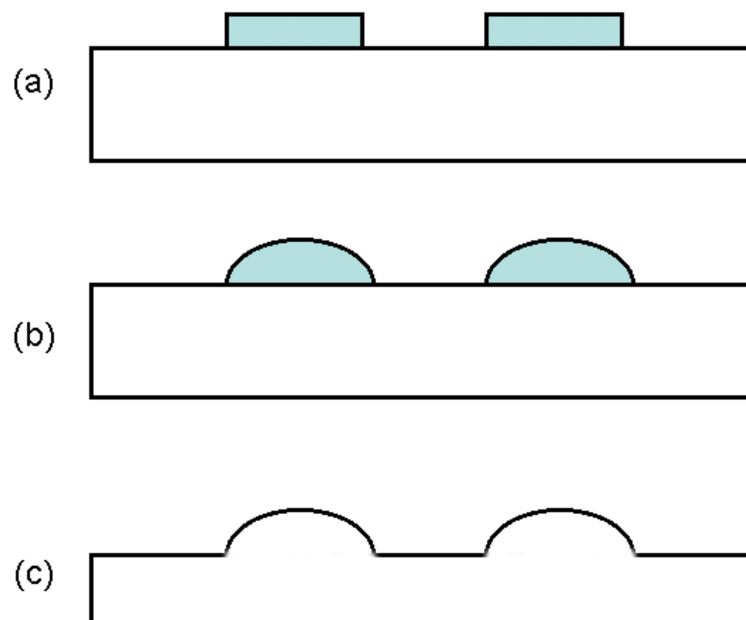

Figure 1.2 The process of fabricating a lens by reflowing resist

Sometimes, reflowing (melting) resist can be used for the manufacturing of some mostly spherical shape structure, such as a spherical lens [7]. Figure 1.2 illustrates the process of this technology. Figure 1.2(a) shows the resist (in blue color) pads on a substrate, fabricated in a standard lithograph step. Figure 1.2 (b) shows the spherical shape of the melted/reflowed resist. Typically the reflowing temperature in this step is about 100 to 200 degrees centigrade. Figure 1.2 (c) shows the fabricated spherical lens in substrate. The lens is fabricated after the reflowed resist (shown in Fig. 1.2 (b)) is transferred into the substrate in an etching step. This technique is restricted to a very limited range of shapes (mainly spherical, due to the surface tension of liquid) and is not a methodology that can be used for fabrication of structures with arbitrary shape.

1.2 HEBS gray-scale mask and binary half-tone (BHT) mask

1.2.1 HEBS gray-scale mask

High-Energy-Beam-Sensitive (HEBS) glass was used in some experiments as the gray scale mask material [3, 4]. HEBS glass is a glass made of a low expansion zinc-borosilicate. This glass contains alkali to facilitate ion exchange reactions that make the glass sensitive to high-energy beams, electron or laser beams. The ion exchange process is carried out long enough to cause silver ions to diffuse into the

glass to a depth of up to 3 microns. This process is conducted at a temperature above 320 degrees centigrade, and silver-alkali-halide containing complex crystals is formed. Chemical reaction to produce opaque regions of silver atoms is achieved by exposing the glass to high-energy beams, i.e., more than 100 kV electron beams. So the principle behind this kind of mask is that HEBS glass changes its opacity when exposed to a beam of high-energy electrons or laser. For example, gray-scale masks may be generated in electron beam writer by varying the dosage of electrons striking different areas of a HEBS glass plate. HEBS gray-scale mask cannot provide enough optical density at wavelengths shorter than 350 nm for high-resolution component fabrication and it is even not applicable when wavelength is below 300 nm because of the intrinsic property of HEBS glass.

1.2.2 Binary half-tone (BHT) mask

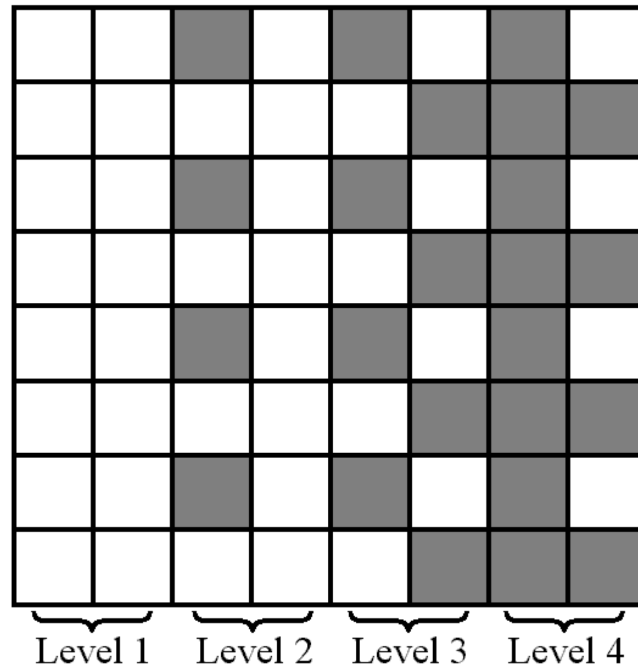

Figure 1.3 Illustration of binary half-tone (BHT) mask

Figure 1.3 illustrates the design of binary halftone (BHT) mask [8, 9]. For this 4-level mask, each gray-scale level has 4 resolution elements and each gray-scale resolution element has 2x2=4 square cells. In level 1, 2, 3 and 4, the numbers of clear cells in each resolution element are 4, 3, 2 and 1 respectively. The principle behind this kind of mask is that, by varying the ratio between the number of opaque cells and the number of clear cells, the transmission intensity of the mask can be modulated. A state of the art halftone chrome mask may consist of mixtures of 0.5 x 0.5 micron^2 chrome cells that are totally opaque, and 0.5 x 0.5 micron^2 clear cells

that are totally transparent. The transmittance of a gray level in a halftone chrome mask is determined by the ratio of the number of opaque cells to clear cells within a gray scale resolution element.

This BHT mask is very easy to be fabricated because its fabrication process is the same as that for normal masks used in the integrated circuit (IC) industry. It is not wavelength-selective, which means it can be used for lithography tool at any wavelength. But one main disadvantage of BHT mask is its low-resolution capability. Theoretically the resolution of the BHT mask is limited by the size of each cell when the cell size is resolvable by the lithography tool. So far the best resolution of the pattern, fabricated by the use of BHT mask, is about 0.5 micron, which is close to the applied wavelength of the lithography tool.

In theory the total number of levels that BHT mask can accommodate is equal to the number of cells in a resolution element plus one. For the mask shown in Figure 1.3, the total umber of square cells in one resolution element is 4, so the maximum number of levels that it can accommodate is 5. The possible 5th level, whose 4 cells are all opaque, is not shown in the figure.

Because of limits of the low resolution and the maximum number of levels, there exists a minimum size limitation for patterns by BHT technology. For example for a spherical lens, if 33 levels are used for the mask design, then the minimum base

radius of the lens will be (33 x 0.5) micron = 16.5 microns. This means, in some cases, BHT technology is not suitable for the fabrication of very small refractive micro-optics.

1.3 Improved carbon-based gray-scale mask

1.3.1 Introduction of the improved carbon based gray-scale mask

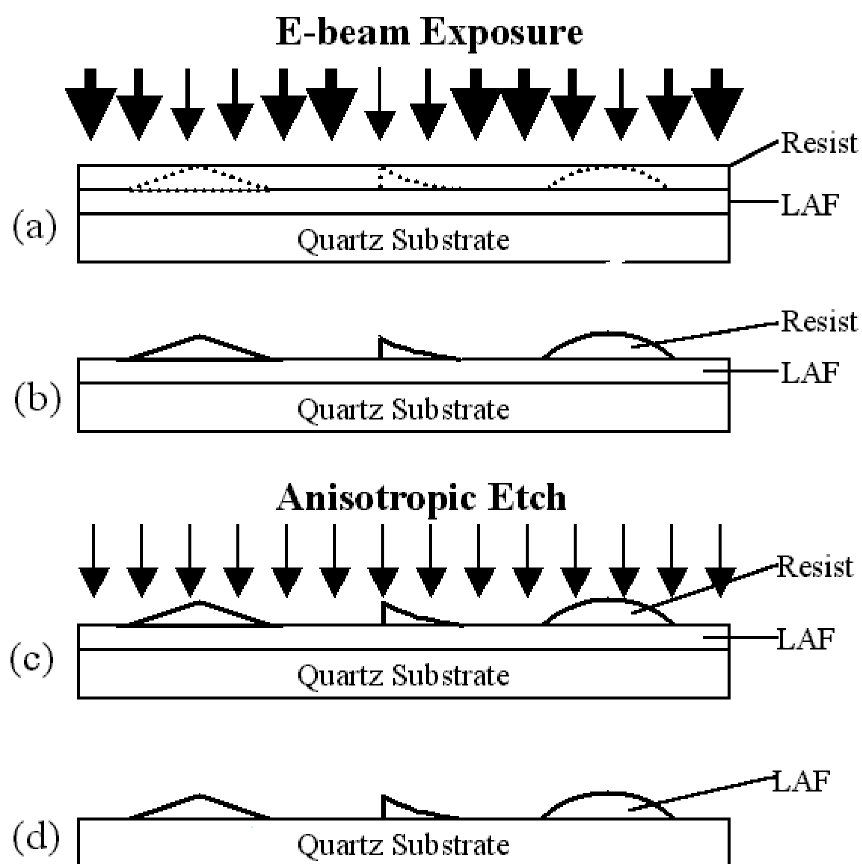

Figure 1.4 Fabrication process of the gray-scale mask

Figure 1.4 shows the schematic fabrication process of our new gray-scale mask [10]. An e-beam writer was used to write gray-scale patterns on the ZEP7000A e-beam resist (shown in Figure 1.4(a). After exposing the /ZEP/LAF/Quartz plate in the e-beam writer, the resist was developed in ZED750 developer. The profile shown in Figure 1.4(b) is obtained in this step. The developed resist pattern was then transferred into the light-attenuating film (LAF) by an anisotropic etching using a dry etching system, as shown in Figure 1.4(c). The dry etching system can be Chemically Assisted Ion Beam Etching (CAIBE), Reactive Ion Etching (RIE) or Inductive Coupled Plasma Reactive Ion Etching (ICP-RIE). Final mask is fabricated after the etching is completed and it is shown in Figure 1.4(d). The transmittance of the new gray-scale mask is related to LAF thickness d as $\exp[-\kappa d]$, where κ is the absorption coefficient of LAF. The carbon-based material has a big hardness comparable to diamond film and stays at the quartz surface very firmly. The mask can be used in contact aligner repeatedly, as a normal chrome mask is. The life time of the new mask is comparable to the normal chrome mask, and is thus long.

1.3.2 Larger optical density at shorter wavelength (DUV range)

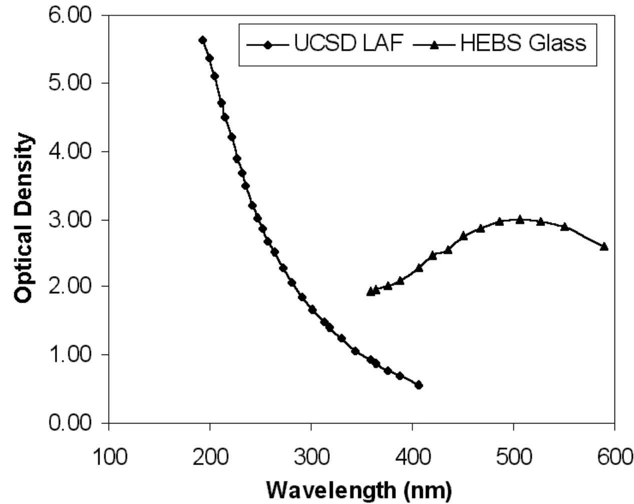

Figure 1.5 Optical density comparison for HEBS and LAF

As compared in Figure 1.5, our new gray-scale mask, which utilizes the new Light-Attenuation Film (LAF), shows a higher optical density than HEBS mask when wavelength is below 300 nm [10]. The shorter the wavelength is, the bigger the optical density of our LAF will be. Because of the higher optical density of LAF, the new gray-scale mask can accommodate more phase levels than that HEBS mask can, while it has no the minimum size limitation that exists in BHT technology.

1.3.3 Higher resolution capacity by using shorter wavelength

E-beam writing system was used for the fabrication of our new mask. So the resolution of the patterns in the new mask is limited by the resolution capability of e-

beam resist and it can reach even better than 0.1 micron, which is much better than that is achieved by BHT mask (0.5 micron). Theoretically, the resolution of the patterns in the new mask could also be affected by the e-beam size of the e-beam writing system. But usually the beam size of the e-beam system is much less than 0.1 micron. So in practical, the resolution of patterns in our carbon-based gray-scale mask is mainly limited by the e-beam resist. For the e-beam resist (ZEP7000A), which is used in this dissertation, the resolution capability can reach as low as 0.1 micron.

1.4 Comparison of HEBS, BHT and our new gray-scale masks

Table 1.1 shows the comparison of the three masks mentioned above. Resolution, optical density (OD), wavelength range and fabrication difficulty are compared for all three masks together. From this table we can conclude that our improved mask offers the best resolution, optical density and wavelength range, while the fabrication difficulty is compatible to that for HEBS glass.

Table 1.1 Comparison of different masks

	Resolution	OD	Wavelength	Fabrication
BHT	low	low	Non-sensitive	easy
HEBS	medium	medium	▪ Sensitive ▪ Not work for 300 nm or less	difficult
UCSD	high	high	▪ Sensitive ▪ Work for all wavelengths	difficult

1.5 Latest developments of gray-scale technologies and applications

Current three dimensional (3D) photolithography technologies can be divided into three primary groups: multiple-step [1-2], direct-write, and grayscale mask photolithography. Each photolithography technique has advantages and disadvantages that make it suited for different applications.

A general process of fabricating gray-scale devices is employing one of the three gray-scale masks, which are mentioned in 1.4, in a lithography step. After gray-scale profile is generated in the resist layer, a dry etching process will be used to transfer the gray-scale profile into the substrate (Quartz, Silicon et al.). Some groups used photosensitive hybrid glass material, instead of ordinary resist, in the

lithography step [11]. The hybrid glass is based on sol-gel synthesis technique. When gray-scale patterns are generated on this kind of glass material in the lithography step, a baking step is used to cure the hybrid glass. The final optical lens is done thereby. This technology eliminates the need for the final dry etching step, so it will reduce equipment demands and costs, speed up the fabrication and shorten the process cycle. Any one of the three masks mentioned above can be used in the lithography process of this hybrid glass and the advantages of our improved gray-scale mask still stand. The disadvantage of this technology is the device material can not change.

Laser direct-writing (LDW) technology can also be used to fabricate gray-scale devices [12, 13]. This is a mask-less gray-scale technology and it can create gray-scale structures directly on UV-sensitive materials, such as polymer, by burning the exposed material off under high-power laser beam. LDW photo-tool has been developed by modulating a UV laser spot, which is focused by a microscope objective. Three dimensional (3D) pattern writing, or multilevel gray-scale topography, can be achieved by modulating the intensity of the beam to expose the resist/polymer partially. This technology eliminates the need of fabricating a gray-scale mask and the gray-scale structure has to be done in a UV-sensitive resist/polymer material. A dry etching step is still needed to transfer the gray-scale structure from resist/polymer into a substrate. One limitation of this technology is the expensive cost of the system. The writing process has to be repeated for every device

is another big disadvantage of this technology because it's impossible to massively produce devices in a low cost in this way due to the has-to-be-repeated laser writing process. The size of high power laser beam also limits the resolution (state-of-art is about 1 micron so far) that can be achieved using this technology. Generally this is a very costly technology for fabricating gray-scale devices.

Very recently, an interferometric phase contrast method was introduced to fabricate arbitrary diffractive optical elements [14]. This approach is based on an interferometric phase contrast method that transforms a complex object wavefront into an intensity pattern. The resulting intensity pattern is used to expose a photoresist layer on a substrate. After development, a diffractive phase object with an on-axis diffraction pattern is achieved. However, this method, just as described above, can be used to fabricate only diffractive optical components.

In 2009, L. Mosher et al. reported a double-exposure gray-scale photolithography technique and demonstrated that it produced three dimensional (3D) structures with a high vertical resolution [15]. This technique was developed for BHT mask. BHT is a pixelated grayscale mask and pixilated masks often suffer from limited vertical resolution due to restrictions on the mask fabrication. The double exposure technique uses two pixelated grayscale mask exposures before development and dramatically increases the vertical resolution without altering the mask fabrication process. An empirical calibration technique was employed for mask

design and was also applied to study the effects of exposure time and mask misalignment on the photoresist profile. This technology has been demonstrated, on the mask, to improve the average step between photoresist levels from 0.19 to 0.02 μm and the maximum step from 0.43 to 0.2 μm compared to a single pixelated exposure using the same mask design. The limitation in the vertical resolution is imposed by the mask fabrication process and the projection photolithography tool. The resolution of the projection system determines the upper limit on the pixel size. Typical low-resolution systems, such as the 5× projection tool used in this paper, have resolutions near 0.6 μm on the wafer. This allows pixel sizes up to 3 μm before spatial information from individual pixels begins to transfer. The mask fabrication limits the minimum pixel size and the minimum difference between pixel sizes. The projection photolithography tool and mask process enables grayscale designs using 15 square pixel sizes ranging from 0.6 to 2.0 μm. Double-exposure grayscale photolithography was developed in this paper to improve the vertical resolution compared to a single exposure without increasing the mask fabrication complexity. Similar to multiple-step techniques, the process consists of two aligned exposures before development, but each exposure uses a grayscale mask in place of a binary mask. Unlike multiple-step lithography, both exposures are overlaid above the same location on the photoresist. Examples of multiple-step photolithography in the literature use adjacent exposures, where each step is applied to unexposed photoresist. Double-exposure photolithography attempts a new phenomenon. Instead of exposing the photoresist down to the substrate or partially to create a gray level,

two partial exposures are superimposed to create a gray level that is not achievable using a single exposure. Therefore, the final structure is composed of a combination of both partial exposures. Any pixel size used in the first exposure may be followed by any other pixel size in the second exposure. If two different exposure times are used with n pixel sizes, double exposure will produce n^2 gray levels. Using this double-exposure photolithography the average step height was reduced by an order of magnitude, and the maximum step height was reduced by a factor of two compared to a single gray-scale exposure using the same set of pixel sizes. This improvement in the vertical resolution on mask enables fabrication of more complicated devices that require more precise vertical control. Very interestingly the main idea in this paper is very similar to the two-beam-current method we published in Applied Optics in 2008, which is presented and discussed in detail in Chapter 3.

In 2009 L. Jiang et al. reported the development of a grayscale lithography technique based on the use of a polymeric gray-scale photomask [16]. The photomask is made of patterned polydimethylsiloxane (PDMS) polymer doped with a UV absorbing laser dye. The PDMS photomask contains micro-patterns made by micro-molding the PDMS on a complementary silicon master mold. By adjusting the thickness of the patterns on the polymer photomask, the dopant dye concentration in the photomask and UV exposure dose, a multitude of unique 3D microstructures can be fabricated on the substrate with desired geometries and dimensions. A variety of 3D master mold structures for the PDMS photomask were made to enable highly

arbitrary microstructures to be formed in the doped PDMS photomask. This allows the fabrication of arbitrary microstructures in photoresist material by a single UV exposure step. One of the advantages of the polymer grayscale photomask method is it enables 3D microstructures to be fabricated in positive and negative photoresist materials. In this paper, 3D microstructures have been realized in SU-8 50 photoresist. The uniform doping of dopant in the photomask is an important factor. The polymer grayscale lithography method discussed here is relatively inexpensive and easy to implement. In principle, multiple layers of patterned PDMS photomask can be bonded to create complex and arbitrary 3D patterns through standard optical lithography. This technique is also extendable to different materials and applications. By selecting alternative dopant and photoresist, this technique can be used to realize high aspect ratio microstructures for a wide range of applications in microelectromechanical systems, micro fluidics and optics. The inherent flexibility of the PDMS grayscale photomask can enable lithography on non-uniform surfaces and allow the fabrication of unique 3D microstructures on non-planar substrates.

In 2007, S. Akbar et al. reported gray-scale lithography of photosensitive polyimide and its graphitization [17]. In this paper gray-scale lithography (GSL) was implemented using an aqueous developing photosensitive polyimide, HD8820. Gray Scale Lithography with HEBS glass photomask were implemented in the fabrication of graded junction edge terminations for silicon carbide power diodes and transistors. The GSL photomask was made by electron beam lithography 32-bit gray scale

intensity profile exposure of a silver doped HEBS glass that is sensitive to electron beams but not to ultra-violet UV radiation. When the photosensitive polyimide HD8820 was exposed through the gray scale photomask in a UV lithography system, the desired polyimide tapered profile was obtained. The polyimide patterns were subsequently converted to amorphous graphite at 650°C in a nitrogen furnace. Boron and aluminum high temperature ion implantations at several energies and doses were performed and the resulting dopant profiles, characterized using secondary ion mass spectroscopy SIMS, were found to correlate well with computer simulations. The GSL tapered photosensitive polyimide can therefore serve as an effective ion implantation barrier to obtain precisely graded dopant profiles. Micro-optics components such as gratings and Fresnel micro-lenses were also successfully fabricated using gray scale lithography of the photosensitive polyimide. It was found that the photosensitive polyimide HD8820 can work as an effective polymer for gray scale lithography. When converted to a graphitized form at 650°C in a nitrogen furnace, the polyimide showed less shrinkage than conventional photoresist and it closely retained its patterned shape during the graphitization process. For the fabrication of silicon carbide power diodes and transistors, the graphitized polyimide can function as a useful tapered barrier to dopant ion implantations at high temperatures to yield junction termination extensions capable of withstanding high reverse blocking voltages.

In 2008 T. Dillon et al. reported a progress on processing and modeling optimization for gray-scale lithography [18]. In this paper gray-scale lithography was applied to the fabrication of a fiber-to-waveguide coupler based on the parabolic reflector, where the efficiency of the device is quite sensitive to fabrication errors in the coupler geometry. In this case the thin photoresist and slowly varying topography conditions were not met and more comprehensive process models were tried to determine the appropriate transmission levels to encode in the photomask. It was demonstrated that the photomask can be optimized, based on simulation of the lithography process, to produce the required three-dimensional photoresist pattern. In summary, they introduced a fiber-to-waveguide coupling device, the so-called vertical J-coupler, which applied grayscale lithography to produce the smoothly contoured parabolic reflector geometry. Despite the high theoretical efficiency predicted by FDTD simulation, experimental efficiency was low at the beginning due to distortions of the parabolic reflector during the fabrication process. Later in designing new gray-scale mask for this device, they used the common approach to encoding the gray levels of the photomask according to the photoresist contrast curve. After extracting the model parameters for the new process, they simulated the lithographic processing using this approach and showed that distortion results were due to the neglecting of the details of the development process and the diffraction of the imaging process. It was demonstrated that the gray levels of the photomask could be optimized to recover the intended photoresist pattern. The distortion that results

from the pattern transfer into the underlying silicon substrate and how it could be compensated for were discussed in the paper.

In 2005 B. Morgan et al. developed a substrate interconnect technology for 3D MEMS packaging using gray-scale technology [19]. The development of 3-dimensional silicon substrate interconnect technologies, specifically for reducing the package size of a MOSFET relay, was reported. The ability to interconnect multiple chips at different elevations on a single substrate can significantly improve device performance and size. The process development of through-hole interconnects fabricated using deep reactive ion etching (DRIE), with an emphasis on achieving positively tapered, smooth sidewalls to ease deposition of a seed layer for subsequent Cu electroplating, were reported. Gray-scale technology is integrated on the same substrate to provide smooth inclined surfaces between multiple vertical levels (>100 μm apart), enabling interconnection between the two levels via simple metal evaporation and lithography. In this paper through-hole interconnects were optimized by tailoring the etch power and passivation cycle time during DRIE to control sidewall profile and morphology, easing deposition of a thin metal seed layer for subsequent copper electroplating. Gray-scale technology was then used to demonstrate a sloped wiring technique capable of providing interconnection between multiple vertical levels on a single silicon substrate. These two technologies can be used individually or in tandem to address a multitude of substrate and packaging issues, including the small MOSFET relay configuration proposed here. In short

words, the developments can be used to address packaging and integration needs. This idea is the same as we proposed when we designed and fabricated via/pad structure for high density interconnection (HDI) application, presented and discussed in Chapter 4.

In 2006 B. Morgan et al. applied gray-scale technology on an automated two-axis optical fiber alignment application [20]. This paper presents the design, fabrication, and characterization of the grayscale fiber aligner, demonstrating its value as an automated in-package alignment tool. They reported a new method for actuating an optical fiber in two axes. This device enables in package active alignment of an optical fiber towards reducing the time and cost of optoelectronic packaging by eliminating the need for expensive and slow macro-alignment machines. Opposing comb-drive actuators with integrated three-dimensional (3D) wedges (fabricated using grayscale technology) create a dynamic v-groove to alter the horizontal and vertical alignment of an optical fiber cantilever. All structural components are fabricated in silicon using a single gray-scale lithography and dry-etching step, making the system conducive to batch fabrication, an essential element to minimize the cost of including in-package alignment capabilities. Actuation of a cleaved fiber tip greater than 30 min each direction is demonstrated, with automated fiber alignment times on the order of 10 s, comparable to those achieved using macro-alignment systems. Alignment tolerances are held below 1.25 μm over a 20-by-20-μm actuation area for the first time. The influences of alignment target

location, actuation parameters, and alignment algorithm on total alignment time are also presented. The concept, design, fabrication, and testing of the gray-scale fiber aligner demonstrate its flexibility for aligning optical fibers in two axes. Actuation of a fiber cantilever > 30 μm in both the horizontal and vertical axes is demonstrated, with an estimated resolution of < 1.25 μm over much of the alignment area. The alignment times achieved with the on-chip gray-scale fiber aligner compare favorably to active alignment times reported using external actuators. The device configuration and control algorithms presented provide numerous avenues for optimizing active alignment time and accuracy for optoelectronics packaging.

In 2009 Y. Yamanishi et al. reported an interesting application of gray-scale technology on Micro-Electro-Mechanical Systems (MEMS) [21]. For the first time, they applied the gray-scale photolithography technique to the KMPR photoresist which can be dissolved in a stripper liquid, and hence this technique is appropriate to use for a high-accuracy molding to produce three-dimensional micro-tools which has many advantages over the conventional stereo lithography techniques in terms of the accuracy, cost and their performances by operating as magnetically driven micro-tools. They successfully operated 3D-MMTs which were fabricated by gray-scale lithography as micro-loader and micro-filter, and confirmed the applications for on-chip particle-handling. In this paper, they describe a novel method of fabricating three-dimensional polymeric magnetically driven micro-tools (3D-MMT) for performing non-intrusive and contamination-free experiments on chips. In order to

obtain precise and complicated three-dimensional patterns from magnetically driven 3D micro-tools, a grayscale photolithography technique was applied by making good use of thick negative photoresist as a sacrifice mold. By controlling an amount of ultraviolet light with a gradation of gray-tone mask, we fabricated a smoothly curved (100 μm gap) object without steps, which tend to appear in the case of conventional layer-by-layer photolithography techniques. A wide range of on-chip applications of micro-actuators can be realized by using the softness of polymer-based 3D-MMT. For example, a micro-filter and micro-loader were successfully operated by a combination of magnetic and fluidic forces. The FEM analysis of flow showed that a rotation of the 3D-MMT produces a relatively strong downward axial flow, which prevents a particle climbing up along the surface of the MMT. The produced 3D-MMT can be applied to complex on-chip manipulations of sensitive materials such as cells. Similar MEMS application was also explored in early stage of our project, explained in Chapter 5.

Photoresist plays one of the key roles in gray-scale lithography. In 2001 M. LeCompte et al. did an analysis and study on the photoresist characterization and linearization procedure for the gray-scale fabrication [22]. They present a procedure for the characterization and the linearization of the photoresist response to UV exposure for application to the gray-scale fabrication of diffractive optical elements. A simple and reliable model was presented as part of the characterization procedure. Application to the fabrication of surface-relief diffractive optical elements was

presented, and theoretical predictions are shown to agree well with experiments. Because there are many processing parameters that affect the photoresist response, developing and refining a recipe for gray-scale photolithography can be quite challenging. In this study, they developed a simple and reliable model based on processing parameters that accurately predicts the response characteristics of the photoresist to UV exposure in a gray-scale photolithographic process. They presented a theoretical model of the photoresist response and introduced an optical response parameter that describes the chemical sensitivity of photoresist to UV exposure. With the model and experimental results, they were able to determine the optical response parameter of photoresist AZ5214E. The theoretical model is quite useful and can be adjusted to handle multiple materials and negative photoresist.

Here is another paper about photoresist for gray-scale lithograph published by A. Kovalskiy et al. in 2006 [23]. In this paper, they presented results on the fabrication of DOE by conventional wet etching method using gray scale mask technology with ChG photoresist. They investigated the potential use of ChG with dry etching, which is more convenient than wet etching and provides a higher resolution. Previous studies show that dry etching can be an effective method for fabricating structures in ChG photo-doped with Ag. Wet and dry negative etching procedures are evaluated for the fabrication of 3D graded microstructures in As–S based inorganic photoresist. Absorption of light and consequent photo-structural changes near the surface layer enhances the chemical resistance of the As–S films.

The success of the procedure is demonstrated by fabricating arrays of 12 μm diameter micro-lenses in a thin $As_{35}S_{65}$ film using a gray scale Cr mask and wet etching. The selectivity of dry etching is successfully realized by using photo-diffusion in Ag–As_2S_3 bi-layer structure.

1.6 E-beam systems used in this dissertation

Two different e-beam systems were employed for the e-beam writing in this dissertation. One is Cambridge Leica EBMF 10.5/CS operated at 40 kV and another is Leica VB-6HR operated at 100KV. Both are located in Cornell Nano-scale Facility (CNF). The VB-6HR is a more advanced electron beam lithography system capable of reproducibly achieving feature sizes less than 30 nm. VB-6HR was employed in writing our gray-scale mask described in Chapter 3, while the Leica EBMF 10.5/CS was employed in the process described in Chapter 2 where VB-6HR was not available to us yet when the work described in Chapter 2 was done. VB-6HR system stage positioning is monitored by a laser interferometer with 0.6 nm precision. This capability of precise stage positioning makes it very suitable for our two-beam-current method and high resolution device structures. Leica EBMF 10.5/CS can handle only no more than 64 dosage levels in one e-beam writing and this is the reason only 64 gray levels were used in Chapter 2. VB-6HR system can handle up to 256 levels, so 256 gray-level patterns were designed and fabricated in

Chapter 3 and Chapter 4. In principle, more levels can lead to smaller step size, thus smoother surface for micro-structures.

1.7 Structure of the dissertation

In Chapter 2, the material and process of the improved gray-scale mask are presented. Cambridge Leica EBMF 10.5/CS operated at 40 kV was used for fabricating the 64-level gray-scale mask in this Chapter. In Chapter 3, a new two-beam-current method for writing gray-scale masks is described in details. The applications of the improved gray-scale technology to high-resolution micro-structures are included. In Chapter 4, the applications of improved gray-scale technology to micro-devices with deep (more than 2 microns) structures are demonstrated. Leica VB-6HR e-beam system operated at 100 kV was employed for e-beam writing in these two chapters. Chapter 5 is a summary of research ideas and results in earlier stage of the project. Discussions and summary are presented in Chapter 6.

2. Material and Process of Improved Gray-scale Mask

2.1 Motivations of improved gray-scale technology

To fabricate micro-devices of many phase levels with standard binary masking techniques, multiple masks must be used, and multiple alignments, exposures, and processing steps must be performed [1-2]. In fact, this technique needs *N* masks and *N* processing steps to achieve 2*N* gray levels, so a high production cost results from the need for the multiple lithography and processing steps. Misalignment between masks and the lithography steps also leads to degradation in resolution. Consequently, an alternative process based on gray-scale masks has been developed [3, 4, 8, 9, and 10]. This gray-scale photolithography process allows the fabrication of an *N*-level profile by use of only a single mask and a single processing step. Alignment error is thus avoided. High-energy beam-sensitive (HEBS) glass was used in some experiments as the gray-scale mask material [24, 25, 26, 27, 28, 29, and 30]. The principle behind this mask fabrication method is that HEBS glass changes its opacity when exposed to a beam of high-energy electrons or a laser. For example, gray-scale masks may be generated in an electron-beam (e-beam) writer by varying the dosage of electrons striking different areas of a HEBS glass plate. However, a HEBS gray-scale mask cannot provide

enough optical density at wavelengths shorter than 350 nm for fabrication of high-resolution components (see Fig. 1.4).

2.2 New mask material for improved gray-scale technology

A new light-attenuating film (LAF) is studied for the gray-scale mask. The LAF is a carbon-based material provided by Gray Scale Technology, Inc. and can potentially reach very high optical density (3.0 or more) for deep ultraviolet (248- and 193-nm) lithography applications [31]. Higher densities at shorter wavelengths mean potentially higher-resolution components with more phase levels than are achievable with HEBS masks. A comparison of optical density variations between HEBS and our LAF is shown in Figure 1.4. It shows that the optical densities of 300-nm-thick LAF are 3.02 and 5.62 at 248 and 193 nm, respectively, whereas the optical density of HEBS glass has a maximum of 3.0 at ~500 nm and decreases to less than 2 at 365 nm.

2.3 Fabrication process of new gray-scale mask

The fabrication process of this new kind of gray-scale mask is shown in Figure 1.3. An e-beam writer (Cambridge Leica EBMF 10.5/CS) with an acceleration voltage of 40 kV was used to write on the ZEP 7000A e-beam resist [Fig. 1.3 (a)]. The thickness of ZEP 7000A was 510 nm. A layer of 20-nm Cr film

was applied to the surface of the ZEP 7000A/LAF/ quartz structure. The sole purpose of this Cr layer is to avoid the local charging of the mask plate during the e-beam writing process.

After the Cr/ZEP/LAF/quartz plate in the e-beam writer was exposed to patterns of 48 dosage levels, the top Cr layer was removed with the standard chrome etching solution (wet etch). Then the resist was developed in ZED 750 developer [Fig.1.3 (b)].

The developed resist pattern was transferred into the LAF by use of a Reactive Ion Beam Etch 250 system from Technics Plasma [Fig. 2(c)]. This ion-milling system was designed to accommodate the introduction of reactive gases to provide chemically assisted ion-beam-etching capability.

To fully use the whole thickness of the 300-nm LAF, the etching ratio between the ZEP 7000A and the LAF was targeted at 510:300, or about 1.7:1, since the pattern depth in ZEP 7000A is 510 nm. To achieve this targeted etch ratio, a chamber pressure of approximately 8.2 3 1025 Torr was used, together with a f low of 4.89-SCCM Ar and a f low of 0.2-SCCM O2 (SCCM denotes cubic centimeters per minute at STP). The other etching parameters include perpendicular ion incidence, an acceleration voltage of 600 V, an ion-beam current of 100 mA, and a sample chuck with rotating capability. To completely etch through the 510-nm ZEP

7000A, an etching time of 25 min was needed. The profile of an axicon in LAF measured by atomic force microscopy is shown in Fig. 2.1.

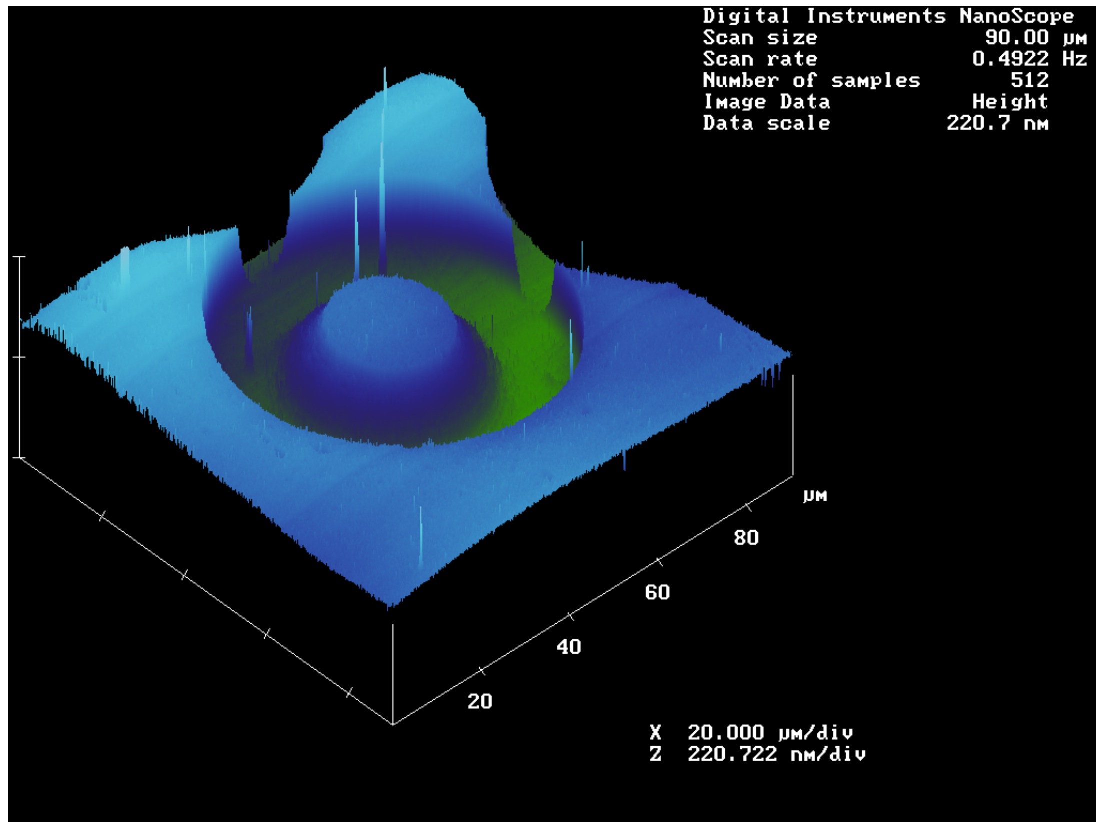

Figure 2.1 Axicon in LAF measured by atomic force microscopy

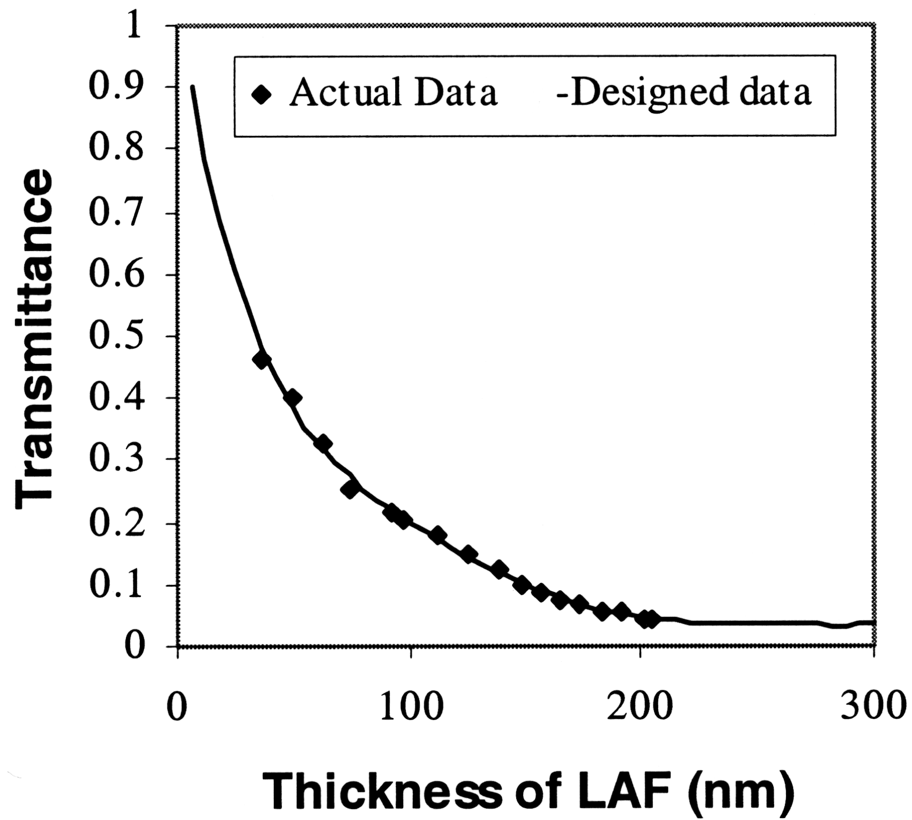

Figure 2.2 (a) Actual transmission profile compared to the designed LAF thickness

The solid line in Figure 2.2 (a) is the designed LAF thickness profile and the theoretical transmittance profile based on the designed LAF thickness profile. The data were measured at a wavelength of 315 nm, which is the central wavelength of the spectral range of a Karl Suss MJB-UV300 aligner available for this measurement.

Figure 2.2 (a) and Figure 2.2 (b) provide the comparison between the actual transmittance data in our mask and the designed data. The designed transmittance in Figure 2.2 (b) is related to LAF thickness *d* in Figure 2.2(a) as exp(-κd), where κ is the absorption coefficient of LAF. Figure 2.2 (b) calculated the cross-correlation factor between the designed and the actual transmittance. The R2 value is 0.9987, which mathematically shows that the fabricated transmittance is very close to the designed profile. Figure 2.2(a) and Figure 2.2(b) show that the gray-scale profile of a designed transmittance function can be accurately fabricated.

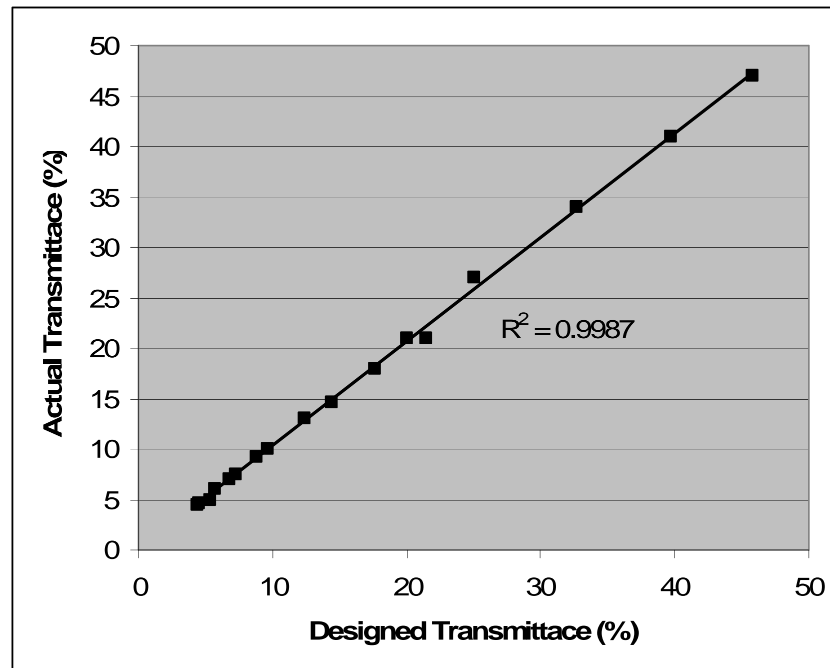

Figure 2.2 (b) Transmission comparisons between the designed and the fabricated gray-scale steps on the mask.

2.4 Conclusion

In summary, an improved gray-scale mask was fabricated on a new light-attenuating material. The gray-scale mask has the potential of producing higher-resolution micro- and meso-optics of more phase levels or other kinds of micro-components than HEBS masks.

3. Two-Beam-Current Method for E-beam Writing Gray-Scale Masks and Its Application to High-Resolution Micro-Structures

3.1 Introduction

Two-beam-current method is introduced for e-beam writing in the fabrication of gray-scale masks [32]. Compared with the simpler single-current method, the two-beam-current method offers two important advantages: (a) it can achieve much larger dynamic range for e-beam exposure; (b) the writing time for a gray-scale mask can be reduced considerably when a large pattern is to be written. In this article the new method is first described in details and its application to the fabrication of our new gray-scale mask is demonstrated. Then, the improved gray-scale masks were employed to fabricate large dynamic range, high-resolution micro-optical elements of less than a couple of microns depth, using DUV lithography at 248nm wavelength and an Inductively Coupled Plasma Reactive Ion Etching system.

In all e-beam writings for mask fabrication, only one e-beam current has been used till now. For binary masks (or masks of binary transmittance), there is no reason to use more than one current for the e-beam writing. However, for gray-scale masks (or masks with gray scale transmittance) the dynamic range of the dosage becomes important, when tens to hundreds different e-beam doses may be needed. A two-

beam-current method, which employs two different e-beam currents in sequence to write the gray-scale pattern, is developed to achieve larger dynamic range of e-beam dosage. In this method the computer-generated pattern files for the e-beam writing system divide the whole gray-scale pattern into two portions, one for each of the two currents respectively. The first e-beam of lower current writes the portion of the gray-scale pattern that needs lower e-beam dosage. The second e-beam of higher current writes the portion that needs higher dosage. Both portions of the computer-generated patterns files have the same starting (or settling) point for the e-beam writing. The two portions of the computer-generated e-beam pattern files and two-beam-current writing sequence are illustrated in Figure 3.1.

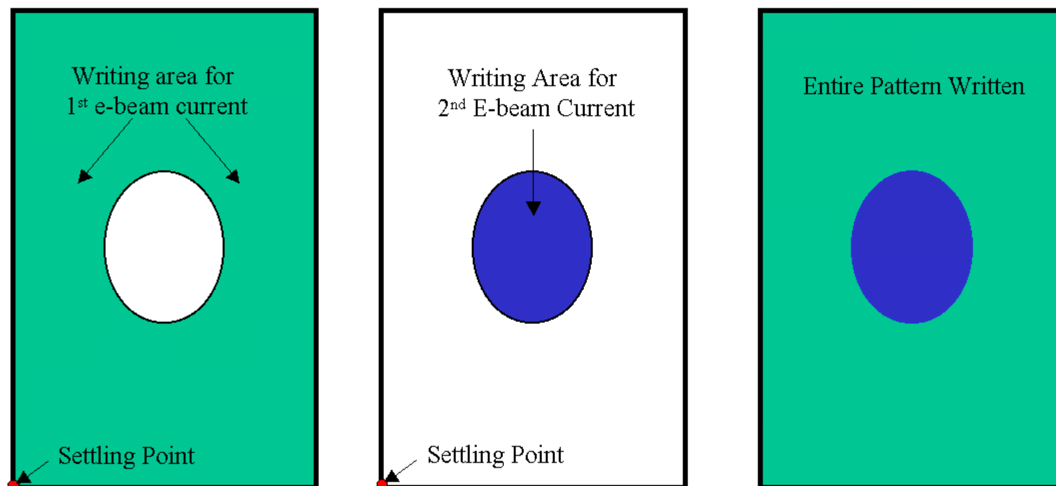

Figure 3.1 Illustration of two-beam-current method of e-beam writing

With larger dynamic range of e-beam dosage, we can achieve larger dynamic range in the transmittance of the gray-scale mask. When the two-beam-current method is implemented, we found that it can also offer the advantage of reduced e-beam writing time for large gray-scale masks. In section 3.2 the possible gain in dynamic range and reduction in writing time is analyzed. In section 3.3 the fabrication of gray-scale mask using both single- and two-beam-current methods is described and compared. In section 3.4, gray-scale mask is used to fabricate different structures. Discussions on technological issues unique to the two-beam-current method, such as the effects of recalibration of e-beam system required by the two-current method on writing time reduction and alignment between the two patterns written by the two currents, are provided in section 3.5.

3.2 The two-beam-current method of writing gray scale masks

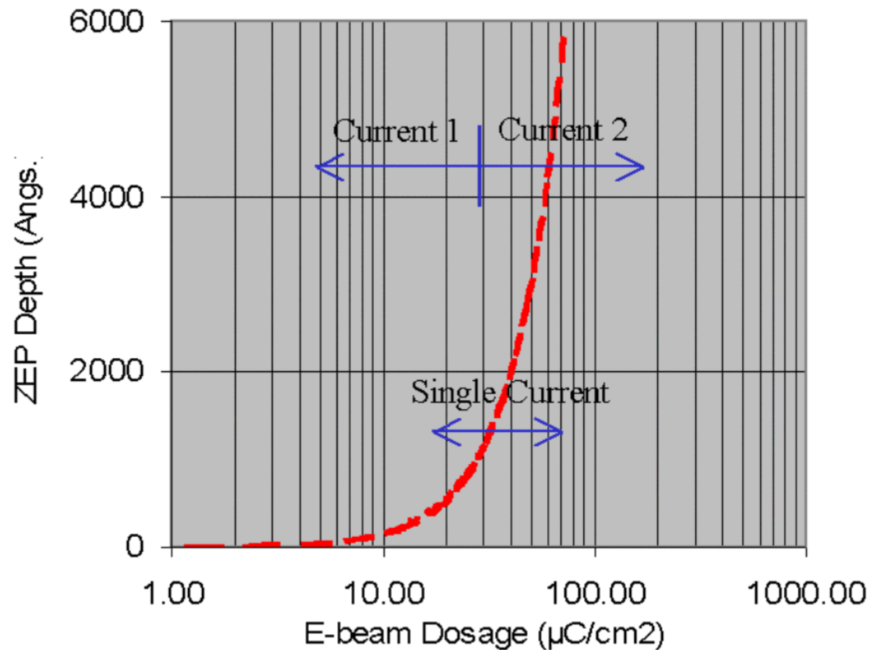

Figure 3.2 The exposure characteristic of ZEP 7000A e-beam resist is shown by the dotted line. Also shown is the comparison of dosage dynamic range between single current I_s and two currents I_1 and I_2 .

Fig.3.2 illustrates that the comparison of dosage dynamic range between the two-beam-current and the single-beam-current methods. The increase in dynamic range is discussed in section 3.2.1, and the writing time reduction in section 3.2.2. The general criteria for choosing the two currents in the two-current-method to give larger dynamic range and shorter writing time will be provided in section 3.2.3. To implement the two-beam-current method, the Leica VB-6HR e-beam system at Cornell operating at 100 kV was employed for e-beam writing and a ZEP7000A of 510 nm thickness was chosen as the e-beam resist in the experiment. The dotted line

in Fig. 3.2 illustrates the exposure characteristic of ZEP7000A we obtained in calibration measurement. The developed ZEP7000A pattern is then transferred onto a carbon based light attenuating film (LAF) to produce the gray-scale mask [10].

The transmittance of the new gray-scale mask is related to the thickness d of the LAF according to exp(-κd), where κ is the absorption coefficient of the LAF (which is a constant) [10]. In order to maximize the optical density range of the mask, the entire thickness of the e-beam resist and the entire thickness d (300 nm) of the LAF should be utilized.

To calculate how much the dynamic range can be increased and the e-beam writing time can be reduced when two beam currents were used, we can make use of the following expression for dosage:

$$D = I / (f * S) \tag{3.1}$$

where I is the beam current, f is the clock frequency and S is the area of pixel grid. Clock frequency is inversely proportional to the dwell time of e-beam current at each pixel grid. For optimum e-beam writing time, every e-beam system has a finite range of clock frequency to be used. This leads to a finite range of D, when I and S are fixed.

3.2.1. Dynamic range increase for gray-scale mask

To illustrate the dynamic range increase by the use of the two-current method, let I_s be the single current used, I_1 and I_2 be the two currents used, and (f_{max} to f_{min}) be the range of clock frequency used. Furthermore, let us assume I_s to be 1.5 nA, I_1 and I_2 to be 0.5 nA and 2.5 nA respectively. We chose S to be 400 nm^2, which corresponds to a pixel size of 20 nm. The minimum pixel size that Leica VB-6HR can achieve is 5 nm, corresponding to S = 25 nm^2. For the same current and clock frequency, a smaller pixel size would result in larger dosage D. On Leica VB-6HR f_{max} is fixed at 25 MHz. f_{min} is usually 5 MHz for optimized writing speed, although it can be as low as 100 KHz.

Then, the dynamic range for D in the single current method will be (D_{max} to D_{min}), where

$$D_{max} = I_s / (f_{min} * S) = 75\ \mu C/cm^2$$

and
$$D_{min} = I_s / (f_{max} * S) = 15\ \mu C/cm^2.$$

The dynamic range for D in the two current method will be (D'_{max} to D'_{min}), where

$$D'_{max} = I_2 / (f_{min} * S) = 125\ \mu C/cm^2$$

and $D'_{min} = I_1 / (f_{max} * S) = 5\ \mu C/cm^2$

From these equations, we can estimate the dynamic range is increased from 5 (75:15 $\mu C/cm^2$) to 25 (125:5 $\mu C/cm^2$). If the single current of 1.5 nA were used to obtain D'_{min} (5 $\mu C/cm^2$), f_{max} would have to be 50 MHz, which would exceed the capability of Leica VB6 system. If the single current of 1.5 nA were used to obtain D'_{max} (125 $\mu C/cm^2$), f_{min} would have to be 3.0 MHz, which is smaller than 5 MHz. A smaller f_{min} means longer e-beam writing time.

Due to the different ranges of exposure we can read from Fig. 1 the depth ranges of developed ZEP7000A is 500 to 5000 angstroms for the single-current method and that for the two-current method is 100 to 6000 angstroms, as shown in Fig. 1. So, the thickness range of two-current method (5900 angstroms) is about 31% larger than that of single-current method (4500 angstroms). When the thickness profile of ZEP7000A is etched onto the LAF at the same etch ratio, the thickness range of the LAF will also be 31% larger for two-current method.

3.2.2. Writing time reduction for gray-scale mask

The two-beam-current method can also help to reduce the e-beam writing time for gray-scale mask fabrication. To illustrate writing time reduction, let us assume the same dosage range of 15~75 $\mu C/cm^2$ is to be covered. The mid-point of this dosage range is 45 $\mu C/cm^2$. For single current method, 1.5 nA would be used for both the low dosage range (15~45 $\mu C/cm^2$) and the high dosage range (45~75 $\mu C/cm^2$). For the two-beam-current method, we could use 1.5 nA for the low dosage range (15~45 $\mu C/cm^2$) and a higher current (2.5 nA) for the high dosage range (45~75 $\mu C/cm^2$). In other words, the difference between the two methods is that we could choose a higher current to write the area of the high dosage range. Using higher beam current to achieve the same dosage range means faster clock frequency and less writing time. This explains why the two-beam current method can save writing time, compared with the single-current method.

To estimate how much time can be saved by the use of the two-beam-current method, we make use of Equation (3.1) again.

$$f = I / (D * S), \quad \text{where S is 400 nm}^2.$$

Moreover, if we take A as the total area of the pattern to be written, the total e-beam writing time T can be expressed as

$$T = A / (S * f), \tag{3.2}$$

where f is the average clock frequency for the e-beam writing. In comparing the writing times between the single current and two-beam-current methods, A and S will be the same and can be taken as constants. To calculate the total writing times T we need only to calculate the f_s for the single current and f_1 and f_2 for the two current methods:

For the single current method, the average dosage is D_s = 45 μC/cm^2 (for the 15~75 μC/cm^2 range). Using Equation 4, we calculate its corresponding frequency to be f_s = 8.33 MHz. For the two current method, the average dosages are D_1 = 30 μC/cm^2 (for the 15~45 μC/ cm^2 range) and D_2 = 60 μC/cm^2 (for the 45~75 μC/cm^2 range). Using Equation 4, we calculate f_1 = 12.5 MHz and f_2 = 10.41 MHz.

Assuming that the pattern area in the 15~45 μC/ cm^2 range is the same size as that in the 45~75 μC/ cm^2 range, the total writing times T_s for the single current and T' for the two current method can be calculated to be:

$$T_s = A / (S * f_s) = 1.2 \times 10^{-7} * (A/S) \text{ seconds,}$$

$$T' = 0.5A / (S * f_1) + 0.5A / (S * f_2) = 0.88 \times 10^{-7} * (A/S) \text{ seconds.}$$

Therefore, the time saving will be (1.2 – 0.88) / 1.2 = 26.7%, which is significant.

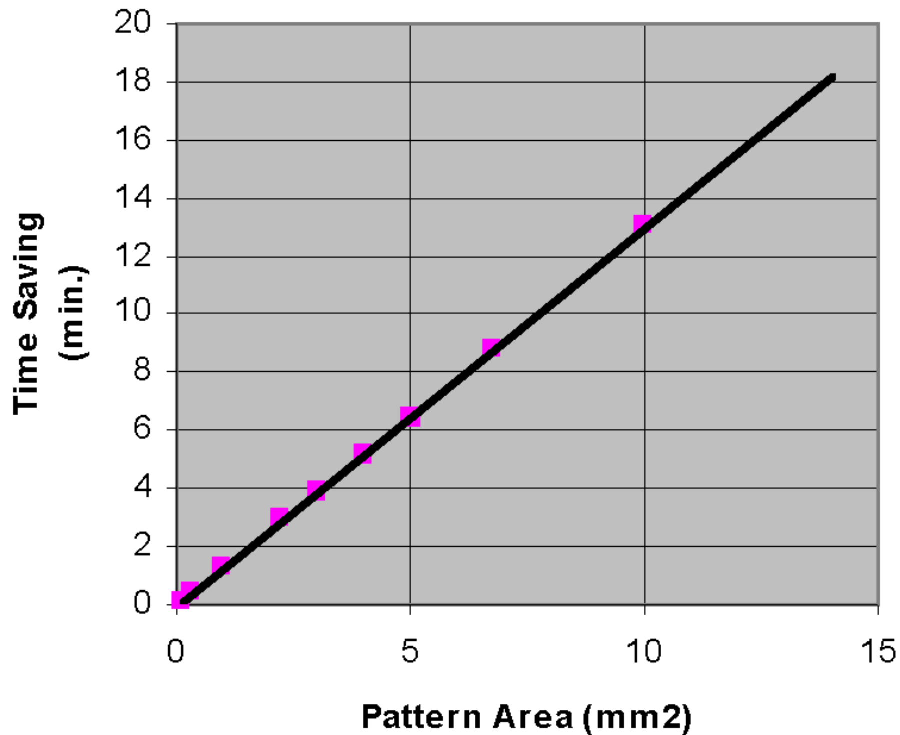

Figure 3.3 Time saving for the two-beam-current method calculated from the online Parameter Calculator (provided by IBM [33]) for Leica VB-6HR e-beam system. The slope of the line in this figure is about 1.3 min/mm^2.

Another way to estimate the actual e-beam writing time is to use the online Parameter Calculator for Leica VB-6HR provided by IBM [33]. For a pattern area of 2.25-mm^2 to be written, the Parameter Calculator gives 11.19 minutes for single current and 8.27 minutes for the two-current method, resulting in about 3 minutes (or 26.1%) saving in writing time. For a larger pattern area of 10 mm^2, the Parameter Calculator shows the same percentage (26.1%) of time saving in writing time. Fig.

3.3 shows the time saving calculated by the online Parameter Calculator for a range of writing areas, assuming the same writing parameters chosen above. If I_2 were larger in the above calculations, for example 4.5 nA, then the time saving could be larger than what we can obtain from 2.5 nA. This is because for the same dosage and the same pattern size, larger current leads to higher clock frequency and shorter writing time. (More discussions on writing time saving, including that for writing even larger area, is given in section 3.5.1.)

3.2.3. Criteria for choosing the two currents

Hence, the general criteria for choosing the two currents in the two-current-method are: (a) I_2 should be chosen to reach the maximum required dosage, determined by what it takes to clear the e-beam resist (e.g. ZEP 7000A for our experiment); (b) I_1 should be chosen so that its maximum reachable dosage (when the slowest clock frequency of the e-beam system is used) is the same as the minimum reachable dosage by I_2 (when the fastest clock frequency of 25 MHz is used). There should be no dosage gap between the maximum dosage reachable by I_1 and the minimum dosage reachable by I_2. When the above two conditions are met, then I_1 should be as small as possible so that the exposure dynamic range can be maximized; at the same time I_2 should be as big as possible so that the writing time saving can be maximized.

3.3. Gray-scale mask fabrication

Gray-scale masks fabricated by the two-beam-current method is described below, and compared with those by a single beam current method.

3.3.1. E-beam resist and its preparation

The e-beam resist we used was ZEP 7000A. A resist spinner applied it on a LAF-coated quartz substrate. The LAF film on quartz has 300 nm in thickness. The spinning parameters are 300 rpm for 3 seconds, followed by 550 rpm for 177 seconds. After being allowed to relax for 5 minutes, the resist was baked in a convection oven at 180 °C for 30 minutes. This results in a resist layer of 550 nm in thickness. This ZEP7000A coating process was recommended by the resist manufacturer and was performed at Telic Company.

A 10nm Cr film was next coated on the resist surface by a sputtering machine. The role of this Cr layer is to avoid the local charging of the mask plate during the e-beam writing process. The Cr/ZEP7000A/LAF/Quartz sample is now ready for e-beam writing. The Cr coating was carried out at Nanofilm Inc.

ZEP 7000A is a positive resist frequently used in the semiconductor industry. Longer exposure on the resist will cause more of it being washed off when it is

developed. Thinner resist will contribute to more of the underlying light attenuating material being etched away, resulting in higher transmission, when the e-beam resist profile is transferred into the LAF by dry etching.

It should be pointed out here that the dosage to clear certain thickness of e-beam resist varies for different e-beam system. For example, to clear the entire ZEP 7000A resist thickness, a higher dosage is required (approximately 62 $\mu C/cm^2$) for the Leica VB-6HR (operating at 100KV), whereas to clear the same resist thickness it requires only about 20 $\mu C/cm^2$ for the Leica EBMF 10.5/CS system (operating at 40KV). This is because higher accelerating voltage means higher electron energy and higher possibility of punching-through without exposing the e-beam resist. In other words, the electrons have less chance of exposing the e-beam resist at higher energy.

3.3.2. E-beam writing process and ZEP7000A resist development

0.475 nA and 2.05 nA were actually used for the two currents experiment and 1.5nA for the single beam current experiment in pattern writing. Other parameters of the Leica VB-6HR system, the calibration pattern and device patterns are all kept the same to obtain a fair comparison on the e-beam writing times of the two approaches.

The beam size of the system was 5 nm small. The pixel grid size of our patterns was chosen to be 20 nm. A beam size of 25 nm was used; it was chosen a little larger than the pixel grid size in order to obtain smoother pattern surfaces. A calibration pattern of 64 steps was designed and written on the same mask that contains other device patterns.

The ZEP 7000A resist was developed in a ZED 750 developer for 2 minutes at room temperature (23 °C); then the sample was rinsed in ZED-D for 10 seconds. The development method was immersion with mild agitation. After the development step, anatomic force microscope (AFM) was used to measure the calibration steps. About 40 nm (or 7.3% of the original 550 nm thickness) of ZEP7000A was lost during the development process. This is normal because 5-10% of the pre-development thickness is usually lost during the resist development process.

To simplify the comparison between the resist profiles written by the two-current and the single current methods, the same resist development parameters were used on the two masks.

3.3.3. Dry etching for gray-scale mask

To fully use the entire 300nm thickness of the light-attenuating film, the etching ratio between ZEP 7000A and the light-attenuating film was targeted at

510:300 = 1.7:1, since the pattern depth in the developed ZEP 7000A is 510nm. To achieve this targeted etch ratio, a Trion inductively coupled plasma reactive ion etching (ICP-RIE) system was used with the etching parameters of 10 mTorr etching pressure, 50/5 sccm CF_4/O_2, 50W inductively coupled plasma (ICP) power, 50W reactive ion etching (RIE) power and 20 °C of chiller temperature. To completely etch through the 510 nm ZEP 7000A, an etching time of 22 minutes was needed.

3.3.4. Experimental results

To verify e-beam writing time reduction for the two-current method, we simulate the writing of a collection of small patterns on a Leica VB-6HR, including calibration steps, axicons and retro-reflectors, and repeat them 5 times, totaling 0.4 mm^2 in area. The parameters used in the writing simulation are exactly the same as those used in the calculations provided in section 2.2.

We find that 125 seconds will be required for the single current method, whereas it takes only 96 seconds for the two-current method. The time saving is therefore 29 second or 23.2%, which is very close to the predictions (26.7% vs. 26.1% in theoretical calculation shown in Fig. 3.3). When the collection of small patterns was repeated 10 times totaling an area of 0.8 mm^2, the writing times become 249 seconds for the single current and 190 seconds for the two-current

methods, respectively. This results in 59 seconds or 23.7% of time saving, which is also closely in agreement with predictions.

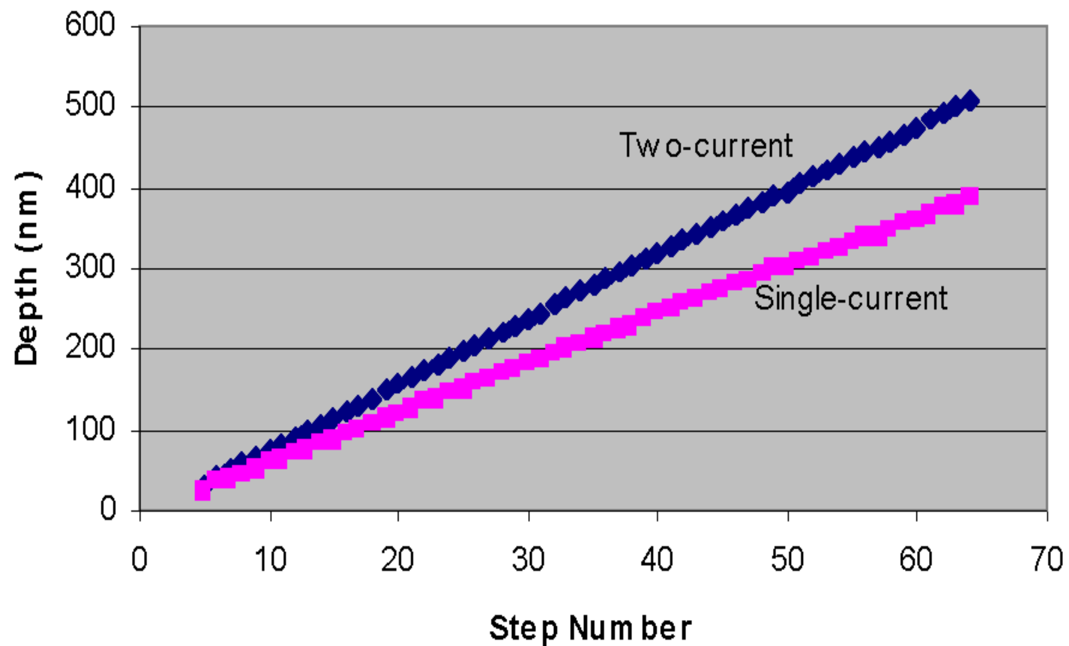

Figure 3.4 The measured depth profiles of the calibration steps in the e-beam resist. The depths at step #64 are about 510nm and 400nm for two-current and single-current method respectively.

Fig. 3.4 shows that the full range (510 nm thick, 64 calibration steps) of the e-beam resist is etched when two beam currents are used to write the resist. It also shows that the range of resist depth is smaller (~ 400 nm, 64 calibration steps) when we use a single beam current to write while maintaining the same parameters to develop the resist. This is consistent with results illustrated in Fig. 3.2.

After transferring the developed resist profiles onto the LAF by dry etching, the optical densities of the calibration steps @248 nm wavelength could be obtained from the thickness data and the absorption coefficient of LAF. Figure 3.5 provides the data, which shows that the gray-scale mask written by the two-current method can achieve an optical density range as high as 3.02, whereas the mask written by the single current method can provide only a range of 2.30.

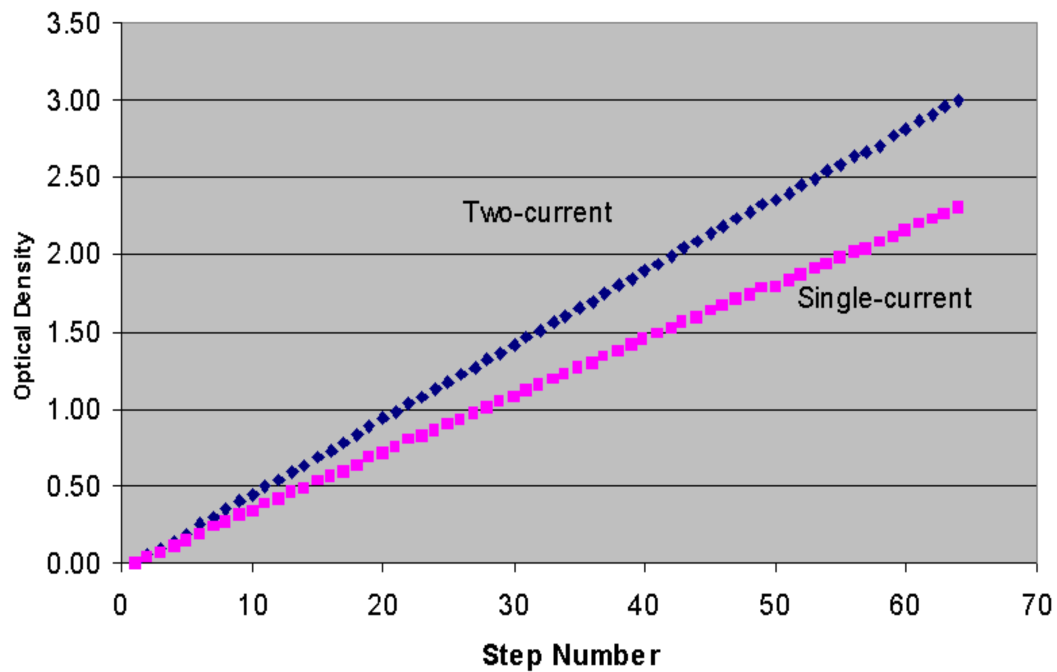

Figure 3.5 Optical densities of the calibration steps at 248nm. The maximum optical densities (at step #64) achieved in two-current and single-current methods are 3.02 and 2.30 respectively.

3.4 Fabricating micro-optical devices

Using the new gray-scale mask, the procedures for fabricating devices of shallow (about a couple of microns in depth) microstructures are as follows: Transmittance patterns in the gray-scale mask are transferred into an optical resist using an optical stepper. The gray-scale profiles in the developed optical resist are then transferred onto the substrate to obtain the devices by dry etching in an Inductively Coupled Plasma Reactive Ion Etching (ICP-RIE) system. Only a single iteration of optical lithography and dry etching is required in gray scale technology, as compared to multiple iterations required by binary technology to produce microstructures with gray scales in devices.

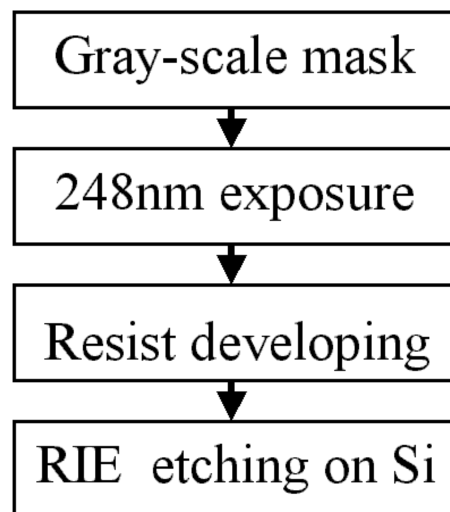

Figure 3.6 The fabrication processes of high-resolution micro-devices using our improved gray-scale masks.

Since our mask can work in deep ultra-violet (DUV), a 248nm stepper and optical resists sensitive to 248nm were employed in the optical lithography process. Hence, higher resolution can be achieved in the device microstructures when one compares with using 365nm or longer wavelength lithography. The wavelength of 248nm is out of the reach of any gray-scale mask on High Energy Beam Sensitive glass because its optical density becomes quite low at wavelengths below 300nm [10, 27]. Fig.3.6 summarily shows the fabrication procedure of gray-scale devices by the use of our improved gray-scale technology.

3.4.1. The optical lithography process

A Nikon stepper operated at 248 nm with a 4:1 demagnification factor was employed in this experiment. It is located at the Pennsylvania State University. Shipley UV5 and MicroChem PMGI-SF11 were used as the optical resists. UV5 is a very popular, thin resist for 248nm binary lithography and was used to fabricate the binary gratings to demonstrate the high-resolution capability of our gray-scale mask. PMGI-SF11 resist is a thick, good analog resist for gray-scale lithography in DUV range and was used to fabricate an off-axis Fresnel lens and other gray-scale patterns in this experiment. Generally analog resists have lower contrast than binary resists in their characteristics.

UV5 has a typical thickness of 300nm. The preparation, exposure and developing parameters of UV5 are provided in Table 3.1.

Table 3.1 Processing parameters of UV5 resist

Resist Spinning	5000 rpm, 45 seconds
Resist Baking	130 °C, 1 min, Hotplate
Exposure	10 mJ/cm2
Developing	LDD26W, 45 seconds
Hard Baking	145 °C, 3 minutes, Hotplate

Table 3.2 Processing parameters of PMGI-SF11 resist

Resist Spinning	2000 rpm, 45 seconds
Resist Baking	115 Deg. C, 120 seconds, hotplate
Exposure	75 mJ/cm2, 248 nm
Developing	MF 321, 180 seconds, immersion, mild agitation
Rinse	DI water, 30 seconds
Dry	Nitrogen gas

The typical thickness of PMGI-SF11 is 1 to 2 microns. The preparation, exposure and developing parameters of PMGI-SF11 resist are provided in Table 3.2. Fig. 3.7 shows the typical exposure characteristics of PMGI-SF11 at 248nm.

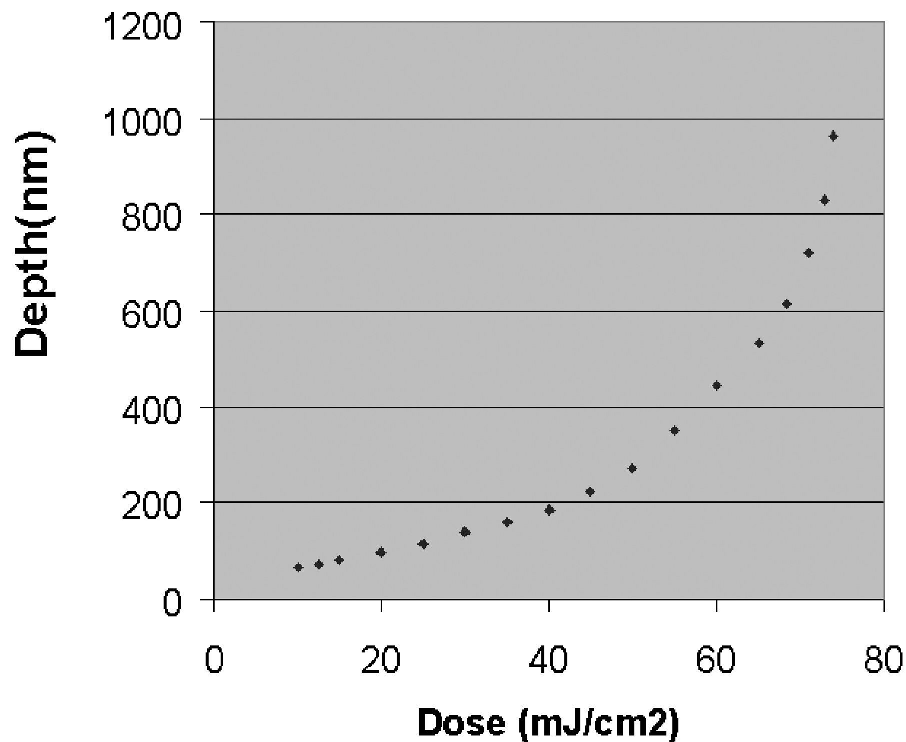

Figure 3.7 Exposure characteristic of PMGI-SF11 resist.

3.4.2. Dry-etching for fabricating optical devices

A Trion MINILOCK II ICP-RIE etcher was used to transfer the gray scale profiles in the developed optical resists onto the substrate. Quartz was adopted as the substrates for the fabrication of Fresnel lens. ICP-RIE can operate with higher plasma density at lower pressure, in comparison with conventional parallel plate RIE system. It is a cleaner system and can perform more uniform etch over a larger area.

The parameters employed for etching PMGI-SF11 to Quartz are provided in Table 3.3.

Table 3.3 Parameters for etching PMGI into quartz

Pressure	10 mTorr
ICP/RIE power	40/120 W
CF_4/Ar	20/20 sccm
Temperature	5 °C

The dry etching parameters in Table 3.3 result in etching rates of 45 nm/minute for PMGI and 21 nm/minute for quartz, and the etch ratio of about 2.1 : 1. In order to avoid overheating the resist, the etching process was paused for 5 minutes after every 5-minute etching. In order to get more uniform etching, the substrate was manually rotated for 90 degrees after every 10-minute etching.

3.4.3. Experimental results

Using the new gray scale mask and a 248nm stepper, a resolution of 0.2 micron was achieved in a UV5 resist as shown in Fig. 3.8. Binary gratings with different periodicities were the patterns used for testing the resolution limit. Here, no

resolution enhancement method (e.g., phase contrast method) was used in our pattern design.

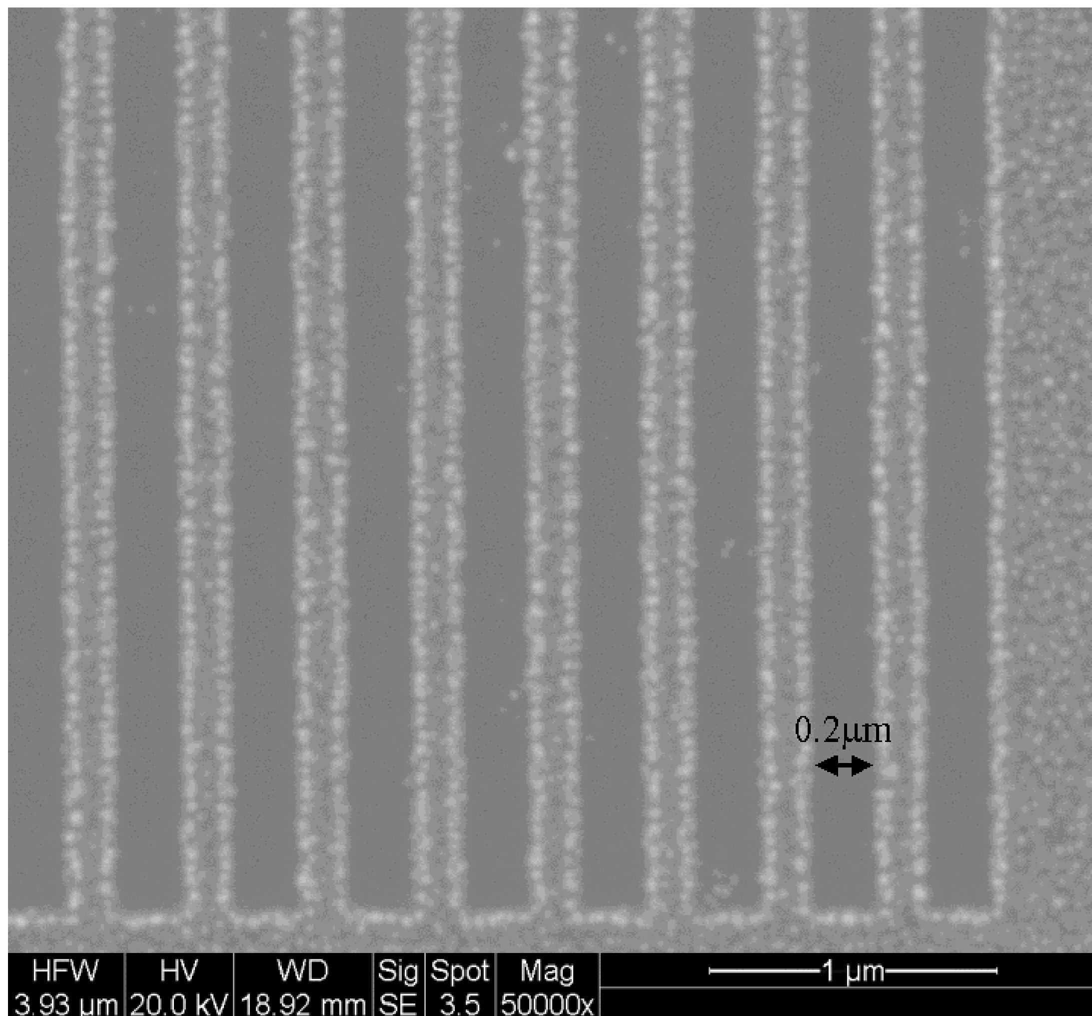

Figure 3.8 SEM picture showing a resolution of 0.2 micron in UV5 by 248nm lithography.

Figure 3.9 is the atomic force microscopy (AFM) picture of an off-axis Fresnel lens on quartz. Due to the limitation of the AFM scanning lateral range (~75 microns), only a portion of the Fresnel lens was captured. The periodicities in the shown region of the Fresnel lens are between 10 and 12 microns.

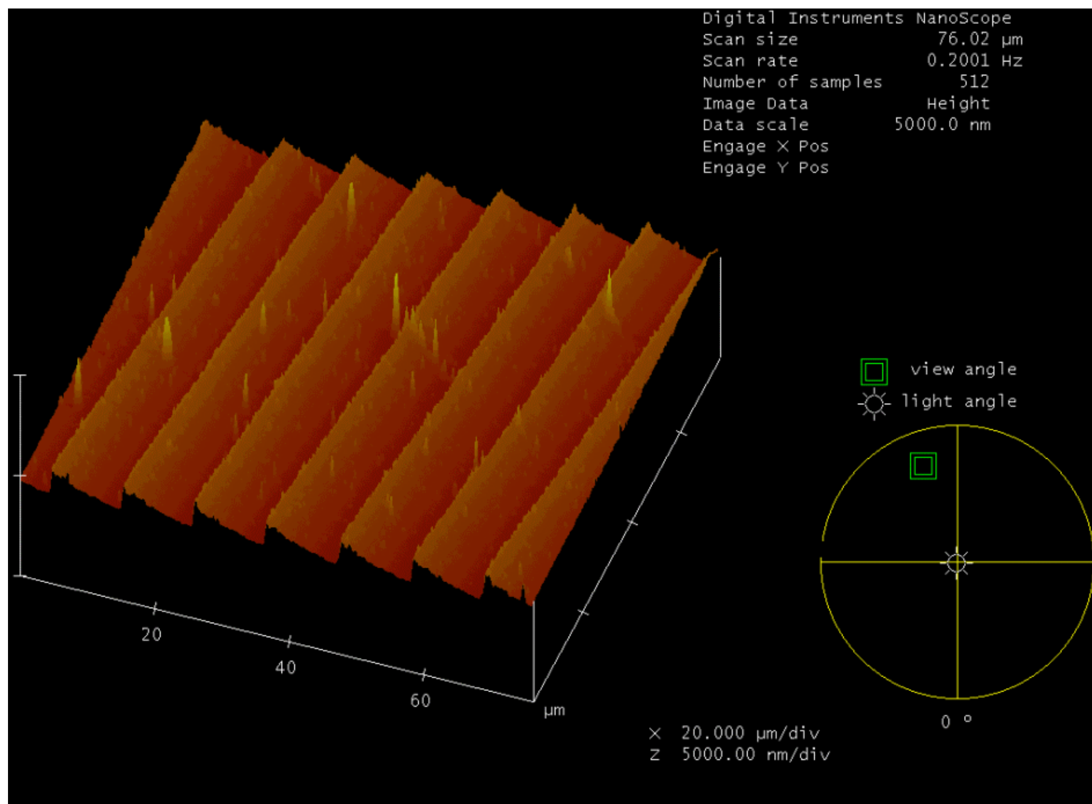

Figure 3.9 AFM picture of a portion of an off-axis Fresnel lens on quartz

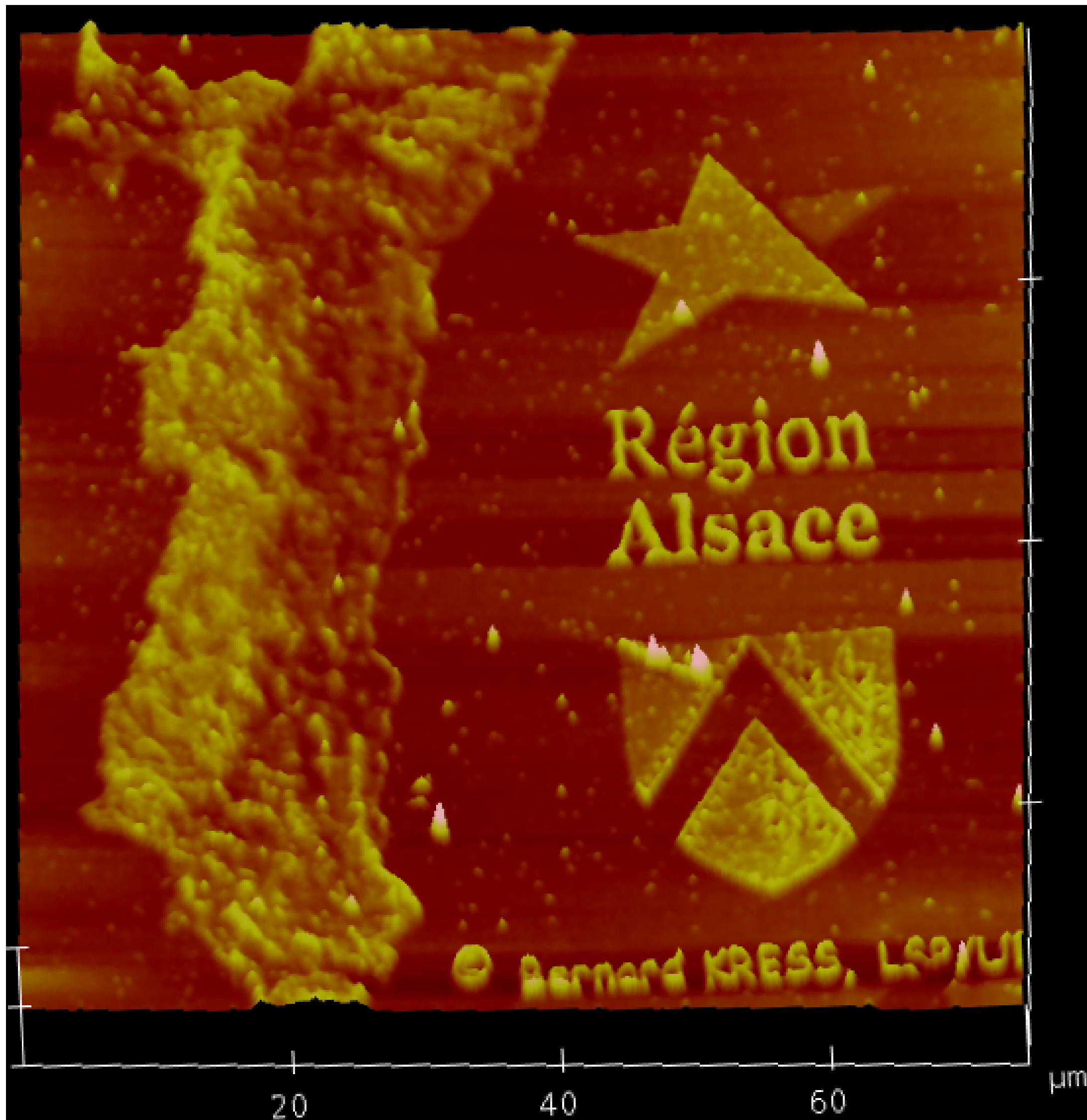

Figure 3.10 An AFM picture of a 3-D topographic map on LAF

Figure 3.10 is an AFM picture of a map with interesting 3-D topography in the Alsace region of France, fabricated on our gray-scale mask. The area of the map is about 20 microns x 70 microns, close to the size of a human hair cross-sectional area.

3.5 Discussions

3.5.1 The effect of recalibration of e-beam system required by the two-current method on writing time reduction

When two currents are used in e-beam writing by Leica VB-6HR, an important fact to take into account is that a certain amount of time (5 to 10 minutes usually depending on the operator) will be needed to call the second pattern file, re-calibrate the e-beam system for the second e-beam current and to re-position the stage holding the sample. From Fig. 3.3 we can see that when the pattern area to be written is small, this extra time could be more than the writing time saving. Therefore, only when writing a larger pattern area (e.g. > 10 mm^2 with the same parameters adopted for Fig 3.3) can time saving be expected for the two-beam-current method.

For a 6-inch mask, we can estimate the saving in writing time as follows, when two-beam-current method is used. Conservatively let us also assume that only

1% of the total mask area needs to be written by the two-beam-current method. Then, the total writing area becomes about 225 mm^2. From Fig. 3.3 we can estimate the time saving would be about 290 minutes (or 4 hours 50 minutes), which is much larger than the extra time for recall/recalibration/reposition. For an 8-inch or 12-inch mask, the time saving would be even bigger. Therefore, the larger is the mask writing area, the more time saving we can realize by the two-beam-current method to reduce the mask fabrication costs.

3.5.2 Alignment and stitching issues in using two-beam-current method

The two-beam-current method requires the computer-generated pattern data file for e-beam writing be partitioned into two, based on the dynamic range requirements, one for each of the two currents. Both portions of the pattern file use the same starting point. The alignment accuracy of the second pattern written by the second current with respect to the first depends on the re-alignment of the stage holding the sample while the current is changed and re-calibrated. This mechanical re-alignment will usually cause some stitching error between the two patterns, typically about 40 nm for the Leica VB6 system. Experimentally, we did observe this small stitching error in the e-beam resist pattern and its transfer to the mask in the dry etching process, as shown by the stitch line on the mask in Fig. 3.11 (a). The ellipse on the top portion of the elliptical axicon mask has the dimensions of 21.20 μm (minor axis) by 25.44 μm (major axis), and the bottom ellipse 40 by 48 μm.

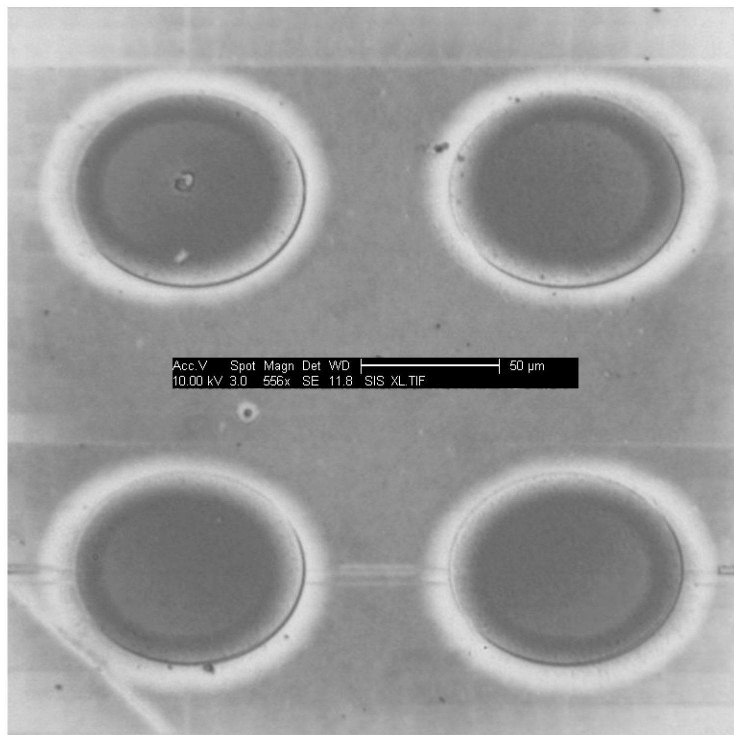

Figure 3.11(a) Microscope pictures of axicons on the gray-scale mask;

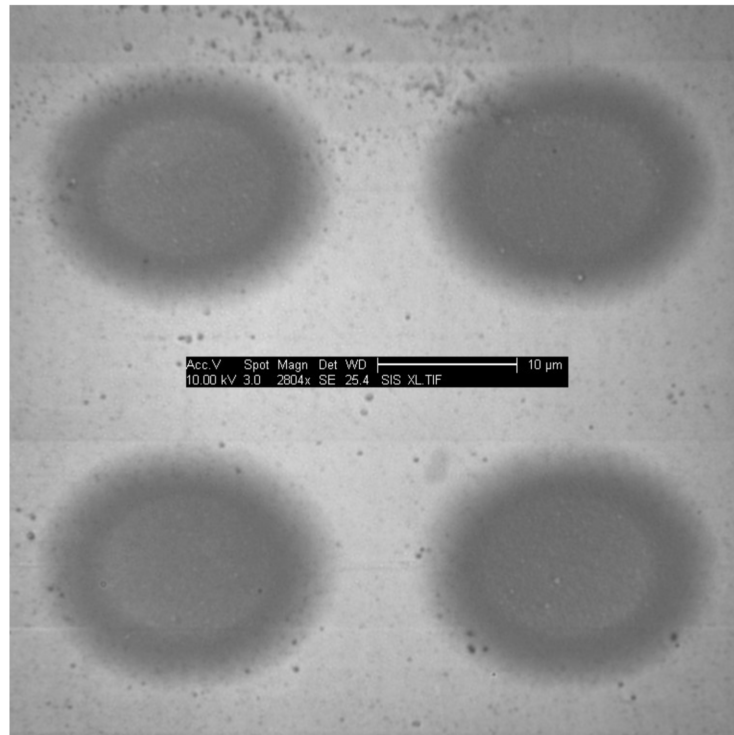

Figure 3.11(b) The microscope pattern on PMGI resist (enlarged four times to show the disappearance of the curved line due to stitching error).

However, in the optical lithography process the stepper employed has a wavelength of 248 nm and a de-magnification factor of 4. When the stitching error is less than 40nm, this stitching error is reduced significantly to a level not observable in the optical resist, as shown in Figure 3.11(b). Figure 3.11(b) shows the microscope picture of an axicon on PMGI, enlarged 4 times to the same size as that of the mask for a better comparison with Figure 3.11(a). This small stitching error on the optical resist should not cause much surface smoothness problem in device fabrication of micron dimensions.

3.5.3 The effects of the accuracy of e-beam clock frequency on dynamic range

As mentioned in previous sections, the dynamic range of exposure can be expanded dramatically by using the two-beam-current method. The accuracy of clock frequency of an e-beam system also affects the dynamic range of the exposure. For the Leica VB6HR system used in this project, the maximum clock frequency is 25 MHz. This maximum clock frequency is limited by the accuracy of clock frequency, which means the higher accuracy of the clock frequency is, the higher maximum clock frequency can be. As mentioned previously the lowest frequency normally used in e-beam writing is about 5 MHz. So the exposure dynamic range is about 5 for this system when single e-beam current is used. Nowadays, e-beam system with more accurate clock frequency has been developed and this progress keeps moving forward. For example, Vistec Inc. has developed VB6 e-beam systems with doubled accuracy, and even quadrupled accuracy, for clock frequency. Their latest VB6UHR system has achieved a clock frequency of 50 MHz and even 100 MHz. These two advanced e-beam systems can elevated the dynamic range by a factor of two and four respectively. This means an exposure dynamic range of 10 and 20 respectively, compared to the dynamic range of 5 got for VB6HR used in this project, when a single current is used. So a more accurate clock frequency can also expand the exposure dynamic range efficiently. However, the idea of two-current-method is always applicable when a larger exposure dynamic range is needed when a more accurate clock frequency itself can not provide. For example for a VB6UHR

system with a maximum clock frequency of 100 MHz, its exposure dynamic range can be expanded from 20 to 400 by using two-beam-current method.

3.5.4 Extension to three-beam-current method

The approach behind the two-current method, as discussed in this paper, can be extended to three or more currents, when larger dynamic range for fabricating devices of deeper microstructures or more e-beam writing time reduction for larger pattern area are needed. Currently, the optical density of 3 (achievable by the two-beam-current method) may have been sufficient for many applications; there appears no great need to explore for higher optical density. In the future when need arises, the extension to three or more beam-currents can be explored. Carbon-based light modulating material we employed can be used for the gray-scale mask in 193nm lithography [8], which is a shorter wavelength than the 248nm used in this paper. Shorter wavelengths generally allow for higher resolution devices to be fabricated.

3.6 Conclusion

The two-beam-current method has been demonstrated successfully for e-beam writing in the fabrication of our new gray-scale mask. This method gives a larger e-beam exposure dynamic range than one-beam-current method. It also saves much e-beam writing time, lowering the costs of gray-scale masks to an affordable level when the writing area is large.

Since our gray-scale mask is on a carbon based light modulating material, it can work in the DUV and UV wavelength range for device production, instead of being restricted to i-line or longer wavelengths. Higher resolution components and devices can be made when shorter wavelength optical lithography can be applied.

Gray-scale technology will help to lower the production costs for devices with multiple depth levels in many fields of application, since it requires only one optical lithography and dry etching iteration, while binary technology requires multiple iterations. However, more careful monitoring is required in mask fabrication, optical lithography and dry etching processes to preserve the gray-scale, when gray-scale technology is applied. This will be discussed in next chapter, where our gray-scale mask is applied to fabricate devices with depth deeper than a couple of microns.

4. Applications of Improved Gray-Scale Technology to Micro-Devices with Deep Structures

4.1 Introduction

We present a low cost method for producing micro-devices with deep micro-structures, using our improved gray-scale technology. In this method a Karl Suss MJB3-UV300 contact aligner operating at 315nm and an Inductively Coupled Plasma Reactive Ion Etching (ICP-RIE) system by Trion were employed for the gray-scale optical lithography process and the dry etching process respectively, as reported in this chapter. 256 gray levels, instead of the 64 gray levels that have been published previously [10], were used to fabricate the gray-scale mask in order to get smoother surface for micro-devices with bigger size and deeper structure. Micro-devices with deep structures can find important applications in many fields. For example, aspherics, and retro-reflectors are important in the field of micro-optics; micro-via/pad structure is important in the field of microelectronics.

The new carbon-based gray-scale mask material offers a large optical density range in the DUV and UV wavelength range [10]. To realize the large density range, all devices described in this chapter use gray scale masks written by the two-beam current method [32] described in chapter 3. A Leica VB-6HR e-beam system at Cornell was used for the e-beam writing. It allows the density range be divided into

256 gray levels, which can be utilized to fabricate devices with deep gray-scale microstructures and to improve the surface smoothness of devices. The amount of gray levels affects mostly the design of computer-generated pattern files for the e-beam writing in mask fabrication, while it rarely affect the device fabrication process.

Since fabricating devices by gray scale technology requires one iteration of optical lithography and dry etching, the fabrication cost of devices by gray-scale technology is lower in comparison with the fabrication cost by binary technology [34, 35], where multiple iterations of lithography and etching steps are required.

In this chapter a Karl Suss MJB-UV300 contact aligner at 315nm wavelength was employed as the optical lithography tool. An Inductively Coupled Plasma Reactive Ion Etching (ICP-RIE) system by Trion was employed for dry etching [36]. We successfully fabricated some micro-devices, e.g. aspheric lens, retro-reflectors, and microelectronic micro-via/pad, in silicon substrate.

Silicon is a popular semiconductor single-crystal material. It is widely used in fabricating various micro-devices, e.g. Micro-electro-mechanical systems (MEMS) devices et al. Etching technology for silicon is mature today. Silicon material also has a big hardness (8~13 GPa, Silicon<100>, single crystal) [37] and very high melting point (1687 K, 1414 °C or 2577 °F). These properties make it very suitable

to be a mold material for molding polymer-based micro-devices. Silicon is nearly transparent in the spectrum used for long-wavelength optical telecommunication (1.3 to 1.55 microns) [38]; therefore silicon is a good material for manufacturing micro-lens or waveguide for telecommunication applications.

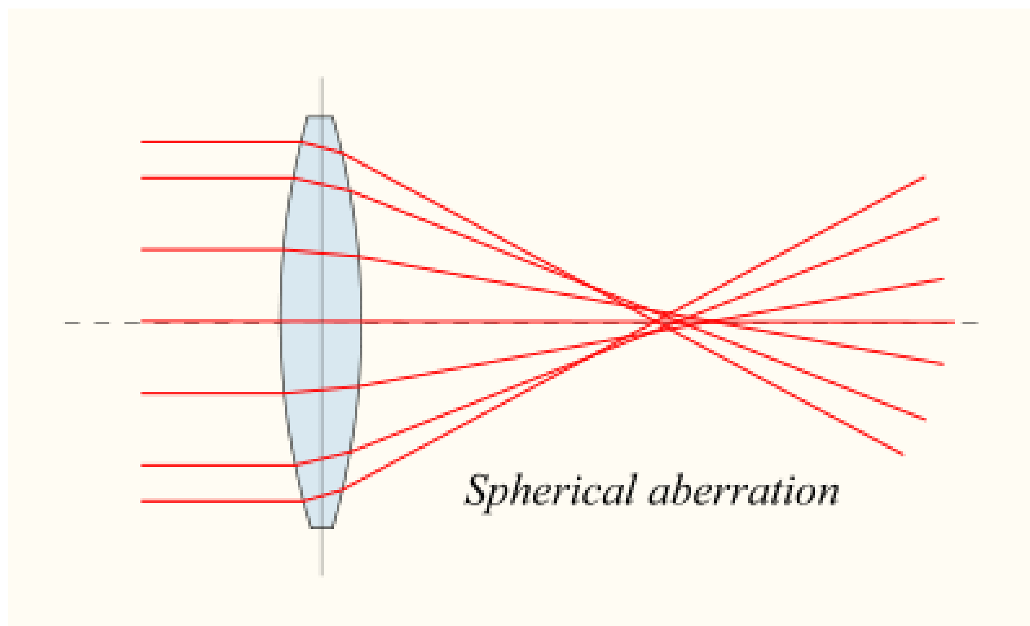

Figure 4.1 Spherical aberration of a normal spherical lens

Aspherics is very important in optics because an ideal aspheric lens provides zero spherical aberration [39, 40, 41]. Figure 4.1 shows the spherical aberration of a typical spherical lens. The spherical aberration of a spherical lens becomes more serious when the f-number (sometimes called focal ratio, f-ratio or relative aperture; in simpler terms, the f-number is the focal length divided by the aperture diameter

[42]) of the lens becomes smaller, because of the relatively smaller focal length. Figure 4.2 compares a normal spherical lens (lower) and an aspheric lens (upper) with zero spherical aberration. Aspheric lenses with big sag would provide both zero spherical aberration and small f-numbers. They are important to applications that require compact designs, and are not producible by simply melting resists as some spherical lenses are made [7]. In this paper a lens in parabolic shape is fabricated and used to demonstrate the capability of our gray-scale technology for fabricating aspheric lens.

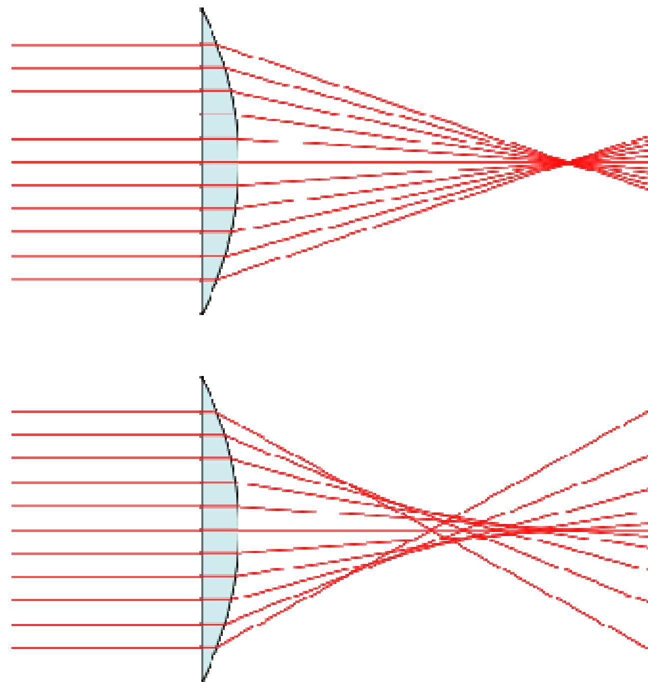

Figure 4.2 Comparison of a normal spherical lens (lower) and an aspheric lens (upper) with zero spherical aberration

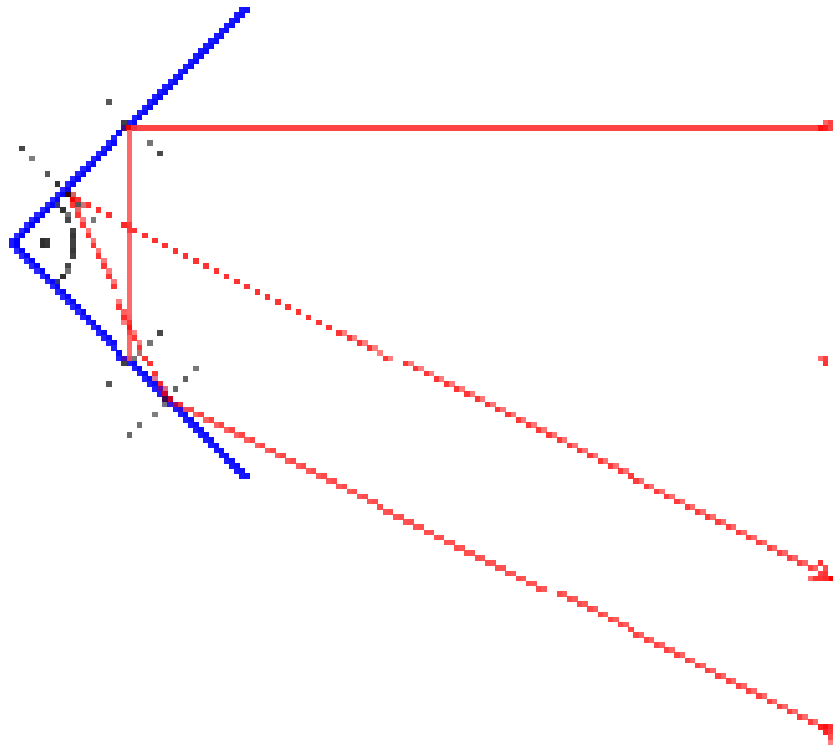

Figure 4.3 Working principle of a 2-dimentional retro-reflector

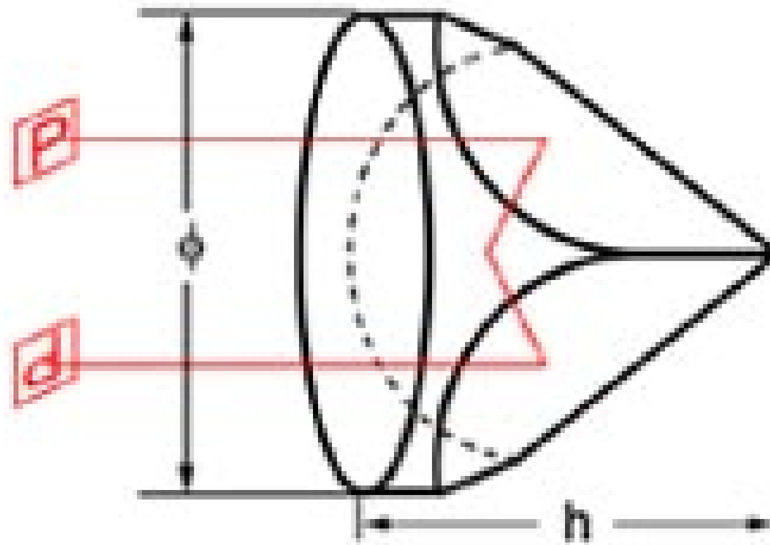

Figure 4.4 A 3-dimentional retro-reflector (also called corner-cube, corner-reflector)

The unique property of retro-reflector is that it can bounce an incident beam back to the source where the incident beam comes from [43]. Figure 4.2 and Figure 4.3 show how a 2-dimentional and 3-dimentional retro-reflector work. A 3-dimentional retro-reflector is also called a corner cube or a corner reflector. This characteristic of retro-reflector has been utilized to build free space optical communication links [44], where only one laser and a modulator at each end of the link (instead of two lasers, one at each end of the link) are employed for bi-directional communications. Examples of such links are those for communicating with satellite or aircraft, where the weight of the load is important. At present the commercially available retro-reflectors are too big to be integrated with the small semiconductor modulators employed to achieve faster modulation rates. The

technology demonstrated in this paper shows the capability of fabricating retro-reflectors in arrays and in meso-scale for these applications.

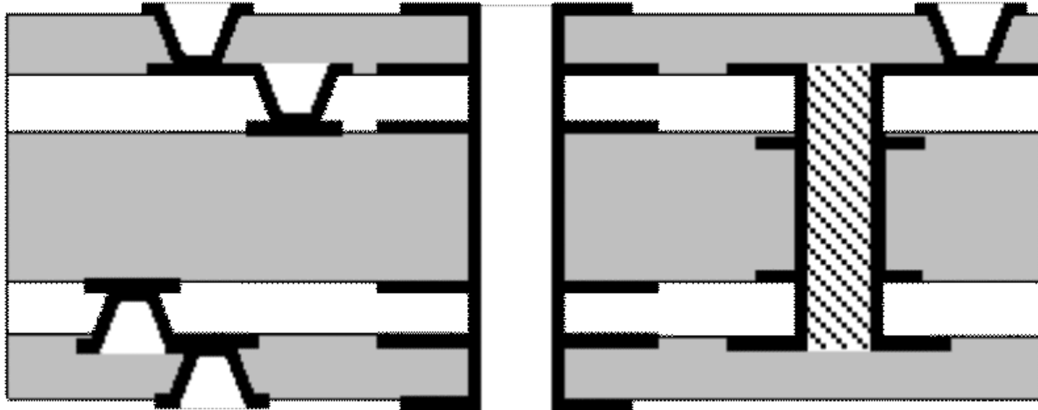

Figure 4.5 Via/Pad structures in a typical multi-layer PCB board

Micro-via/pad pairs are very frequently needed for high density interconnection (HDI) application in microelectronics [45]. Figure 4.4 shows Via/Pad structures in a typical multi-layer PCB board. The via/pad structures can be fabricated first in silicon, which are then employed as moulds for replication in polymer or printing circuit board (PCB), to lower the manufacturing cost of HDI. When micro-via/pad pairs are fabricated by using binary lithography, at least two masks and two lithography steps are needed. This causes alignment errors and put a limit on the current state-of-art size of via/pad in industry presently to about 200 microns. By employing our gray-scale technology, the alignment error between

multiple lithography steps can be eliminated, and a 30-micron size has been demonstrated without difficulty in our experiment. Smaller sizes of micro-via/pad pair would be very valuable to increase the interconnection density in HDI application

4.2 Device design

The large optical density range offered by our gray-scale technology can be utilized to produce gray-scale devices with deep microstructures and to improve on the surface smoothness of gray-scale devices. For micro-optics applications, gray-scale devices with smooth surfaces are often required. For MEMS applications, gray-scale devices with deep (more than a couple of microns) micro-structures are often needed.

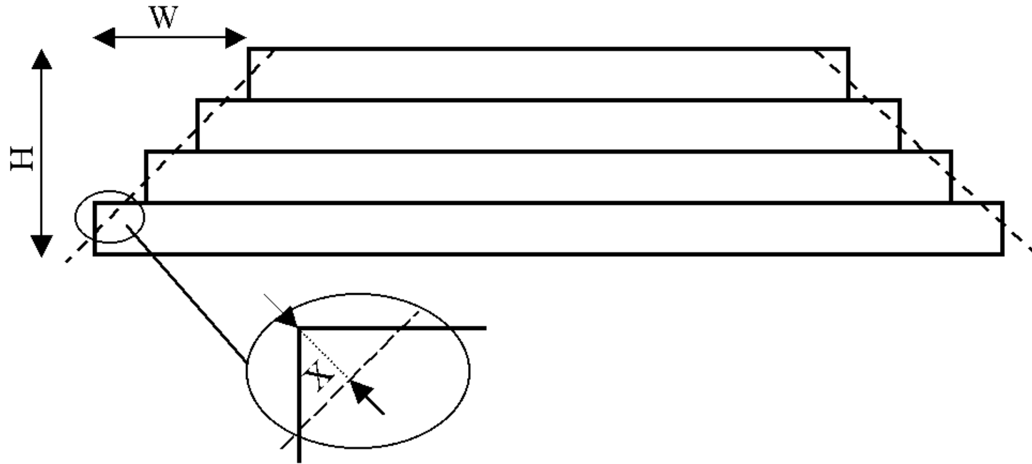

Figure 4.6 A smooth surface with a slope of H/W can be approximated by many quantized steps. Its surface roughness X can be calculated as a function of H, W and the number of quantized steps (N).

Micro-optics requires smooth surfaces to keep the optical efficiency high and the scattering noise low. Smooth surfaces require a larger number of gray levels in the designs to reduce their roughness. The roughness X of a surface with slope (H/W), as shown in Fig. 4.6, can be calculated to be

$$X=HW/[2N(H^2+W^2)^{1/2}] \tag{4.1}$$

So, the roughness is inversely proportional to the total number of gray levels. As an example, if $H=W=2\pi$ and $N=8$, then $X = 0.09\pi$ or a little better than ($\lambda/20$).

Figure 4.7 shows the relationship model between the theoretic surface roughness X (in unit of micron, defined in Figure 4.6) and the total number of gray levels, for sets of different dimensions of H and W. From the figure we can find that for the same roughness of 0.11 micron, the required number of gray levels is 32, 64 and 128 respectively for three sets of dimensions: H=W=5 microns, H=W=10 microns, and H=W=20 microns. This is the same as common sense and very easy to understand. The larger and deeper the device is, the more gray levels is needed to maintain the same surface roughness.

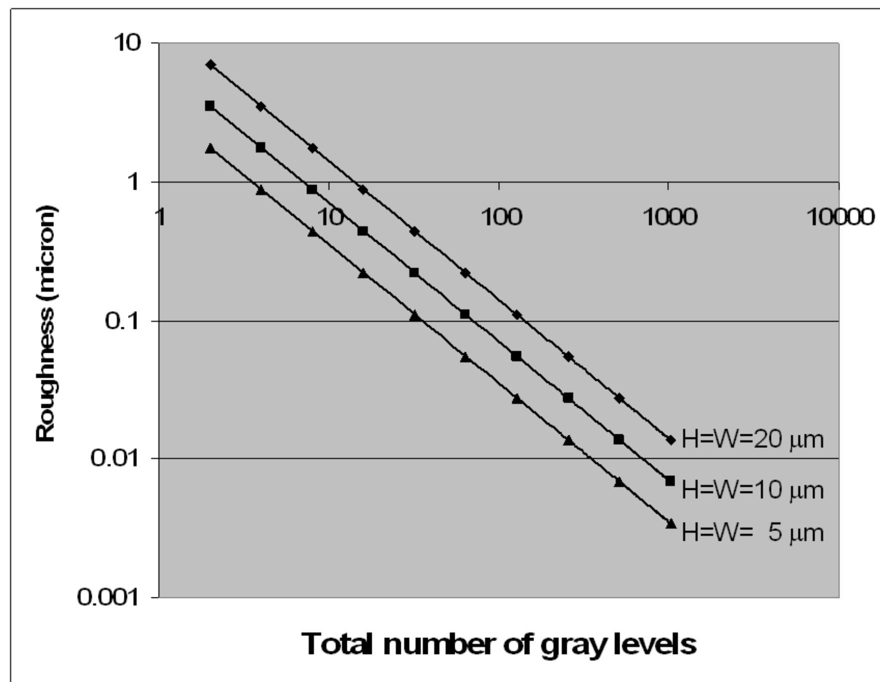

Figure 4.7 The relationship between the theoretic surface roughness X and the number of gray levels

To estimate the depth of optical devices that can be fabricated with smooth surfaces, let's assume that an optical lens with 8 levels for every 2π-phase retardation in height is acceptable, when light travels through the device. Then, a device with 256 levels can accommodate 64π of phase retardation at the device operation wavelength. If the device is made of quartz with a refractive index of about 1.54, and operated at $\lambda = 1.31$ μm, then the device thickness can be about 27 μm deep. If the device is made of silicon, whose refractive index is about 3.4, and operated at the same wavelength, the device depth can be about 12.3 μm. The devices mentioned in this chapter are all fabricated in silicon and no optical device in this chapter is deeper than 12.3 microns.

4.3 Device fabrication

A gray-scale mask that satisfies the design considerations on surface smoothness in Section 4.2 was written by the two-beam current method [32]. Using this gray-scale mask, a number of devices were fabricated by following the process procedure shown in Fig. 4.8.

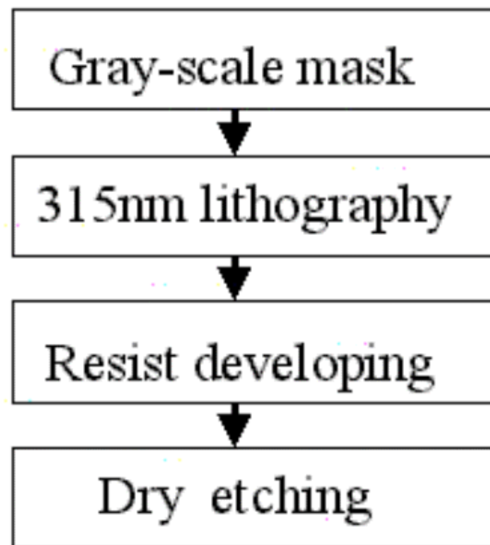

Figure 4.8 Flow chart of the procedure for fabricating gray-scale devices

4.3.1 The optical lithography process

A gray-scale mask with the desired transmittance profiles for various devices was employed to expose the optical resist Shipley SPR220. SPR220 is a positive resist chosen to accommodate the large optical density range offered by the mask. It is also a general purpose, multi-wavelength (i-line and g-line in the UV range) resist that can be coated in a wide range (1-10 microns) of film thicknesses. It has excellent adhesion characteristics, which make it ideal for thick film applications. The typical resist thickness we used was about 4 microns.

The preparation, exposure and development parameters of SPR 220 are listed Table 4.1.

Table 4.1 Processing parameters of SPR220-3.0 resist

Resist Spinning	2000 rpm, 45 seconds
Resist Pre-Baking	115 °C, 120 seconds, hotplate
Exposure	240 mJ/cm2, 315 nm
Developing	MF 321, 180 seconds, immersion, mild agitation
Rinse	DI water, 30 seconds
Dry	Nitrogen gas

Post-exposure-baking (PEB) is often used to enhance the acidity caused by exposure to light for catalyzing the polymerization reactions. The polymerization reaction would cause the exposed resist become more soluble in the developer [46]. Because diffusion of the acid catalyst can cause image spreading (or blurring) during post-exposure thermal processing we did not use the PEB process in our lithography process to avoid this pattern blurring phenomenon.

Fig. 4.9 shows the exposure characteristic of Shipley photoresist SPR 220-3.0. To fabricate gray-scale devices with smooth surface, we would like to see a small slope for this curve. A lower developing temperature and a diluted developer

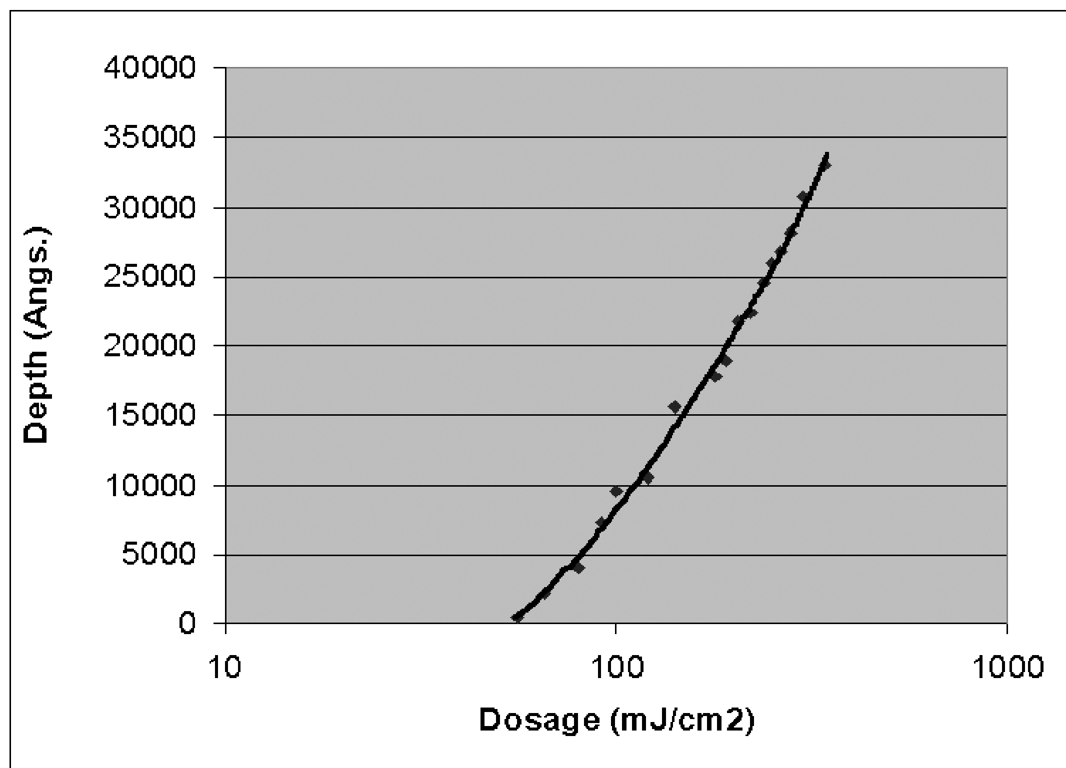

Figure 4.9 Exposure characteristic of Shipley photoresist SPR 220-3.0

are helpful on getting smaller slope in Figure 4.9. For binary lithography, a big slope is usually desirable because a steep wall is preferred. Here we can see that the parameter control of lithography process is more critical for gray-scale lithography. This is a big difference for the gray-scale lithography, compared with the binary lithography.

4.3.2 Dry-etching process

A Trion MINILOCK II ICP-RIE etcher was used to transfer the gray-scale patterns in the developed SPR220 resist into the substrate. Silicon was adopted as the substrate for all micro-structures in this chapter.

ICP-RIE can operate with higher plasma density at lower pressure, in comparison with conventional parallel plate RIE system. Higher plasma density and lower pressure allow for tighter control of anisotropy in etching high aspect ratio structures and for reduction of the micro/macro loading effect [47]. Micro-loading effect is also called RIE lag, which means narrower features etch slower than wider features. Macro-loading effect refers to a phenomenon, in which larger open areas in the sample are etched slower than the smaller open areas.

Etching for deeper micro-structures requires a higher etching ratio between the substrate and the resist. In our device fabrication process, we took an etching ratio of 5:1 between Si and SPR220. The etch parameters and etch rates are given in Table 4.2. SF_6 was the etching gas, O_2 was added to make the etching speed of SPR220 resist faster and H_2 helps to maintain an anisotropic etching.

Table 4.2 ICP-RIE Etching parameters used to obtain the etch ratio of 5:1 between silicon and SPR 220-3.0 resist.

$SF_6/O_2/H_2$	20.0/8.0/2.0 sccm
Pressure	30 mTorr
RIE/ICP power	60/30 W
Chilling water	5 Deg. C
Etch Rates	SPR 220 (100 nm/min)
	Silicon (500 nm/min)

4.4 Experimental results and discussion

4.4.1 Fabricated devices

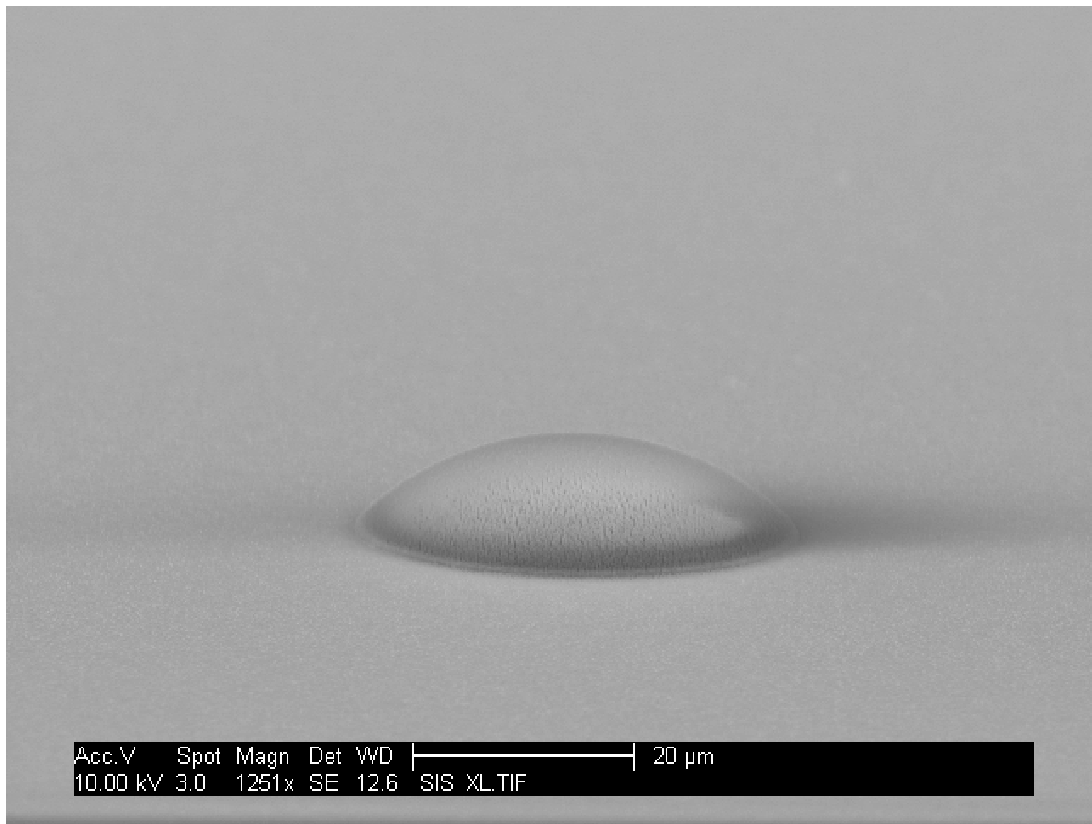

Figure 4.10 SEM picture of a parabolic lens fabricated in silicon

The parabolic lens shown in Fig. 4.10 has a diameter of about 45 microns and a sag of about 10 microns.

Fig. 4.11 shows the top view (slightly tilted) of a 2x2 retro-reflector array and Fig. 4.12 is the zoomed-in picture of a retro-reflector in the array. The retro-reflector

shown in Fig. 4.12 has a sag of 10.4 microns and its bottom side length is 27.6 microns. The array of retro-reflectors can reflect more light as a large retro-reflector does, but has a smaller thickness. An array of micro retro-reflector devices can find its application in small modulators for high-speed free space communication [44].

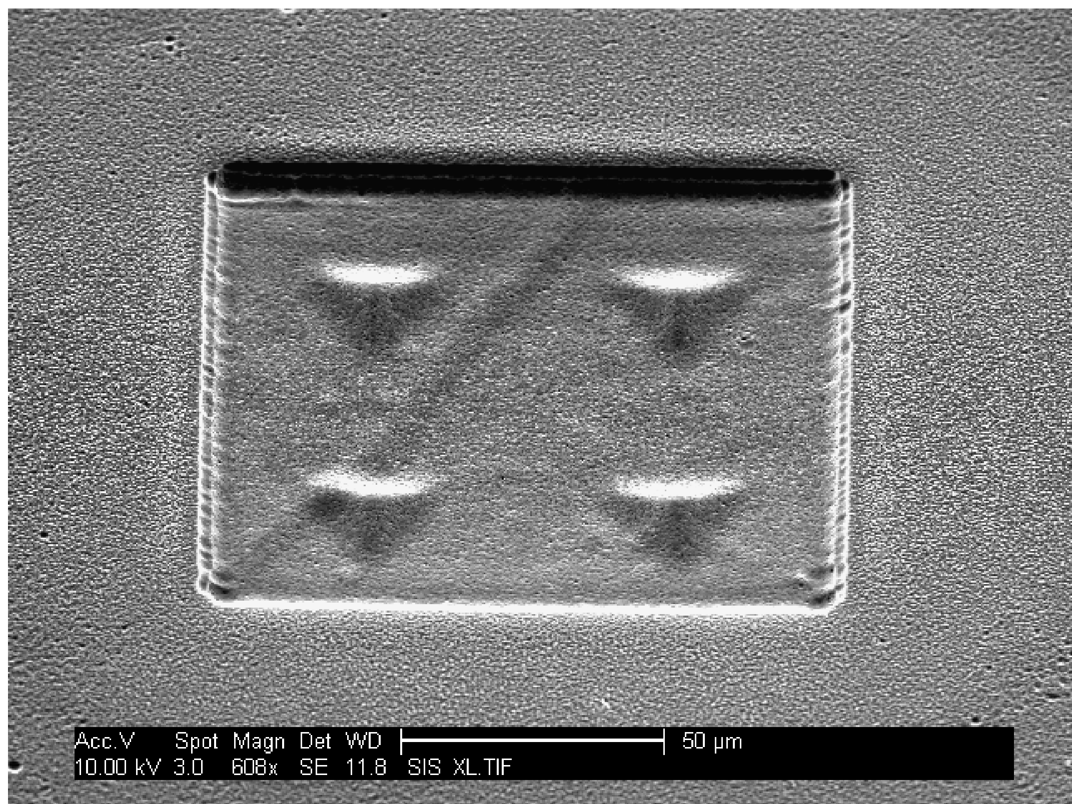

Figure 4.11 SEM picture of a retro-reflector array

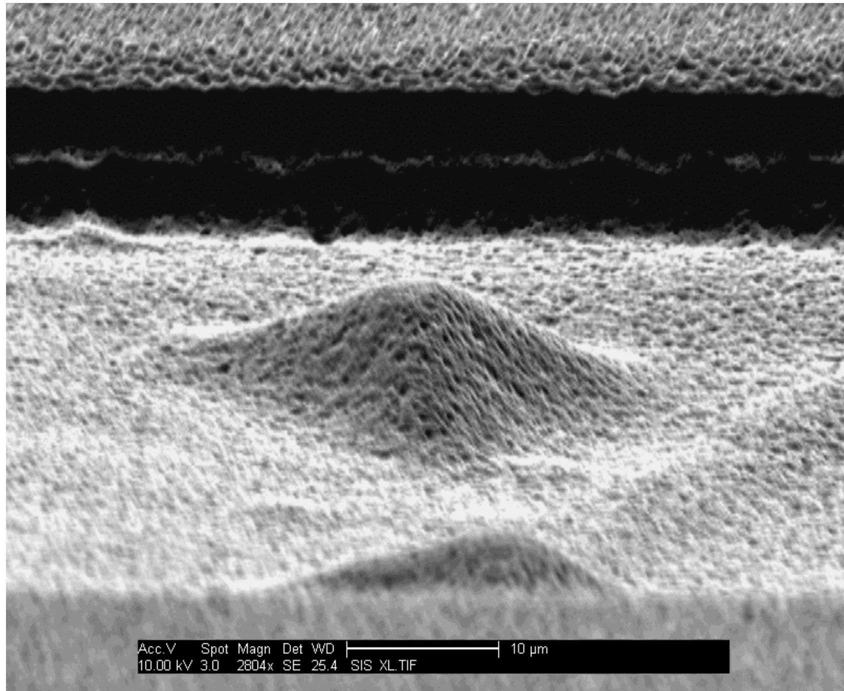

Figure 4.12 SEM picture of a retro-reflector

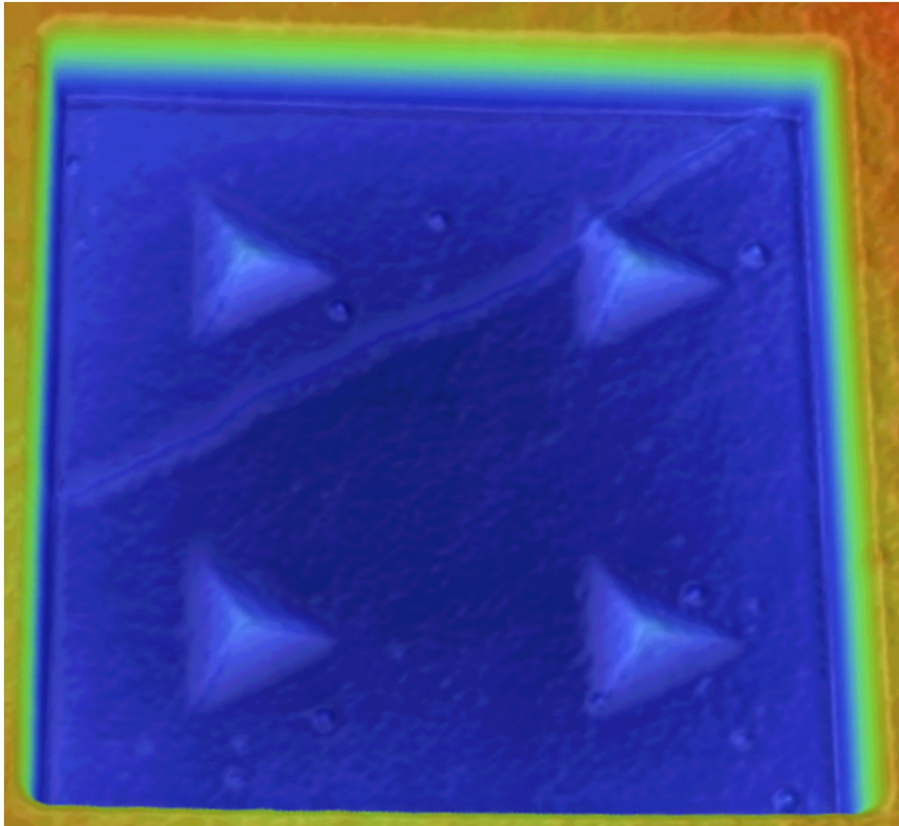

Figure 4.13 Picture of the retro-reflector structure on mask (side of the square frame is 120 microns in length)

The mask used to fabricate the retro-reflector structure in Fig. 4.11 is shown in Figure 4.13, taken on a Veeco NT1100 Optical Profiling System. The side length of the square frame is 120 micron and the sag of this retro-reflector structure on the mask is about 1000 angstroms. From Fig. 4.11 and Fig. 4.13, we can see that the structure was transferred from mask to Si substrate successfully.

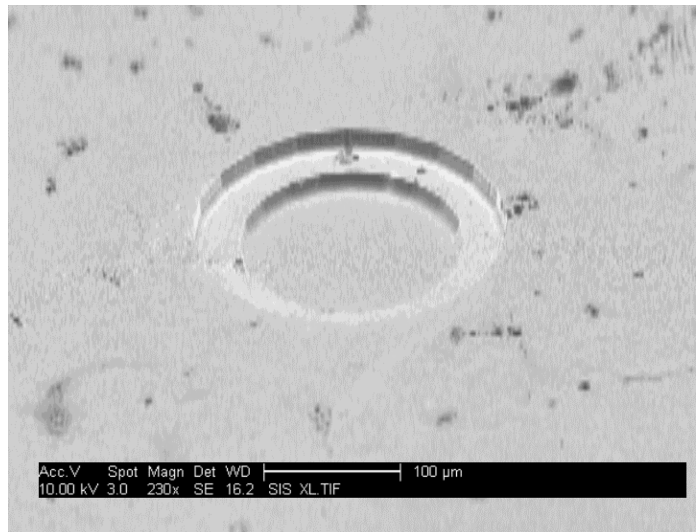

Figure 4.14 SEM picture of a via/pad structure

The via/pad structure in Fig. 4.14 shows a step width of 30 microns, which is much smaller than the current technical level (~200 microns) of High-Density Interconnection (HDI) technology in semiconductor industry. If needed the height of the intermediate step can be any values, varying from 1 256th to 100% of the total depth of via/pad structure, because of the multi-level capability provided by our gray-scale technology.

4.4.2 Comparison of device shape to design

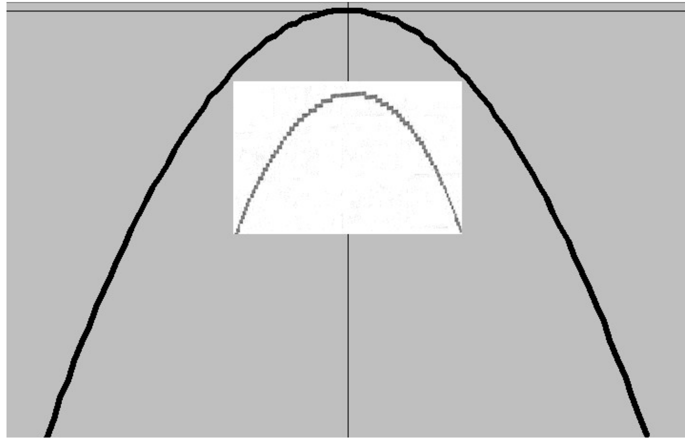

Figure 4.15 (a) Comparison of fabricated aspheric lens shape to the design

The final shape of a fabricated gray-scale device in silicon is determined, as discussed earlier, by the following factors: the optical transmittance profile of the gray-scale mask, the lithography parameters, and the dry etching parameters. When lithography and dry etching parameters are fixed, the shape of a gray-scale device in silicon will be solely determined by the transmittance variation in the gray-scale mask. In this way we can fabricate a gray-scale device with certain gray-scale shape by designing a gray-scale mask and using the mask in the fabrication process. As an example, Fig. 4.14(a) shows the comparison of the shape of a fabricated parabolic lens to the designed profile. The black line is a mathematically generated parabolic curve. The curve in the center white frame illustrates the shape of the fabricated

parabolic lens. The profile of this parabolic lens was measured on a DEKTAK 3030ST system. In order to better compare the similarity between the shape of the fabricated lens and the real parabolic curve, the profile of the fabricated device was re-scaled along y-axis. The re-scaling doesn't change the shape of the parabolic surface mathematically, in principle. From this figure, it can be seen that the shape of the fabricated parabolic device matches very well with the designed parabolic profile.

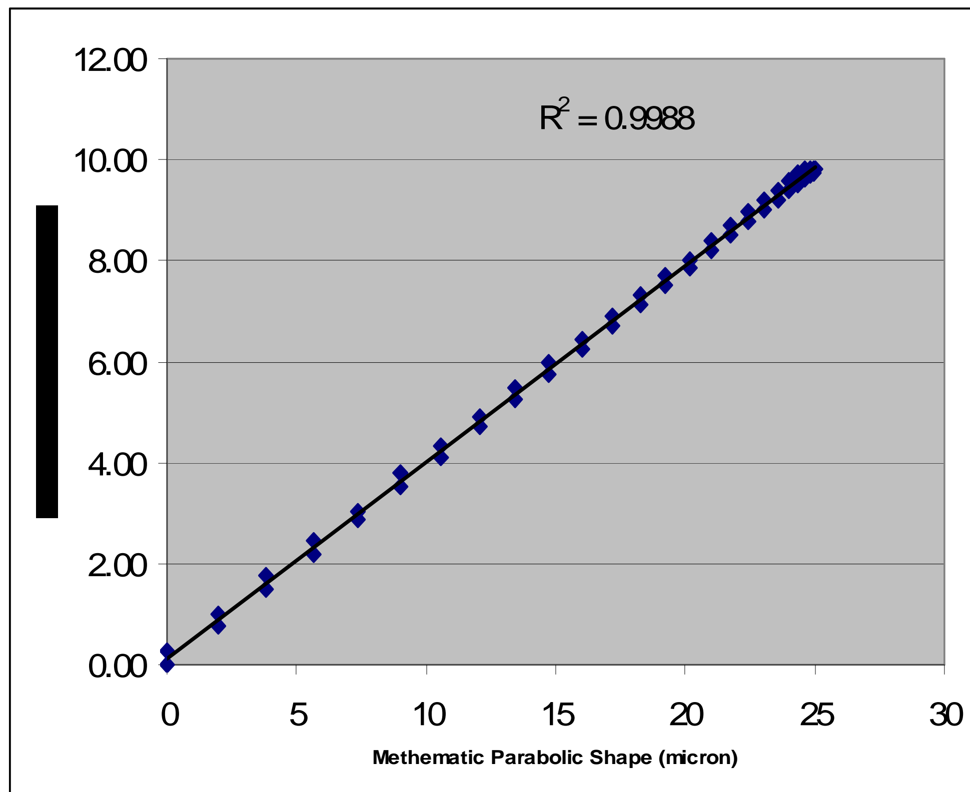

Figure 4.15 (b) Cross-correlation of fabricated aspheric lens shape to designed

Fig. 4.15(b) calculates out the cross-correlation of a fabricated parabolic lens to the designed profile. A value of 0.9988 of R^2 demonstrates that the fabricated lens shape is close enough to a mathematic parabolic shape.

4.4.3 Potential application of our new gray-scale technology in MEMS devices

To date gray-scale lithography technology has not yet been applied to fabricate MEMS devices with 3-D profile. Our gray-scale technology shows a good potential in MEMS field. For example our technology can be used to fabricate silicon-based micro bevel-gear, which has a lot of applications in micro-machines. Circular bevel-gear can transfer the mechanical rotation axis by 90 degrees, and linear bevel-gear can transfer the rotation movement to linear movement et al. By changing the gear design, while using the same gray-scale technology used in fabricating linear bevel gear, one can fabricate circular or even spiral bevel gears.

4.5 Conclusion

Several deep structures, e.g. aspherics, optical retro-reflector, and micro-via/pad, have been fabricated using our improved gray-scale masks. Together with the high-resolution shallower structures reported in Chapter 3, the improved gray-scale technology has demonstrated that it can be widely employed to fabricate various micro- and meso-structures with different depth for a wide range of applications.

To fabricate gray-scale devices with higher resolution, 248nm or 193nm lithography, instead of 315nm, is preferred. Compared with using 315 nm aligner, using 248/193 nm stepper for the same gray-scale mask would call some attentions here. First of all, the optical density of the mask would be higher for 248/193 nm for the same mask. So if the same optical density profile is needed, the carbon-based optical film should be thinner for 248/193 nm. Secondly, steppers usually have a de-magnification ratio, for example 2:1 or 4:1. This means the actual device structure would be smaller than the pattern shown on mask, if a stepper with a de-magnification ratio is used. This is a big difference between an aligner (1:1 ratio) and a stepper. A de-magnification ratio also means that any stitch shown on mask would be de-magnified in the final device, which is good if any stitch error exists in the mask. One more major difference for 248/193 nm lithography is that the resist used for DUV lithography is usually different from that used for 315 nm although all resists for gray-scale technology are required to have good analog properties.

5. Review of Other Research Ideas and Progress in This Project

At the very beginning of this project, we proposed to work with two collaborators (Yale University and Precision Instrument Development Center (PIDC), National Science Council of Taiwan) on LIGA-like process and Asymmetric Resonant Cavity (ARC) respectively. Although these proposed collaborations couldn't be finished due to the funding reason, the research ideas are still valuable in our mind. These ideas are reviewed here and will be done in future, if possible.

5.1 LIGA process and LIGA-like process

LIGA is the German acronym for X-ray LIthography (X-ray Lithographie), electro-deposition (Galvanoformung), and molding (Abformtechnik) [48, 49]. These three steps make it possible to mass-produce micro-components at a low-cost and are briefly summarized below. To produce the necessary X-radiation a very expensive set-up called synchrotron system needs to be used. The system consists of a several meter long ring structure in which electrons are accelerated. When reaching a certain velocity the rotating electrons emit X-rays perpendicular to their circular flight path. The emitted radiation is highly collimated and by placing an X-ray mask and substrate into the beam path, the mask structures can be transferred onto the substrate. Due to expensive synchrotron radiation used in LIGA technique, its application fields were limited. Therefore, several LIGA-like techniques were developed, for example UV-LIGA technique using UV lithography, DEM technique

using silicon deep etching and laser-LIGA technique using laser ablation. LIGA-like techniques have advantages of lower cost and shorter processing procedure in contrast to conventional LIGA technique.

5.1.1 Deep X-ray lithography and mask technology

X-ray lithography allows structures of any lateral design with high aspect ratios to be produced, i.e., with heights of up to 1 mm and a lateral resolution down to 0.2 μm. These structure walls are smooth and parallel to each other. The very sophisticated structures of this type can be produced lithographically only by a highly penetrating, intense, and parallel X-radiation supplied by a synchrotron. The structural information is compiled by the use of a CAD system and then stored on a mask that meets the special requirements of hard X-radiation; the "transparent" carrier of the mask is a very thin metal foil (e.g. titanium, beryllium), while the absorbers consist of a comparatively thick layer of gold. Synchrotron radiation is used to transfer the lateral structural information into a plastics layer, normally polymethylmethacrylate (PMMA), by "shadowing". Exposure to radiation modifies the plastic material in such a way that exposed material can be removed with a suitable solvent, leaving behind the structure of the un-exposed plastic (the "shadowed areas") as the primary structure. The development process and the ensuing electro-deposition/electroforming process impose stringent requirements on

the process technology because of the high aspect ratios and the resultant narrow, deep grooves in structures.

5.1.2 Electro-deposition

The spaces generated by the removal of the irradiated plastic material can be filled with metal by electro-deposition or electroforming processes. In this way, the negative pattern of the plastics structure is generated as a secondary structure out of metals, such as nickel, copper and gold, or alloys like nickel-cobalt and nickel-iron. This technique can be used to produce microstructures for direct use, but also tools made with nickel and nickel alloys for plastics molding.

5.1.3 Plastics molding

Plastics molding is the key to low-cost mass production by the LIGA process. The metal microstructures produced by deep X-ray lithography and electro-deposition/electroforming are used as mold for the manufacturing of faithful replicas of the primary structures in large quantities and at low cost. The materials used in plastics molding can be thermoplastics with very special optical properties (PMMA plexiglass, polycarbonate), or materials particularly resistant to chemicals (epoxy phenol resins, polyvinylidene fluoride (PVDF), and other fluoropolymers), or

polymers of high temperature resistance (such as polysulfones, polyether ketones), depending on the device application requirements.

5.1.4 Existing LIGA-like process in PIDC

LIGA-like process in PIDC is basically a laser ablation LIGA-like process. The Excimer laser micromachining system in Precision Instrument Development Center (PIDC), National Science Council of Taiwan is a PS-2000 system by Excitech Ltd. The system consists of a 248 nm KrF Excimer laser COMPEX 110, an optical beam shaping and projection subsystem, a servo-controlled motion stage and sample table, and a personal computer as the system controller. The short laser pulses generated by the KrF laser have typical pulse duration of 30 ns (FWHM) and the maximum laser energy is around 350 mJ/ pulse. Pulse repetition rate ranges from 1 to 100 Hz. Pair of cylindrical lenses and the homogenizers are included to shape the laser beam into a uniform intensity distribution over the cross-section. The laser beam is then passed through a photo-mask and projected onto the sample surface by a 10X demagnifing objective lens. The laser energy density projected on sample surface can be varied by either directly reducing the output laser energy or activating the laser attenuator. Maximum laser energy density is around 2 J/cm2. The sample is placed on a motorized table that can rotate and translate in all three axes (x-y-z) through the PC controller. The computer also triggers the output of laser pulses so that the laser pulse firing is synchronized with the movement of the sample table.

Programming software is provided with the micromachining system and users can program the table movement and laser firing sequence. A CCD camera is mounted on top of the objective lens to monitor the sample under machining. A beam profile viewer is included in the system for monitoring the homogeneity of laser intensity distribution. Excimer laser micromachining is two-dimensional and binary, which means each single laser pulse will remove a certain amount of sample material from the surface at those areas that are projected by the laser beam. The machining rate depends on laser energy density and the sample's material properties. The machined pattern on the sample is a duplicate of the contour pattern of the photo-mask with a down scaling factor of 10 under the help of the 10x demagnification lens. Laser-machined pattern is then replicated by electro-deposition/electroforming to obtain inverse metal molds. Finally, plastic devices are replicated from these metal molds using hot embossing method.

5.1.5 Proposed LIGA-like process for deep gray-scale devices

In our proposal, a gray-scale mask, instead of the normal binary mask, was proposed to be applied to the LIGA-like process in PIDC (Precision Instrument Development Center, National Science Council of Taiwan) for producing 3D gray-scale microstructures directly in PMMA or polymer material. In this proposal we would design and produce gray-scale masks first in UCSD for the 248nm Excimer laser employed in the LIGA-like process, and then researchers in PIDC would produce and test gray-scale devices based on the established LIGA-like processes in

PIDC. This proposal was submitted by our collaborators in PIDC to National Science Council of Taiwan; unfortunately it didn't get funded and supported. After we tested the heating effect of our mask material under the high power laser illumination and concluded that our mask material could withstand the laser ablation process and could be used in the Excimer Laser LIGA-like process, no further research could move forward due to the funding condition.

5.1.6 Brief review of latest progress and applications of laser LIGA-like process

C. H. Ho et al. reported a method to completely remove cross-linked SU-8 without remnants of the resist or destroying the electroplated microstructures in their LIGA-like process [50]. The LIGA-like fabrication of a side-driven electrostatic micro-motor was employed as an example to describe polymerized SU-8 resist removal. Using near-UV light, nickel components of the micro-motor were electroplated 160 mm in a 300 mm-thick SU-8 mold. A comparison of various approaches based on a commercial remover was performed during the mold removal process. Experimental results showed that components having 1 mm-deep substructures embedded in the substrate could provide stronger structures to withstand the internal stress due to the photoresist deformation. In addition, when the height of the electroplated structure was below two thirds of the photoresist mold thickness, the net clamping force on the resist could be effectively reduced to make

the removal of SU-8 with heated remover successfully. The rotor and the stator with embedded roots were released cleanly and thereby, assembled to form a high-aspect-ratio micro-motor successfully. The technique outlined in this paper solved the notorious problem of the hard-to-strip polymerized SU-8 resist. The LIGA-like process combined with the SU-8 removal technology presented in this work can be applied to simplify fabrication procedures and reduce the production costs of in other LIGA-like processes.

A manufacturing process of micro nickel/diamond abrasive pellet array lapping tools using a LIGA-like technology was reported by S. Y. Luo et al. [51]. The thickness of JSR THB-151N resist coated on an aluminum alloy substrate for micro lithography was up to 110 μm. During the lithography, different geometrical patterns in photomask were used to create specific design patterns of the resist mold on the substrate. Micro-roots, made by electrolytic machining on the substrate with guidance of the resist mold, can improve the adhesion of micro nickel abrasive pellets electroplated on the substrate. During the composite electroforming, the desired hardness of the nickel matrix inside the micro diamond abrasive pellets was obtained by the addition of agents for leveling and stress reducing. Under moderate blade agitation and ultrasonic oscillation, higher concentration and more uniform dispersion of diamond powders deposited in the nickel matrix were achieved. With these optimal experiment conditions, the production of micro nickel/diamond abrasive pellet array lapping tools was demonstrated in this paper.

A low-cost quasi-LIGA process was proposed by Q. Wang et al. [52]. Instead of using thick resist technique, micro-structure with large structural height is achieved by multilevel imprinting and through-mask plating. To achieve precise alignment between individual layers, an alignment system based on computer micro-vision is developed and the experimental results show average overlay accuracy within 1.5 μm with a standard deviation within 0.33μm. Good adherence of resist on seed layer was achieved with substrate surface oxidation and a coupling agent, which establishes tight chemical bond between substrate surface and the resist layer. The deposition uniformity was improved by electroplating process optimization to enhance the cathode polarization. Through electrolyze etching on previous layer before next level of metal deposition, the fresh metal surface is obtained and the bonding strength between adjacent metal layers was found to be improved. With the developed process, tri-layer photoresist and metallic structures with a pattern feature size of 20 μm were successfully fabricated. This quasi-LIGA process has a lower cost compared to LIGA process. In this technique the power requirement on exposure source is less stringent since the multilayer thin resist process instead of thick resist technique is adopted.

An eight-level diffractive microlens (DML) array for beam splitting was designed and fabricated in a LIGA-like process by J. J. Yang et al. [53]. The LIGA-like technique was used in this study to produce a polymer DML. First, the DML pattern was fabricated on a silicon wafer as the master. The silicon master was then

transferred onto a Ni mold by micro electroplating. Finally, with this precision mold, the DML structure was replicated onto a PMMA substrate by hot embossing. The pattern of this dual-focal-point DML was designed using the optimal rotation-angle method and realized by silicon etching, nickel (Ni) electroplating and hot embossing. Tetraethoxysilane (TEOS) oxide etching and specially designed de-mold techniques were developed and employed in the fabrication process to minimize the related processing errors such as misalignment and tilting so that the accuracy of DML could be ensured. The obtained PMMA-based DML was measured to confirm the optical properties and the results showed that the diffraction efficiency error and uniformity error were successfully kept under 5.19 and 1.52%, respectively.

Y. C. Lee et al. reported their progress on fabricating spherical and aspheric micro-lenses using Excimer laser LIGA-like Process [54]. This paper presented an effective and low-cost method for fabricating spherical and aspheric micro-lenses based on Excimer laser LIGA-like processes. It was based on a newly developed Excimer laser micromachining method that can accurately machine a 3D microstructure with a predetermined continuous surface profile. The method is called the planetary scanning method since it is based on a combination of sample rotation and revolution and a concept of laser machining probability. Spherical and aspheric micro-lenses with precise and smooth surface profiles are fabricated by direct laser machining on polymer materials. Laser-machined micro-lenses are replicated by electroforming to obtain inverse metal molds. Finally, plastic micro-lenses are

replicated from these metal molds using hot embossing method. The profile accuracy and surface roughness of the produced micro-lenses at each stage have been measured and monitored. The average surface profile accuracy was better than 1 μm and average surface roughness was less than 10 nm. Optical performance of the fabricated micro-lenses was evaluated by measuring the light intensity distribution at the focal plane and the focal length. Experimental data showed that the characteristics of fabricated spherical and aspheric micro-lenses were well matched to the theoretical predictions, which demonstrated the controllability and accuracy of this micromachining process. The idea of this Excimer laser LIGA-like process for 3D micromachining is to keep the mask or the sample moving when the laser pulses are continuously firing. Superposition of the 2D machined patterns generates a machining depth variation on the sample surface and therefore a 3D structure is created. For fabricating axially or circularly symmetrical 3D microstructures, rotation of the sample is a good choice for it can average out the slightly uneven laser energy density over the projected area and assure a truly symmetrical surface profile. This paper demonstrated a novel way for obtaining micro-lenses with precise control on their machining surface profile and surface smoothness. The surface profile can be of any axially symmetrical shape. This is particularly useful for designing refractive micro-optical elements and for optimizing their optical performance. This method can also be extended to non-axially symmetrical microstructures by scanning along a noncircular orbit, in principle.

5.2 Asymmetric resonant cavity (ARC) device

5.2.1 Overview of concept of asymmetric resonant cavity (ARC)

In 1994 a new class of optical resonator that comprises convex dielectric bodies that are substantially deformed from spherical or cylindrical symmetry was proposed by J. U Nockel et al. in R. K. Chang's group at Yale, [55]. They theoretically demonstrated that such asymmetric resonant cavities (ARC) still retain high-Q (Q >1000) whispering gallery (WG) modes up to distortions as large as 50% of the un-deformed radius R. At the same time their ray simulations indicated that the emission pattern from these modes becomes highly anisotropic. They developed a ray dynamics model for the emission pattern and present numerical and experimental confirmation of the theory [56].

The possible practical applications of such resonators always exist in optics or optoelectronics. Dielectric micro-spheres or micro-disks already provide compact high-Q resonators which may be useful as spectral filters or as components in micro-cavity lasers. There are three advantages that ARCs may provide: 1) The ability to tune the Q-value and resonant frequency of the cavity by appropriate deformations; 2) If this deformation can be done in situ, then the possibility of designing a Q-switched ARC micro-cavity laser; 3) The ability to couple a high-Q WG mode out of the cavity with strong directionality.

However, the fabrication of ARC device is very challenging due to the complex, non-symmetric shape of the device. Our gray-scale technology offers a great potential for fabricating ARC devices, from the technology point of view. Collaboration was sought with Yale researchers for the fabrication of ARC microstructures using our gray scale technology. Dr. Chang's group at Yale proposed to design and test ARC devices for us while we fabricated the ARC devices for them. Unfortunately Dr. Chang's group didn't get funded for this idea and didn't have resources to design and test real ARC devices together with us.

5.2.2 Proposed ARC structures to be fabricated using gray-scale technology

We proposed to study novel photonic devices based on the ARC concept and fabricated by gray-scale technology. Specifically we proposed to test and demonstrate the following important features:

i. Improved lasing characteristics of ARC micro-lasers over a range of wavelength bands and gain materials;

ii. The possibility of lasing emission from ARC micro-lasers from two qualitatively different modes, i.e., different in both emission directionality and wavelength;

iii. Demonstrate similar properties for ARC-based optical amplifiers;

iv. Improved input-output coupling between waveguides and ARC micro-resonators due to non-evanescent coupling to ARCs, resulting in much improved design tolerance;

v. Demonstrate how to exploit unique directional properties of ARC resonances for filtering operations useful for wavelength division multiplexing (WDM) applications in planar integrated optics;

vi. Demonstrate device configurations which convert planar propagation or emission to propagation or emission perpendicular to the plane. Configurations proposed are ARCs with auxiliary meso-reflectors, or axicon-domed ARCs. These configurations rely essentially on unique features of gray-scale technology.

In this collaborative project, we proposed that Yale would be responsible for defining the shapes, sizes and materials of ARCs to be fabricated and UC-San Diego would be responsible for the fabrication of ARCs and sample examination. Yale would measure the fabricated ARCs in terms of their performance and provide feedback to the Yale design group and UC-San Diego (fabrication group), while focusing on possible application to the integrated optics field and WDM part of the telecommunication field.

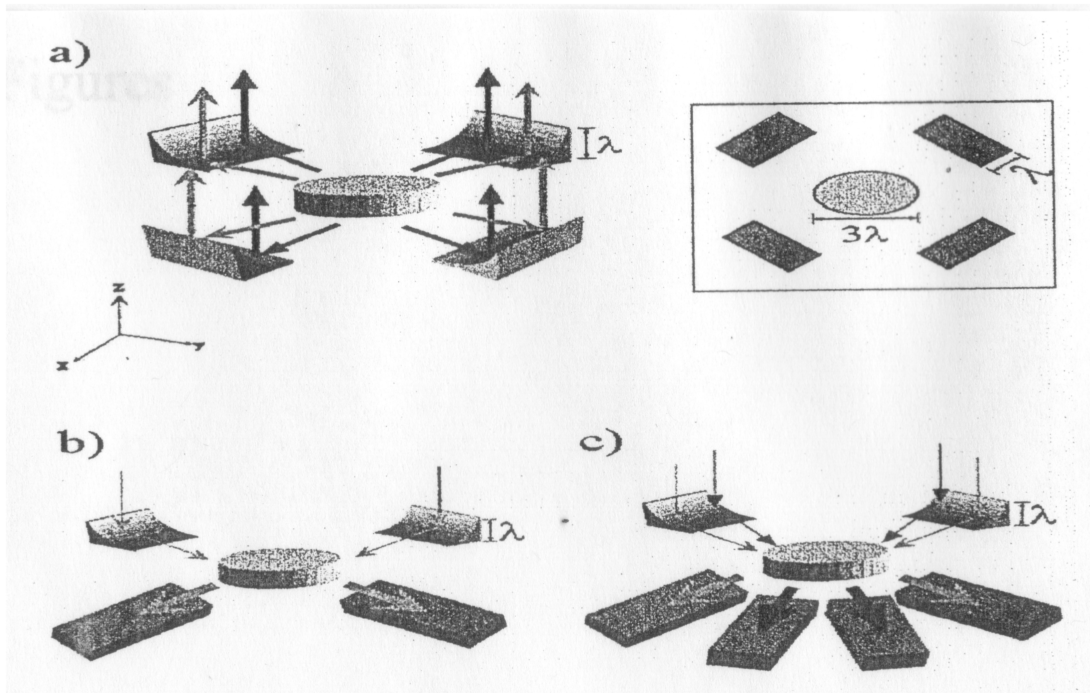

Figure 5.1 (a) Micro optical reflectors, directing the ARC laser emission propagating in the horizontal plane to propagating in the vertical direction. Top view of an ARC-reflectors surface-emitting unit shows a relative scale in units of operation wavelength; (b) Micro reflectors directing the input signal into the ARC amplifier and the amplified signal to optical waveguides; (c) Amplified signal from different resonant modes, and hence, different frequencies and directionality, propagate into different waveguides.

Some interesting applications of ARCs with large deformations, for which the coupling is essentially refractive, are shown in Figure 5.1. In Figure 5.1(b) and Figure 5.1(c) the light can be coupled into the resonator with propagating as opposed to evanescent waves. The refractive coupling to ARC resonant modes would eliminate the necessity of fabricating precisely aligned sub-micron features and greatly improve the tolerances of any devices based on ARCs. Clear demonstration of this new approach was one of the major goals in the proposal. In addition micro-

optics can be designed to direct the input light to couple refractively into the ARC resonant modes, or to redirect the refractive ARC resonant emission. Potential on-substrate redirection of the ARC planar directional emission to the vertical surface emission should then be possible, as shown in Fig. 5.1(a). With the possibility of controlling the input-output coupling and spectral content by varying shape, refractive index and lasing mode, the micro-pillar ARC should be a superb photonic component in a planar geometry.

The unique property of directional emission of ARCs has been demonstrated experimentally at Yale in the visible wavelength using liquid droplet deformed by gravity when they fall in air and in liquid dye jets shaped by rectangular orifice [56]. However lasing and amplification in other important wavelength bands with ARCs of different gain materials, cavity shapes and sizes have not yet been realized yet. The techniques employed to produce ARCs in deformed lasing liquid droplets and jets, while useful for probe basic physics, did not involve any fabrication process relevant to producing solid ARCs. Further investigations of ARCs for both active and passive applications require high-resolution lithography and fabrication technologies to produce ARCs of well-defined shapes and sizes in solid materials with different refractive index. Resolution should be as high as sub-micron; the shape can be 3D with asymmetric cross-sections and well controlled height profiles and the sizes can range from a few microns to several tens of microns. The ARC materials can be glass (e.g. Er-doped), GaAs, InGaAs/GaAlAs, and

silicon/germanium et al. Our gray-scale technology offers all of these capabilities in principle. Figure 5.2 shows a collection of ARC examples that require gray-scale technology to fabricate.

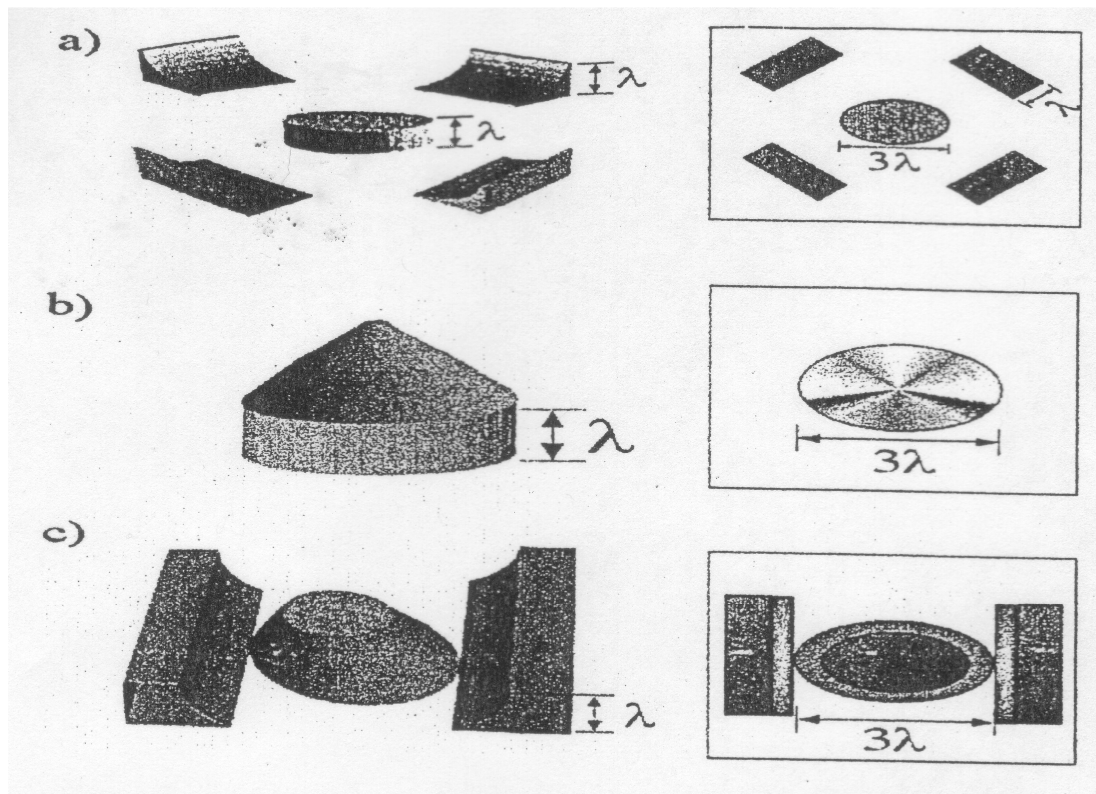

Figure 5.2 A collection of the proposed 3D oval or stadium-shape cross-section ARCs and gray-scale-side wall photonics components that are difficult for binary lithography, but easy for gray-scale lithography to produce. (a) Micro-reflectors with ARC micro-laser; (b) Axicon dome ARC amplifier; and (c) Skirted-side wall waveguide-coupled ARC filter.

It was a very deep regret that this collaboration proposal was not funded. The ideas mentioned above are suggested to be practiced in future, if possible.

6. Discussions and Summary

6.1 Differences between gray-scale and binary technologies

Although the same four steps, i.e., e-beam lithography, mask fabrication, optical lithography and device fabrication, are required in both gray-scale and binary technologies, there are many differences between the two technologies.

6.1.1 E-beam lithography

Binary mask requires only one dosage to clear the designed pattern area in resist, while gray-scale mask needs a gray-scale dosage profile or multiple e-beam dosages to generate gray-scale pattern in the resist.

Developing of gray-scale patterns in e-beam resist requires precise control on when to stop the resist developing, to ensure that no over-developing or under-developing would happen. Over-developing of resist would cause a lost of some gray-scale levels at the largest exposure dosage (for positive resist), while under-developing would cause a lost of some gray-scale levels at both the largest and the smallest dosages (for positive resist).

6.1.2 Mask fabrication

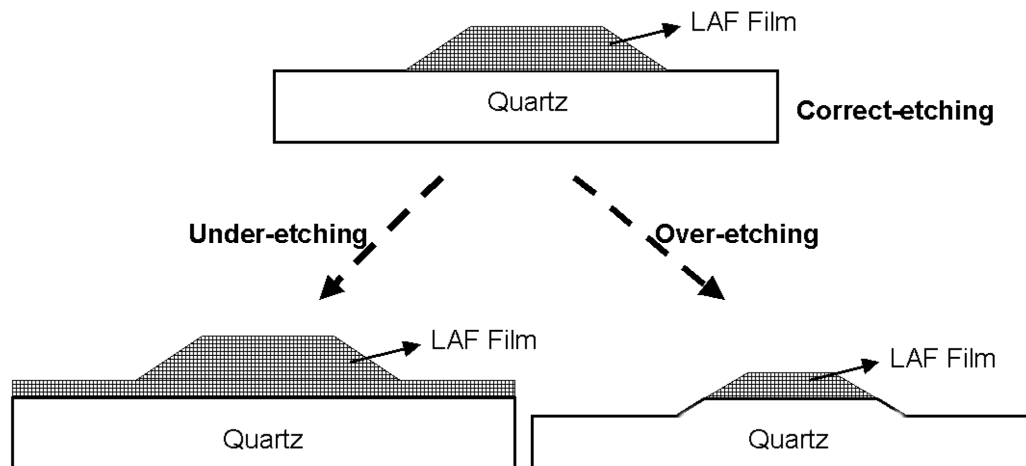

Figure 6.1 Effects of under-etching and over-etching of gray-scale mask

Binary technology can tolerate some over-etching in the mask fabrication process. Gray-scale mask fabrication requires very precise control on when to stop the etching process, to ensure that the e-beam resist is fully etched away (i.e. no under-etching) but without over-etching at the same time. Figure 5.1 illustrates the effects of over-etching and under-etching. Overheating of e-beam resist could also a problem for gray-scale technology, while binary technology doesn't care the temperature of resist at all. Even though the e-beam resist is usually very thin, if etching speed of the resist is too slow and the resulted etching time becomes too long, a carefully studied etching recipe is still needed for gray-scale technology.

6.1.3 Optical lithography

While binary lithography can tolerate some over-exposure or under-exposure, gray-scale lithography must require precise control on the exposure dosage. Gray-scale lithography also requires more precise control on the resist developing time. Over-developing would wash off a portion of the gray-scale structure. In comparison, over developing of binary patterns in resist could likewise make the resist thinner and the developed area larger, but one still have a binary structure.

6.1.4 Dry etching in device fabrication

More care must be exercised in transferring the gray-scale patterns in an optical resist into the substrate without distortion of the gray-scale profile, especially in fabricating deep (> 5 microns) microstructures. Over-heating of the resist can dramatically change the etching speed of the resist, thus distorting the gray-scale profile. Also the resist needs to be completely etched off so that the entire gray-scale structure is transferred into the substrate. For binary etching, over-heating and left-over of resist is not much a problem at all.

6.1.5 Wavelength of optical lithography

To fabricate devices with higher resolution a 248nm or 193nm stepper, instead of a 315nm contact aligner, is preferred. Usually an improved gray-scale

mask has its own application wavelength. For example a gray-scale mask designed for 248nm wavelength cannot be used for 315nm lithography process, because the optical density profile is totally different at these two wavelengths for the gray-scale mask. For binary technology, the restriction of wavelength for the mask is much looser. A binary mask can usually be used in different lithography systems with different wavelength, without causing a big problem.

6.2 Issues of device surface quality in gray-scale technology

Surface quality issue is one major concern for a user of gray-scale technology. A smooth surface for the device is always preferred for optical devices. Even for MEMS devices, people are paying more and more attention on the surface quality issue. In general each step of the gray-scale technology has a contribution to the surface quality of the final device.

In the device design step, more gray levels per unit usually means better surface for the gray-scale mask first, and for the fabricated device later. This topic was discussed in Section 4.2 in detail. Basically we need to know how deep and how big the device will be, and how many gray-levels we need to get a reasonable surface quality. If the required amount of gray levels is beyond the capability of the e-beam system to be used, the computer-generated file may need to divide the device into multiple portions so that each portion can have enough gray levels to guarantee the surface quality.

Once the device design and the computer generated file are done, we will move to the e-beam writing step. In this step, we wish to use an e-beam resist, which has a good analog exposure property, for the writing of the gray-scale mask. This means the e-beam resist should have a large dynamic range of exposure. The dynamic range of exposure for a chosen resist is a function of the resist developing condition. In general lower developing temperature and diluted developer can make the dynamic range of exposure larger for the same e-beam resist. This analog property requirement and general principle of resist developing are also applied to the optical resist used in the optical lithography step. The size of electron beam also plays a role on getting smoother surface. In general, a larger (compared to the pixel size) beam diameter means that there will be some overlapping between adjacent pixels and this would help to smoothen the surface of developed e-beam resist.

After pattern is written in the e-beam resist and the e-beam resist is developed properly, we need to etch the pattern in the e-beam resist into the carbon-based mask material. It is easy to understand that a careful etching can give a better surface for the gray-scale mask. Here the general idea is to keep the etching speed a little bit slower so that the etching would be more uniform and smoother.

Now we are in the optical lithography step. In this step we would require a good analog resist and a suitable developing condition for the exposed resist. This requirement is the same as we stated for the e-beam lithography. A slower

developing speed is generally good for getting better resist surface here. A lower temperature for the developer and a diluted developer are all helpful to make the resist developing process slower.

The dry etching of gray-scale patterns from optical resist from substrate is quite different from the dry etching of gray-scale mask. The etching depth of gray-scale mask material is only about 300 nm, while the depth of devices is in the range of 1 to 20 microns. So the etching time is much longer and more difficult for the dry etching of devices. In general we need to pause the etching processing periodically (e.g. every 5 minutes) so that the temperature of un-etched resist and substrate won't be too high. Big fluctuation of temperature for resist/substrate usually means non-uniform etching speed and this doesn't help on getting smooth device surface. The amount ratio between F^- ions to H^+ ions in etching plasma is also a key to the etching speed and the anisotropic nature [57, 58, 59, 60, and 61]. More F^- ions in the plasma usually mean faster etching speed, while more H^+ ions in the chamber usually slower etching speed. This is because of the H^+ ions participate the polymerization process and the re-deposition of polymer-like material slow down the etching speed. The re-deposition on the sidewall of the etched trench also helps to maintain an anisotropic etching. In this device etching step, the etching speed needs to be optimized (neither too slow, nor too fast) in order to get better surface for the fabricated devices.

6.3 Review of dry etching techniques and progress for deep structures in Si/SiO_2

Dry etching is very critical for the success of gray-scale technology. The three key steps of gray-scale technology are: (1) gray-scale mask design, (2) gray-scale lithography and (3) dry anisotropic etching. Steps (1) and (2) produce a precisely designed 3D profile in a photoresist-masking layer by modulating the intensity incident on the photoresist surface. Step (3) allows the 3D profile in the photoresist to be transferred into the underlying silicon substrate by dry anisotropic etching. A smooth surface is usually required for optical devices and many other devices. In early days gray-scale patterning was primarily used for defining diffractive optical elements (DOEs) where etch depth requirements are typically shallow and the structure can be etched using regular reactive ion etching (RIE) or ion milling. In micro-electromechanical systems (MEMS) and other devices with deep depth, deep reactive ion etching is needed to extend gray-scale technology to the depths required by different applications. How to get smooth surface in different substrate materials, when a deep anisotropic etching is needed, is always very challenging. Keeping improving the dry etching technique and getting a smoother device surface is a permanent topic for gray-scale technology. In Chapter 4 the surface quality of devices with deep structure in silicon is not very satisfactory, so in this section a review of different drying techniques and how these techniques improve the surface quality in deep silicon etching are presented.

Most plasma etching processes primarily rely on RIE for material removal. Reactive ion etching involves simultaneous bombardment of energetic ions and reactive neutral radicals on material surface. As demonstrated in experiment the etch rate is much larger in the presence of both ions and neutrals as compared to ions or neutrals alone. Since ions primarily gain their energy in the sheath above the substrate, they bombard the substrate surface almost in normal direction. Therefore etching occurs preferably in the normal direction (i.e., anisotropically). In this way one can fabricate structures that have vertical sidewalls. Reactive ion processes is usually less selective compared to chemical etching processes due to the presence of energetic ions but more selective relative to physical sputtering because of the partially chemical nature. Work in recent years has shown that, depending on the ion, neutral, and material, RIE can occur in several different manners. For a simple system such as Cl etching of Si, neutral radicals chemisorb on the material surface and form weakly bonded compounds. Energetic ions are then able to dislodge these compounds from the surface and generate volatile products. Reactive ion etching phenomenon tends to be more complex for fluorocarbon etching of silicon or dielectrics. In these etching systems, a thin fluoro-carbon film forms on surface of the material. Although etchant atoms (C and F) exist in this fluorocarbon layer, ions are necessary to modulate fluorocarbon film thickness and enhance etchant and product diffusivity through the reactive layer. Surface reactions therefore do not occur when energetic ions are not present.

Reactive ion etching (RIE) tools are characterized by a large (> **2**:1) area ratio between the anode and cathode, operating in the 10-400 mTorr range and designed in both single wafer and batch configurations. Important components of an RIE etch tool includes a blocking capacitor is in series with the power supply. The wafers are placed on the cathode (the smaller, powered electrode). These are the tools which support virtually all high resolution pattern transferring etch processes in the semiconductor industry. The low pressure operation provides good mass transfer which reduces micro- and macro-loading effects. The diode performance of the plasma provides high ion energy at the wafer surface for ion-assisted etching, and low ion energy at the anode for reduced sputtering of the chamber walls. People adjust different parameters to obtain different wafer etching results and keep the equipment operational in production. Most RIE systems currently available are evolutionary in that they represent continuously improved developments of a mature technology.

For gray-scale deep structures, the etching selectivity is usually big so thin photoresist-masking layers can survive deep etches while maintaining good etch characteristics such as vertical profiles, fast silicon etch rates, and smooth surfaces. In this case, silicon masked by thin photoresist will begin etching process before the silicon masked by thicker photoresist. Therefore the ability to control etch selectivity is necessary to precisely transfer the entire photoresist pattern to the desired depth. C. W. Waits et al. reported their progress on fabrication of 3D silicon MEMS structures

using gray-scale lithography and deep reactive ion etching (DRIE) [62]. This paper investigates the transfer of gray-scale patterned photoresist structures into silicon by DRIE. Effects of DRIE process parameters on etch selectivity between photoresist and silicon is evaluated. Additionally, the non-uniformity of photoresist and silicon are analyzed as well as the surface roughness of the final etched silicon surfaces. The results will serve as a guide for tailoring the etch selectivity in DRIE for developing 3D silicon structures with better precision. From these investigations, a micro-compressor is designed and demonstrated using gray-scale patterning and DRIE. In this study, the tailoring of etch selectivity for precise fabrication was investigated. Combination of SF_6/C_4F_8/Ar chemical gases, silicon loading, the introduction of an O_2 step, wafer electrode power, and wafer temperature are evaluated and determined to be effective for coarsely controlling etch selectivity in DRIE and decreasing the device surface roughness. The non-uniformity and surface roughness characteristics are evaluated and found to be scaled by the etch selectivity when the 3D profile is transferred into the silicon. A micro-compressor is demonstrated using gray-scale lithography. DRIE showing that etch selectivity can be successfully tailored, and the non-uniformity and surface roughness can be minimized for such a specific application.

J. W. Bartha et al. studied low temperature etching of Si with SF_6/O_2 using a Distributed Electron Cyclotron Resonance (DECR) system and a special Helicon type plasma source [63]. Si etch rate of 5 μm/min with Si/SiO_2 etch selectivity well

above 100/1, anisotropic profile and smooth surface, was obtained. Isotropic etch profiles obtained with SF_6 alone, even at temperatures below -120 °C. Anisotropic etch profiles are obtained by an addition of O_2. Therefore a sidewall passivation mechanism was proposed to explain the reduction of the lateral etching. The DECR reactor, in contrast to ECIL or Helicon reactors does not consist of quartz. These quartz parts, which enclose the high density plasma of the reactor types mentioned above, might show significant erosion. This erosion corresponds to homogeneous or heterogeneous chemical decomposition of the quartz material. The effective oxygen addition might be equivalent to several sccm O_2 for a helicon type reactor. In this paper the substrate temperature was varied from -50 to -100°C and no significant variation of the SiO_2 etch rate was observed. However a transition in the etch profile from isotropic to anisotropic is fully achieved at around -100°C. It was believed that this kind of source offers unique advantages over classical RIE or conventional high density plasma sources. Besides a wide operating pressure range and a high plasma density (1 to 5 Pa; 0.5 to $5x10^{12}$ ion/cm^3) it offers, with respect to low temperature Si etching, the possibility to control the oxygen flow, and correspondingly the etch profile. As a consequence of the high plasma density, plasma sheath thickness is typically one order of magnitude less than those obtained in capacitive discharges. Since the ion path is dramatically reduced, high bias is not needed to overcome the loss of ion directionality due to collisions. Thus very low levels of bias, compatible with zero damage etching and obtain a high selectivity towards oxide layers, with anisotropic profile and smooth surface were obtained.

Reactive ion etching (RIE) of silicon using SF6/O2/CHF3, plasmas was studied by R. Legtenberg et al. [64]. Anisotropic etching of high aspect ratio structures with smooth etch surfaces in silicon was reported in this paper. The technique was applied to the fabrication of three-dimensional micro-mechanical structures successfully. Etching behavior was found to be related to loading, the cathode material, and the mask material. Good results with respect to reproducibility, surface smoothness and uniformity were obtained by using silicon as the cathode material and silicon dioxide as the masking material for mask designs. Etch rate, selectivity, anisotropy, and self-bias voltage were examined as a function of SF_6 flow, O_2 flow, CHF_3 flow, pressure, and the RF power, using response surface methodology, in order to optimize anisotropic etching conditions. Measurements indicate that anisotropic etching results from sidewall passivation by silicon oxide species. It was reported that the anisotropic etch mechanism was based on ion-enhanced inhibitor etching. SF_6 provides the reactive neutral etching species in the form of F atoms. O_2 supplies the inhibitor film forming species that passivate the surface with a SiO_xF_y layer. SF6 and CHF3 generate ion species that suppress the formation the inhibitor film at horizontal surfaces. The addition of CHF_3 can be used to produce smooth etch surfaces in the anisotropic regime and is useful for a fine tuning of the anisotropy.

I. W. Rangelow et al. investigated fluorine, chlorine, and bromine containing gases for micro-electrical mechanical system fabrication in reactive ion etching [65].

In this paper a conventional planar RIE (reactive ion etching) reactor was used, in some cases with magnetic field enhancement or an inductive coupled plasma source and low substrate temperature. For RIE based on Cl_2 or Cl_2/HBr plasma a slightly ‘‘positive’’ (top wider than bottom) slope is achieved when etching structures with a depth of several 10 mm, whereas a ‘‘negative’’ slope is obtained when etching with an SF6 /CCl_2F_2-based plasma. A pattern transfer with vertical walls is obtained for RIE based on SF_6 (with O_2 added) when maintaining the substrate at low temperature (about -70°C). In order to obtain high aspect ratio structures with RIE, the ratio of ion flux and radical flux is of decisive influence: Highly anisotropic etching is driven by ion assisted reactions at the bottom surface, but is hindered by undercutting caused by reactive radical induced sidewall reactions. When aiming for high aspect ratio structures, miscellaneous phenomena occur which are not commonly observed when etching low aspect ratio (<3:1) features. The significant of these are aspect-ratio-dependent effects such as RIE lag, bowing, faceting, micro-trenching, and profile-shape dependence. These effects are caused by several mechanisms including: angular dispersion of ions and neutrals due to collisions within the plasma sheath; ion and etchant transport within the feature onto the sidewalls; depletion of the reactant under conditions of high reaction probability at the surface; charging of feature sidewalls, as local charging of substrate surface or microstructure sidewalls can deflect ions and thus may prevent them from reaching the bottom surface to be etched; etching yield dependencies upon the angle of incidence; deposition of the material produced in the discharge within the feature; re-deposition of material

released by ion-induced. The choice of gas phase chemistry, pressure conditions, reactant transport to the surface, and product transport away from the surface have been identified as the key factors for controlling the microscopic etch uniformity in the high aspect ratio etching. In order to reduce the above-listed detrimental effects, Efforts were focused on two main etching strategies: one is the controlled formation of sidewall-inhibitor films, and another is RIE etching at low substrate temperatures. RIE based on Cl and Br plasma chemistries may achieve highly anisotropic structures due to the low reaction probabilities of chlorine or bromine radicals with Si at room temperature. The etching is due to the ion-bombardment-induced chemistry at the bottom surface, where an ion energy as low as 25 eV is sufficient. The sidewalls are protected by radicals of absorbed atoms/molecules of non-fluorine halogens. Plasmas such as Cl_2/BCl_3, $Cl_2/BCl_3/HBr$, Br_2/CF_3Br, and $Br_2/HBr/Ar$ have been found to be most appropriate. Using a SF_6 plasma, Si etch rates of 1 μm/min may be achieved even at low RF power densities of 0.15 W/cm^2. This is due to the high reaction probability of fluorine with silicon which is much higher than the probability of a reaction between Si and any of the other halogens (Cl, Br, I). Subsequent to a scavenger step the anisotropic main etching process is based on a SiO_xF_y film which is sputtered from the bottom surface and re-deposited onto the sidewalls. This process is possible by adding oxygen to SF_6-based plasmas. To prevent the formation of black silicon due to oxidation of the slightly halogenated bottom silicon surfaces, scavenger gases such as CHF_3 are added to the plasma. RIE of Si at low substrate temperatures offers decisive advantages for fabrication of deep

structures with high quality surface. In the experiments reported in this paper RIE was performed with an electro-statically shielded ICP source (inductive coupled plasma from Oxford Plasma Technology). Liquid nitrogen was used as cooling source for the cryotable. This source supplies a uniform cooling across a wide temperature range, realized due to controlled liquid nitrogen flow and integral electrical heater design. When keeping the substrate at low temperature, fluorine is much less penetrating into Si lattice than at room temperature, reducing spontaneous reactions which form volatile products. Halogenated products are formed readily reacting with oxygen on the Si bottom surface. Ion-induced re-deposition causes a silicon–fluorine–oxide passivation layer to be condensed onto the sidewalls. In this paper 10% of oxygen added to the gas mixture was found to form an effective sidewall passivation.

H. C. Liu et al. investigated the sidewall roughness control in advanced silicon etch process using an ICP-RIE system [66]. In this paper, experimental investigations were done on fabrication parameters in the STS advanced silicon etch (ASE) process for decreasing sidewall roughness. In the experiments, several parameters, including over time, ramping time, Ar flow rate, platen power and etching cycle time, were systematically studied. It was found that sidewall mean roughness can be down to 9.1 nm at etching rate of 2.5 μm/min. A series of experiments were performed to improve the sidewall roughness with reasonable silicon etching rate and sidewall profile by adjusting various parameters in a STS

ICP-RIE system. I was found that the mean roughness can be effectively decreased by adjusting SF_6 flow rate, etching cycle time, Ar flow rate, platen power, ramping time, and over time. When Ar flow rate is between 5% and 10% of SF_6 flow rate, platen power is 12W, and over time is 2s, a smoother and better perpendicular sidewall surface can be achieved. Using this recipe, the sidewall mean roughness is reported at 9.1 nm with etching rate 2.5 μm/min in this paper.

The uniform distributed electron cyclotron resonance (UDECR) plasma of SF6, excited at either 2.45 or 5.85 GHz, was applied to study the etching of SiO_2 by F atoms as a function of the three relevant plasma parameters: neutral F-atom flux, ion flux, and ion energy, by T. Lagarde et al. [67]. As mentioned in section 6.4, SiO_2 can act as intermediate transferring layer between photoresist and Si substrate. So the etching behavior of SiO_2 could be very helpful to improve the surface smoothness of devices fabricated using gray-scale technology. Three saturation effects were reported in this paper. At constant ion current density, the etch rate at first increases linearly with F-atom flux, but then it reaches a plateau, which will increase when the ion current density is increased. Second, at constant F-atom flux, initially the etch rate climbs linearly with ion current density, and again, levels out at larger ion current density, and is higher at larger F-atom flux. Third, the etch rate evolves similarly as a function of bias voltage for constant F-atom flux and ion current density. These results were first interpreted by a simple mechanism of F-atom adsorption on the SiO_2 surface, followed by SiF_4 formation at, and desorption from

the surface, and by assuming a constant density of adsorption sites for fluorine on the SiO_2 surface. The model assumes that, at room temperature, ion induced desorption of O_2 from the SiO_2 surface produces a Si-like over-layer on SiO_2 on which F-atom adsorption is possible. Then, the formation and desorption of SiF_4 can be either spontaneous, or induced by the ion bombardment. When the intensity of the ion bombardment increases, the induced part increases at the expense of the spontaneous part and the etching yield per ion decreases correlatively. This model resulting from the hypothesis was reported to be in complete agreement with the experimental results obtained on the etching kinetics of SiO_2 in SF_6 plasmas.

A chemical flux of sulfur hexafluoride (SF_6) in conjunction with low-energy Ar-ion bombardment was used for chemically assisted ion beam etching (CAIBE) of silicon and silicon dioxide by S. K. Ray et al. [68]. One of the limitations of the conventional reactive ion etching (RIE) process to realize critical etch profiles is the interdependence of plasma parameters and the lack of individual control over the physical and chemical components of etching. The technique of chemically assisted ion beam etching (CAIBE) provides a wide range of direct control of the ion energy, current, and the reactive chemical flux, with reduced radiation damage. The study in this paper showed that CAIBE had a large degree of independent control over the selectivity and anisotropy in dry etching. The total etch rate could be controlled by varying either the Ar-ion milling parameters or the chemical flux of SF_6. The SF_6 gas inlet system was designed to obtain a trade-off between etch rate, uniformity and

surface smoothness. Etch rates were compared with the results of argon ion milling, A higher etch rate enhancement, over pure physical etching, of Si compared to SiO_2 was observed for the same CAIBE conditions. It was shown that the total etch rate could be controlled by varying either the ion beam parameters or the partial pressure of SF_6. The device fabricated showed a reasonable surface smoothness in this paper.

S. L. Lai et al. studied the aspect ratio dependent etching lag reduction in deep silicon etching process [69]. There is a well-documented aspect ratio dependent etching (ARDE) effect in deep silicon etching processes, which means for features with different dimensions etched simultaneously the ARDE effect causes bigger features to be etched at faster rates. This nonlinearity of etching rate could result in a rough, not flat device surface in the device fabrication. This article presented a physical model to describe the time division multiplex (TDM) plasma etch processes and thereafter the experimental results on ARDE lag reduction. The model divided individual plasma etching cycles in the TDM plasma etch processes into polymer deposition, polymer removal, and spontaneous silicon etching stages. With the insights gained from the model and control over the passivation and etch steps, it was demonstrated that ARDE lag can be controlled effectively. Experiments in this paper showed that a normal ARDE lag can be changed to an inverse ARDE lag. Under optimized conditions, the ARDE lag is reduced to below 2%–3% for trenches with widths ranging from 2.5 to 100 μm, while maintaining good etch profile in trenches with different dimensions. Such results are achieved at etch rates exceeding 2

μm/min, with a good surface quality. Experiments were conducted to validate the model on the Unaxis DSE™ III platforms. The plasma etching of silicon is carried out by generating high-density plasma using an ICP source operated at 2 MHz. A RF bias is applied independently to the silicon substrate to control the ion energy during the etch process. The etched substrate is either electro-statically or mechanically clamped to an electrode with helium backside cooling. SF_6 and C_4F_8 were the gases used in the alternating etching/deposition cycles in the deep silicon etching (DSE) processes. By controlling plasma etching parameters, elimination and even the reversing of ARDE lag were accomplished in this article.

B. Bai et al. reported a progress on silicon and silicon oxide etching rate enhancement by adding nitrogen in remote perfluorocarbon plasmas [70]. The addition of 3% nitrogen to a mixture of perfluorocarbon/oxygen/argon in a remote toroidal plasma source was found to double the etching rate of both silicon dioxide and silicon in a downstream process. No further increase of etching rate was observed with greater N_2 addition. It was reported that the phenomena was not caused by plasma discharge changes. Instead, N containing radicals, e.g., N atoms, block the recombination sites in the transfer tube favoring the formation of CO_2 over COF_2 formation on the surface, therefore providing more fluorine atoms to the downstream chamber, as reported. A surface mechanism for these phenomena was confirmed by the long system to the lower etching rate state after N_2 flow has been terminated, approximately 5 orders of magnitude longer than the residence time of

any gas within the system. It was believed that the nitrogen blocks the surface recombination sites for COF_2 formation on the wall of the transfer tube, thereby transporting more fluorine atoms to the downstream process chamber and increasing the etching rate. This paper reported that the doubling of SiO_2 etching rates with N_2 addition to perfluorocarbon (CF_4, C_2F_6, C_3F_8, and C_4F_8), oxygen, and argon mixtures. Fourier transformed infrared spectroscopy (FTIR), mass spectrometer (MS), optical emission spectroscopy (OES), and x-ray photoelectron spectroscopy (XPS) were used to determine the mechanism of the etching rate enhancement in the article.

6.4 Future/further development of our technology and applications

This project successfully demonstrates an improved gray-scale technology and its application to several micro-devices. This new gray-scale technology could provide higher optical density to the mask and higher resolution to the devices, and could lead to lower-cost mass production of higher quality micro- and meso-scale micro-devices in different substrates, e.g. quartz and silicon et al.. So far all processing was done within university facilities and all fabricated devices are not applied to any commercial device or system yet.

In future, efforts should be focused on collaboration with industry partners in order to apply this technology to real applications in commercial devices or systems.

Also the surface quality of devices should draw more attention in future in order to improve the device performance.

In this project, a lot of research effort was put on the last step, which is the dry etching of devices. In this step, the gray-scale patterns in optical resists need to be transferred into substrate via dry etching. When devices with deep structures are fabricated (e.g. devices described in Chapter 4), a large etching ratio (5 to 10 for this project) between the substrate (silicon) and the optical resist will be needed. We found great difficulty on getting an etching ratio larger than 10. In future, if a ratio more than 10 is needed (between silicon and resist); an additional layer (e.g. SiO_2, or SiN_xO_y) should be considered as a medium between the resist and the silicon substrate. By transferring the optical resist into SiO_2 or SiN_xO_y layer first and then do the transferring from SiO_2 or SiN_xO_y layer to Silicon substrate finally, we should be able to get an etching ratio up to 100 very easily. This is because the transferring ratio between silicon and SiO_2 or SiN_xO_y layer can be very big and is much less difficult to control. Previously we mentioned that when optical resist is etched one main challenge is to keep the resist temperature low during the long etching process. We had to pause the etching periodically (e.g. every 5 minutes) to avoid the high temperature of resist. Getting an etching ratio of 1 or less between SiO_2 or SiN_xO_y layer and resist is not difficult. When patterns are transferred into SiO_2 or SiN_xO_y layer, etching them into silicon in a big ratio would be much easier [71, 72, and 73].

This project was funded by the National Science Foundation grant ECS 00-00170. We gratefully acknowledge that Gray Scale Technologies (GST), Inc. made available to us the mask blanks with the new light-attenuation film. Bernard Kress generously helped us design all the computer-generated pattern files for this project and is sincerely appreciated. The e-beam writing was performed at the Cornell NanoScale Science and Technology Facility (CNF), a member of the National Nanotechnology Infrastructure Network supported by the National Science Foundation (Grant ECS 03-35765).

Appendices

Appendix A

March 1, 2004 / Vol. 29, No. 5 / OPTICS LETTERS

Fabrication of an improved gray-scale mask for refractive micro- and meso-optics

Zhou Zhou and Sing H. Lee

Department of Electrical and Computer Engineering, University of California, San Diego, La Jolla, California 92093-0407

Received April 2, 2003

An experiment was performed on a new gray-scale mask material. The mask material is carbon based and has high attenuation in the deep ultraviolet spectral range. The experiment involves making a gray-scale mask for an axicon. Preliminary results show that gray-scale profiles of accurate transmittance functions can be fabricated. Potentially, the capability at deep ultraviolet wavelengths will allow the fabrication of high-resolution components. The high-attenuation characteristic will allow the production of microscale and mesoscale optics of more phase levels. © 2004 Optical Society of America

OCIS codes: 160.4670, 310.6860, 350.3950.

To fabricate micro-optic components of many phase levels with standard binary masking techniques, multiple masks must be used, and multiple alignments, exposures, and processing steps[1,2] must be performed. In fact, this technique needs N masks and N processing steps to achieve 2^N gray levels, so a high production cost results from the need for the multiple lithography and processing steps. Misalignment between masks and the lithography steps also leads to degradation in resolution. Consequently, an alternative process based on gray-scale masks has been developed.[3,4] This gray-scale photolithography process allows the fabrication of an N-level profile by use of only a single mask and a single processing step. Alignment error is thus avoided. High-energy beam-sensitive (HEBS) glass[5,6] was used in earlier experiments for the gray-scale mask fabrication. The principle behind this mask fabrication method is that HEBS glass changes its opacity when exposed to a beam of high-energy electrons or a laser. For example, gray-scale masks may be generated in an electron-beam (e-beam) writer by varying the dosage of electrons striking different areas of a HEBS glass plate. Several other groups have also reported gray-scale lithography with HEBS glass.[7–9] However, a HEBS gray-scale mask cannot provide enough optical density at wavelengths shorter than 350 nm for fabrication of high-resolution components (see Fig. 1).

In this Letter a new light-attenuating film (LAF) is studied for the gray-scale mask. The LAF is a carbon-based material provided by Gray Scale Technology, Inc., (GST) and can potentially reach very high optical density (3 or more) for deep ultraviolet (248- and 193-nm) lithography applications. Higher densities at shorter wavelengths mean potentially higher-resolution components with more phase levels than are achievable with HEBS masks. A comparison of optical density variations between HEBS and our LAF is shown in Fig. 1. It shows that the optical densities of 300-nm-thick LAF are 3.02 and 5.62 at 248 and 193 nm, respectively, whereas the optical density of HEBS glass has a maximum of 3.0 at ~500 nm and decreases to less than 2 at 365 nm.

The fabrication process of this new kind of gray-scale mask is shown in Fig. 2. An e-beam writer (Cambridge Leica EBMF 10.5/CS) with an acceleration voltage of 40 kV was used to write on the ZEP 7000A e-beam resist [Fig. 2(a)]. The thickness of ZEP 7000A was 510 nm. A layer of 20-nm Cr film was applied to the surface of the ZEP 7000A/LAF/quartz structure. The sole purpose of this Cr layer is to avoid the local charging of the mask plate during the e-beam writing process.

After the Cr/ZEP/LAF/quartz plate in the e-beam writer was exposed to patterns of 48 dosage levels, the top Cr layer was removed with the standard chrome etchant solution (wet etch). Then the resist was developed in ZED 750 developer [Fig. 2(b)].

The developed resist pattern was transferred into the LAF by use of a Reactive Ion Beam Etch 250 system from Technics Plasma [Fig. 2(c)]. This ion-milling system was designed to accommodate the introduction of reactive gases to provide chemically assisted ion-beam-etching capability.

To fully use the whole thickness of the 300-nm LAF, the etching ratio between the ZEP 7000A and the LAF was targeted at 510:300 = 1.7:1, since the pattern depth in ZEP 7000A is 510 nm. To achieve this targeted etch ratio, a chamber pressure of approximately 8.2×10^{-5} Torr was used, together with a flow of

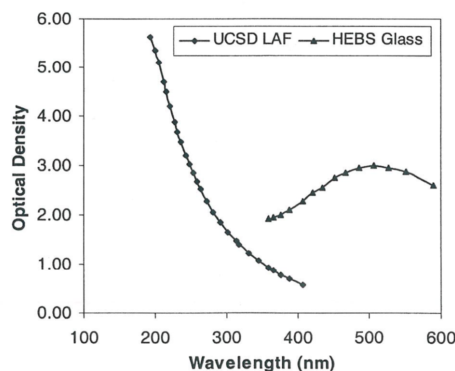

Fig. 1. Comparison of optical density between HEBS glass and a new LAF.

0146-9592/04/050457-02$15.00/0 © 2004 Optical Society of America

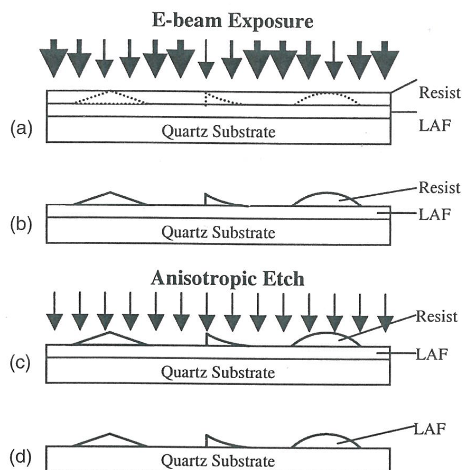

Fig. 2. Fabrication process of gray-scale mask.

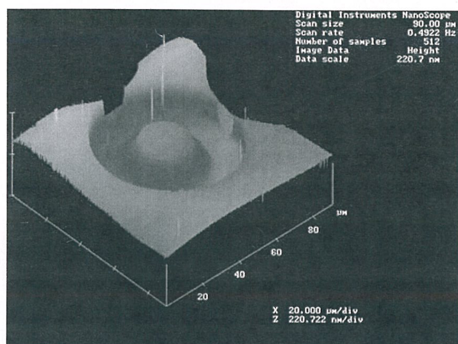

Fig. 3. Axicon in LAF measured by atomic force microscopy.

4.89-SCCM Ar and a flow of 0.2-SCCM O_2 (SCCM denotes cubic centimeters per minute at STP). The other etching parameters include perpendicular ion incidence, an acceleration voltage of 600 V, an ion-beam current of 100 mA, and a sample chuck with rotating capability. To completely etch through the 510-nm ZEP 7000A, an etching time of 25 min was needed. The profile of an axicon in LAF measured by atomic force microscopy is shown in Fig. 3. Figure 4 provides the comparison between the actual transmittance data in our mask and the designed data; transmittance is related to LAF thickness d as $\exp(-\kappa d)$, where κ is the absorption coefficient of LAF. Figure 4 shows that the gray-scale profile of a designed transmittance function can be accurately fabricated.

In summary, a gray-scale mask was fabricated on a new light-attenuating material. The gray-scale mask has the potential of producing higher-resolution micro- and meso-optics of more phase levels or other kinds of microcomponents than HEBS masks. We

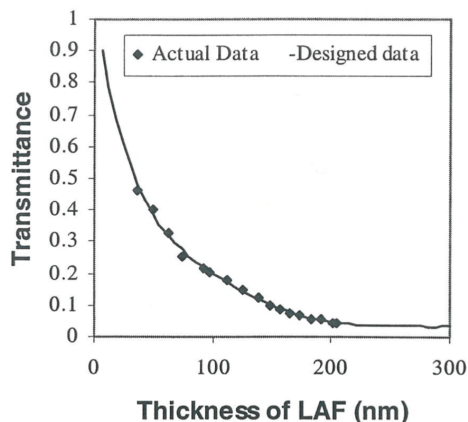

Fig. 4. Transmission comparison between the designed and the fabricated gray-scale steps on the mask. The data were measured at a wavelength of 315 nm, which is the central wavelength of the spectral range of a Karl Suss MJB-UV300 aligner available for this measurement.

will next use this new mask to fabricate optical devices in various substrates.

We gratefully acknowledge that GST made available to us the mask blanks with the new light-attenuating layer.[10] We greatly appreciate the services of e-beam writing provided by the Cornell NanoScale Science & Technology Facility (CNF). We also thank Christian Chovino of GST and David Spencer of CNF for many helpful discussions. Z. Zhou's e-mail address is zhzhou@ucsd.edu.

References

1. G. J. Swanson and W. B. Veldkamp, "High-efficiency, multi-level diffractive optical elements," U.S. patent 4,895,790 (January 23, 1990).
2. G. J. Swanson, "Binary optics technology: theoretical limits on the diffraction efficiency of multi-level diffractive optical elements," Tech. Rep. 914 (MIT, Cambridge, Mass., 1991).
3. W. Daschner, P. Long, R. Stein, C. Wu, and S. H. Lee, Appl. Opt. **36,** 4675 (1997).
4. W. Daschner, P. Long, R. Stein, C. Wu, and S. H. Lee, J. Vac. Sci. Technol. B **14,** 3730 (1996).
5. C. Wu, "Method of making high energy beam sensitive glass," U.S. patent 5,078,771 (January 7, 1992).
6. "Properties of HEBS-Glass," (Canyon Materials, Inc., San Diego, Calif.), retrieved March 10, 2003, http://www.canyonmaterials.com/prop_hebs1.html.
7. M. R. Wang and H. Su, Opt. Lett. **23,** 876 (1998).
8. E. B. Kley, M. Cumme, L. C. Wittig, and C. Wu, Proc. SPIE **3633,** 35 (1999).
9. C. Gimkiewicz, D. Hagedorn, J. Jahns, E. B. Kley, and F. Thoma, Appl. Opt. **38,** 2986 (1999).
10. S. H. Lee, M. S. Jin, and M. L. Scott, "Method for fabricating continuous space variant attenuating lithography mask for fabrication of devices with three-dimensional structures and microelectronics," U.S. patent 6,534,221 (March 18, 2003).

Appendix A, in full, is a reprint of the material as it appears in Optics Letters, Vol. 29 (5), 2004. The dissertation author was the first author of the paper.

Appendix B

Two-beam-current method for e-beam writing gray-scale masks and its application to high-resolution microstructures

Zhou Zhou[1,2,*] and Sing H. Lee[1]

[1]Department of Electrical and Computer Engineering, University of California at San Diego, 9500 Gilman Drive, La Jolla, California 92093-0407, USA

[2]Currently with Triage Wireless Incorporated, 9444 Waples Street, San Diego, California 92121, USA

*Corresponding author: joe@triagewireless.com

Received 10 March 2008; revised 30 April 2008; accepted 1 May 2008; posted 2 May 2008 (Doc. ID 93643); published 4 June 2008

A two-beam-current method is introduced for e-beam writing in the fabrication of gray-scale masks. Compared with the simpler single-current method, the two-beam-current method offers two important advantages: (a) it can achieve a much larger dynamic range for e-beam exposure; (b) the writing time for a gray-scale mask can be reduced when a large pattern is to be written. Here, the new method is first described in detail and its application to the fabrication of our new gray-scale mask is demonstrated. Then, the improved gray-scale masks were employed to fabricate large dynamic range, high-resolution micro-optical elements of less than a couple of micrometers depth, using deep ultraviolet lithography at 248 nm wavelength and an inductively coupled plasma reactive ion etching system. © 2008 Optical Society of America

OCIS codes: 220.2740, 350.4600, 220.4000, 350.3950.

1. Introduction

In all e-beam writings for mask fabrication, only one e-beam current has been used until now. For binary masks (or masks of binary transmittance), there is no reason to use more than one current for the e-beam writing. However, for gray-scale masks (or masks with gray-scale transmittance) the dynamic range of the dosage becomes important, when tens to hundreds of different e-beam doses may be needed. A two-beam-current method (which employs two different e-beam currents in sequence to write the same gray-scale pattern) is developed to achieve a larger dynamic range of e-beam dosage. In this method the computer-generated pattern files for the e-beam writing system divide the whole gray-scale pattern into two portions, one for each of the two currents. The first e-beam of lower current writes the portion of the gray-scale pattern that needs lower e-beam dosage. The second e-beam of higher current writes the portion that needs high dosage. Both portions of the computer-generated pattern files have the same starting (or settling) point for e-beam writing. With a larger dynamic range of e-beam dosage, we can achieve a larger dynamic range in the transmittance of the gray-scale mask. When the two-beam-current method is implemented, we found that it can also offer the advantage of reduced e-beam writing time for large gray-scale masks. In Section 2 the possible gain in dynamic range and reduction in writing time is analyzed. In Section 3 the fabrication of a gray-scale mask using both single- and two-beam-current methods is described and compared. In Section 4, a gray-scale mask is used to fabricate different structures. Discussions on technological issues unique to the two-beam-current method, such as the effects of recalibration of an e-beam system required by the two-current method on writing time reduction and

0003-6935/08/173177-08$15.00/0
© 2008 Optical Society of America

alignment between the two patterns written by the two currents, are provided in Section 5.

2. Two-Beam-Current Method of Writing Gray-Scale Masks

Figure 1 illustrates the comparison of the dosage dynamic range between the two-beam-current and the single-beam-current methods. The increase in the dynamic range is discussed in Subsection 2.A, and the writing time reduction in Subsection 2.B. The general criteria for choosing the two currents in the two-current-method to give larger dynamic range and shorter writing time will be provided in Subsection 2.C. To implement the two-beam-current method, the Leica VB-6HR e-beam system at Cornell, operating at 100 kV, was employed for e-beam writing and a ZEP7000A of 510 nm thick was chosen as the e-beam resist in the experiment. The dotted line in Fig. 1 illustrates the exposure characteristic of ZEP7000A we obtained in the calibration measurement. The developed ZEP7000A pattern is then transferred onto a carbon-based light-attenuating film (LAF) to produce the gray-scale mask [1].

The transmittance of the new gray-scale mask is related to the thickness d of the LAF according to $\exp(-\kappa d)$, where κ is the absorption coefficient of the LAF (which is a constant) [1]. To maximize the optical density range of the mask, the entire thickness of the e-beam resist and the entire thickness d (300 nm) of the LAF should be utilized.

To calculate how much the dynamic range can be increased and the e-beam writing time can be reduced when two beam currents were used, we can make use of the following expression for dosage:

$$D = I/(f * \mathrm{S}), \tag{1}$$

where I is the beam current, f is the clock frequency, and S is the area of pixel grid. Clock frequency is inversely proportional to the dwell time of the e-beam current at each pixel grid. For optimum e-beam writing time, every e-beam system has a finite range of clock frequency to be used. This leads to a finite range of D, when I and S are fixed.

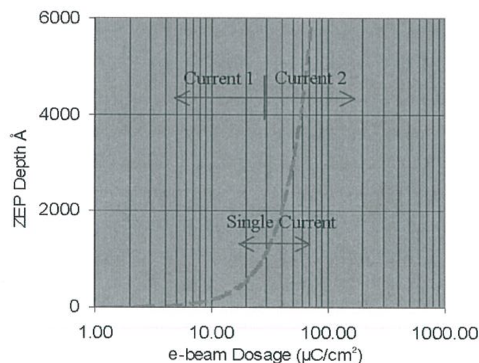

Fig. 1. Exposure characteristic of the ZEP7000A e-beam resist is shown by the dotted curve. Also shown is a comparison of the dosage dynamic range between a single current I_s and two currents I_1 and I_2.

A. Dynamic Range Increase for a Gray-Scale Mask

To illustrate the dynamic range increase by use of the two-current method, let I_s be the single current used, I_1 and I_2 be the two currents used, and ($f_{\max}$ to $f_{\min}$) be the range of clock frequency used. Furthermore, let us assume I_s to be 1.5 nA, and I_1 and I_2 to be 0.5 nA and 25 nA, respectively. We chose S to be 400 nm^2, which corresponds to a pixel size of 20 nm. The minimum pixel size that Leica VB-6HR can achieve is 5 nm, corresponding to $S = 25\,\mathrm{nm}^2$. For the same current and clock frequency, a smaller pixel size would result in a larger dosage D. On Leica VB-6HR $f_{\max}$ is fixed at 25 MHz and $f_{\min}$ is usually 5 MHz for optimized writing speed, although it can be as low as 100 kHz. Then, the dynamic range for D in the single-current method will be ($D_{\max}$ to $D_{\min}$), where

$$D_{\max} = I_s(f_{\min} * S) = 75\,\mu\mathrm{C/cm}^2,$$
$$D_{\min} = I_s(f_{\max} * S) = 75\,\mu\mathrm{C/cm}^2. \tag{2}$$

The dynamic range for D in the two-current method will be ($D'_{\max}$ to $D'_{\min}$), where

$$D'_{\max} = I_2/(f_{\min} * S) = 125\,\mu\mathrm{C/cm}^2,$$
$$D'_{\min} = I_1/(f_{\max} * S) = 5\,\mu\mathrm{C/cm}^2. \tag{3}$$

From Eqs. (2) and (3) we can estimate that the dynamic range is increased from 5 (75:15 μC/cm^2) to 25 (125:5 μC/cm^2). If the single current of 1.5 nA were used to obtain $D'_{\min}$ (5 μC/cm^2), $f_{\max}$ would have to be 50 MHz, which would exceed the capability of the Leica VB6 system. If the single current of 1.5 nA were used to obtain $D'_{\max}$ (125 μC/cm^2), $f_{\min}$ would have to be 3.0 MHz, which is smaller than 5 MHz. A smaller $f_{\min}$ means a longer e-beam writing time.

Because of the different ranges of exposure, we can read from Fig. 1 that the depth range of developed ZEP7000A is from 500 to 5000 Å for the single-current method and that for the two-current method is from 100 to 6000 Å, as shown in Fig. 1. So, the thickness range of the two-current method (5900 Å) is about 31% larger than that of the single-current method (4500 Å). When the thickness profile of ZEP7000A is etched onto the LAF at the same etch ratio, the thickness range of the LAF will also be 31% larger for the two-current method.

B. Writing Time Reduction for a Gray-Scale Mask

The two-beam-current method can also help to reduce the e-beam writing time for gray-scale mask fabrication. To illustrate writing time reduction, let us assume the same dosage range of 15–75 μC/cm^2 is to be covered. The midpoint of this dosage range is 45 μC/cm^2. For the single-current method, 1.5 nA would be used for both the low-dosage range

($15–45\,\mu C/cm^2$) and the high-dosage range ($45–75\,\mu C/cm^2$). For the two-beam-current method, we could use 1.5 nA for the low-dosage range ($15–45\,\mu C/cm^2$) and a higher current (2.5 nA) for the high-dosage range ($45–75\,\mu C/cm^2$). In other words, the difference between the two methods is that we could choose a higher current to write the area of the high-dosage range. Using a higher-beam current to achieve the same dosage range means faster clock frequency and less writing time. This explains why the two-beam-current method can save writing time, compared with the single-current method.

To estimate how much time can be saved by the use of the two-beam-current method, we make use of Eq. (1) again:

$$f = I/(D * S), \quad (4)$$

where S is $400\,nm^2$. Moreover, if we take A as the total area of the pattern to be written, the total e-beam writing time T can be expressed as

$$T = A/(S * f), \quad (5)$$

where f is the average clock frequency for the e-beam writing. In comparing the writing times between the single-current and the two-beam-current methods, A and S will be the same and can be taken as constants. To calculate the total writing times T we need only to calculate the f_s for the single-current method and f_1 and f_2 for the two-current method:

For the single-current method, the average dosage is $D_s = 45\,\mu C/cm^2$ (for the $15–45\,\mu C/cm^2$ range). Using Eq. (4), we calculate its corresponding frequency to be $f_s = 8.33\,MHz$. For the two-current method, the average dosages are $D_1 = 30\,\mu C/cm^2$ (for the $15–45\,\mu C/cm^2$ range) and $D_2 = 60\,\mu C/cm^2$ (for the $45–75\,\mu C/cm^2$ range). Using Eq. (4), we calculate $f_1 = 12.5\,MHz$ and $f_2 = 10.41\,MHz$.

Assuming that the pattern area in the $15–45\,\mu C/cm^2$ range is the same size as that in the $45–75\,\mu C/cm^2$ range, the total writing times T_s for the single-current method and T' for the two-current method can be calculated to be:

$$T_s = A/S * f_s = 1.2 \times 10^{-7}(A/S), \quad (6)$$

$$T' = 0.5A/(S * f_1) + 0.5A/(S * f_2) = 0.88 \times 10^{-7}(A/S). \quad (7)$$

Therefore, the writing time saving will be $(1.2 - 0.88)/1.2 = 26.7\%$, which is significant.

Another way to estimate the actual e-beam writing time is to use the online Parameter Calculator for Leica VB-6HR provided by IBM [2]. To write a pattern area of $2.25\,mm^2$, the Parameter Calculator gives 11.19 min for the single-current method and 8.27 min for the two-current method, resulting in about 3 min (or 26.1%) of time saving in writing. For a larger pattern area of $10\,mm^2$ the Parameter Calculator shows the same percentage (26.1%) of time saving in writing. Figure 2 shows the time saving as calculated by the online Parameter Calculator for a range of writing areas, assuming the same writing parameters chosen above. If I_2 were larger in the above calculations, for example, 4.5 nA, then the time saving could be larger than what we can obtain from 2.5 nA. This is because, for the same dosage and the same pattern size, larger current leads to higher clock frequency and shorter writing time. (More discussions on maximizing writing time, including that for writing an even larger area, is given in Subsection 5.A.)

C. Criteria for Choosing the Two Currents

Hence, the general criteria for choosing the two currents in the two-current method are: (a) I_2 should be chosen to reach the maximum required dosage, determined by what it takes to clear the e-beam resist (e.g., ZEP7000A for our experiment); (b) I_1 should be chosen so that its maximum reachable dosage (when the slowest clock frequency of the e-beam system is used) is the same as the minimum reachable dosage by I_2 (when the fastest clock frequency of 25 MHz is used). There should be no dosage gap between the maximum dosage reachable by I_1 and the minimum dosage reachable by I_2. When the above two conditions are met, then I_1 should be as small as possible so that the exposure dynamic range can be maximized; at the same time I_2 should be as big as possible so that the writing time saving can be maximized.

3. Gray-Scale Mask Fabrication

Gray-scale masks fabricated by the two-beam-current method are described below and compared with those by a single-beam-current method.

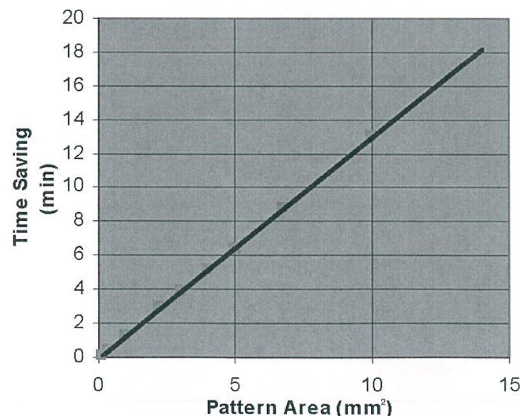

Fig. 2. Time saving with the two-beam-current method calculated from the online Parameter Calculator (provided by IBM [2]) for the Leica VB-6HR e-beam system. The slope of the line is approximately $1.3\,min/mm^2$.

A. E-Beam Resist and Its Preparation

The e-beam resist we used was ZEP7000A. The resist was applied by a resist spinner to a LAF-coated quartz substrate. The LAF film on quartz is 300 nm thick. The spinning parameters are 300 rpm for 3 s, followed by 550 rpm for 177 s. After being allowed to relax for 5 min, the resist was baked in a convection oven at 180 °C for 30 min. This results in a resist layer of 550 nm thick. This ZEP7000A coating process was recommended by the resist manufacturer and was performed at Telic Company.

Next, the resist surface was coated by a sputtering machine with a 10 nm Cr film. The role of this Cr layer is to avoid the local charging of the mask plate during the e-beam writing process. The Cr/ZEP7000A/LAF/quartz sample is now ready for e-beam writing. The Cr coating was carried out at Nanofilm Incorporated.

ZEP7000A is a positive resist frequently used in the semiconductor industry. Longer exposure on the resist will cause more of it to be washed off when it is developed. Thinner resist will contribute to more of the underlying light-attenuating material being etched away, resulting in higher transmission when the e-beam resist profile is transferred to the LAF by dry etching.

It should be pointed out here that the dosage to clear a certain thickness of e-beam resist varies for different e-beam systems. For example, to clear the entire ZEP7000A resist thickness, a higher dosage is required (approximately $62\,\mu C/cm^2$) for the Leica VB-6HR system (operating at 100 kV), whereas to clear the same resist thickness it requires only about $20\,\mu C/cm^2$ for the Leica EBMF 10.5/CS system (operating at 40 kV). This is because a higher accelerating voltage means a higher electron energy and a higher possibility of punching through without exposing the e-beam resist. In other words, the electrons have less chance of exposing the e-beam resist at higher energy.

B. E-Beam Writing Process and ZEP7000A Resist Development

We used 0.475 and 2.05 nA for the two-current experiment and 1.5 nA for the single-beam-current experiment in pattern writing. Other parameters of the Leica VB-6HR system, such as the calibration pattern and device patterns were all kept the same to obtain a fair comparison of the e-beam writing times of the two approaches.

The beam size of the system was 5 nm. The pixel grid size of our patterns was chosen to be 20 nm. A beam size of 25 nm was used; it was chosen to be a little larger than the pixel grid size to obtain smoother pattern surfaces. A calibration pattern of 64 steps was designed and written on the same mask that contains other device patterns.

The ZEP7000A resist was developed in a ZED 750 developer for 2 min at room temperature (23 °C); then the sample was rinsed in ZED-D for 10 s. The development method was immersion with mild agitation. After the development step, an atomic force microscope (AFM) was used to measure the calibration steps. About 40 nm (or 7.3% of the original 550 nm thickness) of the ZEP7000A was lost during the development process. This is normal because 5–10% of the predevelopment thickness is usually lost during the resist development process. To simplify the comparison between the resist profiles written by the two-current and the single-current methods, the same resist development parameters were used on the two masks.

C. Dry-Etching for a Gray-Scale Mask

To fully use the entire 300 nm thickness of the light-attenuating film, the etching ratio between the ZEP7000A and the light-attenuating film was targeted at 510:300 = 1.7:1, since the pattern depth in the developed ZEP7000A is 510 nm. To achieve this targeted etch ratio, a Trion inductively coupled plasma reactive ion etching (ICP–RIE) system was used with etching parameters of 10 mTorr etching pressure, 50/5 sccm (sccm denotes cubic centimeters per minute at STP) CF_4/O_2, 50 W inductively coupled plasma (ICP) power, 50 W reactive ion etching (RIE) power, and 20 °C chiller temperature. To completely etch through the 510 nm ZEP7000A, an etching time of 22 min was needed.

D. Experimental Results

To verify e-beam writing time reduction for the two-current method, we simulate the writing of a collection of small patterns on a Leica VB-6HR (including calibration steps, the axicon and the retro-reflector) and repeat them five times, totaling $0.4\,mm^2$ in area. The parameters used in the writing simulation are exactly the same as those used in the calculations provided in Subsection 2.B.

We find that 125 s are required for the single-current method, whereas it takes only 96 s for the two-current method. The time saving is therefore 29 s or 23.2%, which is very close to the predictions (26.7% versus 26.1% in the theoretical calculation shown in Fig. 2). When the collection of small patterns was repeated 10 times totaling an area of $0.8\,mm^2$, the writing times become 249 s for the single-current method and 190 s for the two-current method. This results in 59 s (or 23.7%) of time saving, which is also in close agreement with predictions.

Figure 3 shows that the full range (510 nm thick, 64 calibration steps) of the e-beam resist is etched when two beam currents are used to write the resist. It also shows that the range of resist depth is smaller (~400 nm, 64 calibration steps) when we use a single-beam current to write while maintaining the same parameters to develop the resist. This is consistent with the results illustrated in Fig. 1.

After transferring the developed resist profiles onto the LAF by dry etching, the optical densities of the calibration steps at a 248 nm wavelength could be obtained from the thickness data and the absorption coefficient of the LAF. Figure 4 provides the data, which shows that the gray-scale mask written

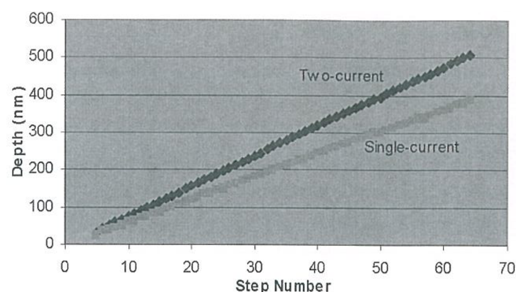

Fig. 3. Measured depth profiles of the calibration steps in the e-beam resist. The depths at step #64 are about 510 and 400 nm for the two-current and single-current methods, respectively.

by the two-current method can achieve an optical density range as high as 3.02, whereas the mask written by the single-current method can provide a range of only 2.30.

4. Fabricating Micro-Optical Devices

Using the new gray-scale mask, the following procedures are followed to fabricate devices of shallow (approximately a couple of micrometers in depth) microstructures. First, transmittance patterns in the gray-scale mask are transferred to an optical resist using an optical stepper. Second, the gray-scale profiles in the developed optical resist are then transferred onto the substrate to obtain the devices by dry etching in an ICP–RIE system. Only a single iteration of optical lithography and dry etching is required in gray-scale technology, as compared to multiple iterations required by binary technology to produce microstructures with gray scales in devices.

Since our mask can work in deep ultraviolet (DUV) lithography, a 248 nm stepper and an optical resist sensitive to 248 nm were employed in the optical lithography process. Hence, higher resolution can be achieved in the device microstructures when compared with the use of a 365 nm or longer wavelength lithography. The wavelength of 248 nm is out of the reach of any gray-scale mask on high energy beam-sensitive glass because its optical density becomes quite low at wavelengths below 300 nm [3]. Figure 5 summarily shows the fabrication procedures of devices with gray scale by the use of our improved gray-scale technology.

A. Optical Lithography Process

A Nikon stepper operated at 248 nm with a 4:1 demagnification factor was employed in this experiment. It is located at Penn State University. A Shipley UV5 and a MicroChem PMGI-SF11 were used as the optical resists. UV5 is a popular, thin resist for 248 nm binary lithography and was used to fabricate the binary gratings to demonstrate the high-resolution capability of our gray-scale mask. A PMGI-SF11 resist is a thick, good analog resist for gray-scale lithography in the DUV range and was used to fabricate an off-axis Fresnel lens and other gray-scale patterns in this experiment. Generally, analog resists have lower contrast than binary resists in their characteristics.

UV5 has a typical thickness of 300 nm. The preparation, exposure, and developing parameters of UV5 are provided in Table 1.

The typical thickness of PMGI-SF11 is 1–2 μm. The preparation, exposure, and developing parameters of the PMGI-SF11 resist are provided in Table 2. Figure 6 shows the typical exposure characteristics of PMGI-SF11 at 248 nm.

B. Dry-Etching for Fabricating Optical Devices

A Trion MINILOCK II ICP–RIE etcher was used to transfer the gray-scale profiles in the developed optical resists onto the substrate. Quartz was adopted as the substrate for the fabrication of a Fresnel lens. ICP–RIE can operate with higher plasma density at lower pressure, compared with a conventional parallel-plate RIE system. It is a cleaner system and can perform a more uniform etch over a larger area. The parameters employed for etching PMGI-SF11 to quartz are provided in Table 3. The dry-etching parameters in Table 3 result in etching rates of 45 nm/ min for PMGI and 21 nm/ min for quartz,

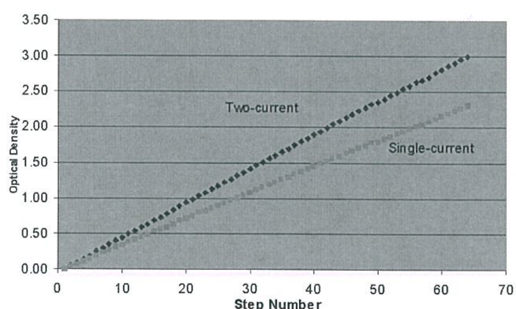

Fig. 4. Optical densities of the calibration steps at 248 nm. The maximum optical densities (at step #64) achieved in two-current and single-current methods are 3.02 and 2.30, respectively.

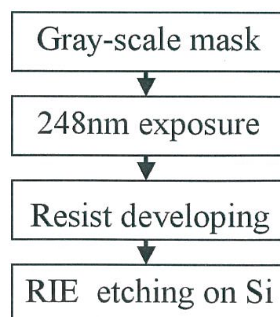

Fig. 5. Fabrication processes of high-resolution microdevices using our improved gray-scale masks.

Table 1. Processing Parameters of a UV5 Resist

Resist spinning	5000 rpm, 45 s
Resist baking	130°C, 1 min, hotplate
Exposure	10 mJ/cm^2
Developing	LDD26W, 45 s
Hard baking	145°C, 3 min, hotplate

with an etch ratio of approximately 2.1:1. To avoid overheating the resist, the etching process was paused for 5 min after every 5 min of etching. To get more uniform etching, the substrate was manually rotated 90° after every 10 min of etching.

C. Experimental Results

Using the new gray-scale mask and a 248 nm stepper, a resolution of 0.2 μm was achieved in a UV5 resist as shown in Fig. 7. Binary gratings with different periodicities were the patterns used for testing the resolution limit. Here, no resolution enhancement method (e.g., phase contrast method) was used in our pattern design.

Figure 8 is the atomic force microscopy (AFM) picture of an off-axis Fresnel lens on quartz. Because of the limitation of the AFM scanning lateral range (~75 μm), only a portion of the Fresnel lens was captured. The periodicities in the shown region of the Fresnel lens are between 10 and 12 μm.

Figure 9 is an AFM picture of a map with interesting 3-D topography in the Alsace region of France, fabricated on our gray-scale mask. The area of the map is about 20 μm × 70 μm, close to the size of a human hair cross-sectional area.

5. Discussions

A. Effect of Required E-Beam System Recalibration on Writing Time Reduction

When two currents are used in e-beam writing by a Leica VB-6HR, an important fact to take into account is that a certain amount of time (5–10 min usually depending on the operator) will be needed to call the second pattern file, recalibrate the e-beam system for the second e-beam current, and to reposition the stage holding the sample. From Fig. 2 we can see that, when the pattern area to be written is small, this extra time could be more than the writing time saving. Therefore, only when writing a larger pattern area (e.g., >10 mm^2 with the same parameters

Table 2. Processing Parameters of a PMGI-SF11 Resist

Resist spinning	2000 rpm, 45 s
Resist baking	115°C, 120 s, hotplate
Exposure	10 mJ/cm^2, 248 nm
Developing	MF 321, 180 s, immersion, mild agitation
Rinse	DI water, 30 s
Dry	Nitrogen gas

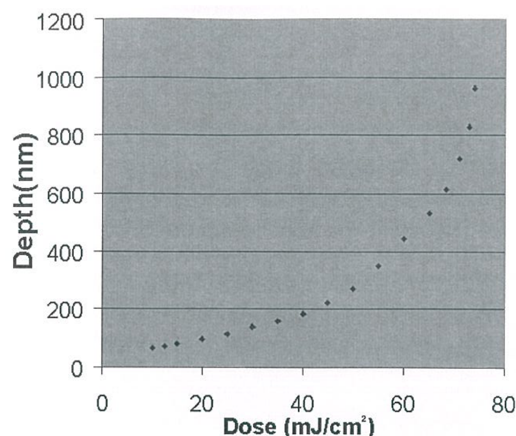

Fig. 6. Exposure characteristic of the PMGI-SF11 resist.

adopted for Fig. 2) can time saving be expected for the two-beam-current method.

For the 6 in. (15 cm) mask used in the integrated circuit industry today, we can estimate the writing time saving as follows, when the two-beam-current method is used. Conservatively, let us also assume that only 1% of the total mask area needs to be written by the two-beam-current method. Then, the total writing area becomes about 225 mm^2. From Fig. 2 we can estimate the time saving would be about 290 min (or 4 h 50 min), which is much larger than the extra time for recall, recalibration, and reposition. Therefore, the larger the mask writing area, the more time can be saved by using the two-beam-current method to reduce the mask fabrication costs.

B. Alignment and Stitching Issues when Using the Two-Beam-Current Method

The two-beam-current method requires the computer-generated pattern data file for e-beam writing to be partitioned into two, based on the dynamic range requirements, one for each of the two currents. Both portions of the pattern file use the same starting point. The alignment accuracy of the second pattern written by the second current with respect to the first depends on the realignment of the stage holding the sample while the current is changed and recalibrated. This mechanical realignment will usually cause some stitching error between the two patterns, typically approximately 40 nm for the Leica VB6 system. Experimentally, we did observe this small stitching error in the e-beam resist

Table 3. Parameters for Etching PMGI into Quartz

Pressure	10 mTorr
ICP/RIE power	40/120 W
CF_4/Ar	20/20 sccm
Temperature	5°C

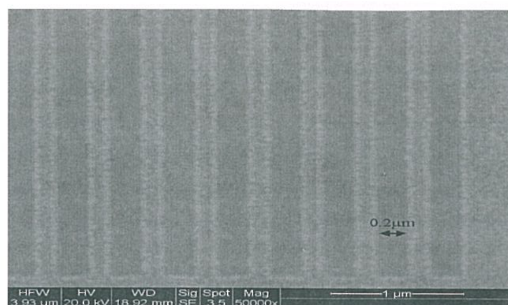

Fig. 7. SEM picture showing a resolution of $0.2\,\mu$m in UV5 by 248 nm lithography.

pattern and its transfer to the mask in the dry-etching process, as shown by the stitch line on the mask in Fig. 10(a). The ellipse on the top portion of the elliptical axicon mask has dimensions of $21.20\,\mu$m (minor axis) by $25.44\,\mu$m (major axis), and the bottom ellipse is $40\,\mu$m by $48\,\mu$m.

However, in the optical lithography process, the stepper employed has a wavelength of 248 nm and a demagnification factor of 4. When the stitching error is <40 nm, this stitching error is reduced significantly to a level not observable in the optical resist, as shown in Fig. 10(b). Figure 10(b) shows a microscopic picture of an axicon on PMGI, enlarged 4 times to the same size as that of the mask for a better comparison with Fig. 10(a). This small stitching error on the optical resist should not cause much surface smoothness problem in device fabrication of micrometer dimensions.

C. Extension to Three-Beam-Current Method

The approach behind the two-current method, as discussed here, can be extended to three or more currents, when larger dynamic ranges for fabricating devices of deeper microstructures or more e-beam writing time reduction for larger pattern areas are needed. Currently, an optical density of 3 (achievable by the two-beam-current method) may have been sufficient for many applications; there appears to be no great need to explore for higher optical density. In the future when the need arises, the extension to three or more beam currents can be explored. The carbon-based light modulating material we employed can be used for the gray-scale mask in 193 nm lithography [1], which is a shorter wavelength than the 248 nm used here. Shorter wavelengths generally allow for higher resolution devices to be fabricated.

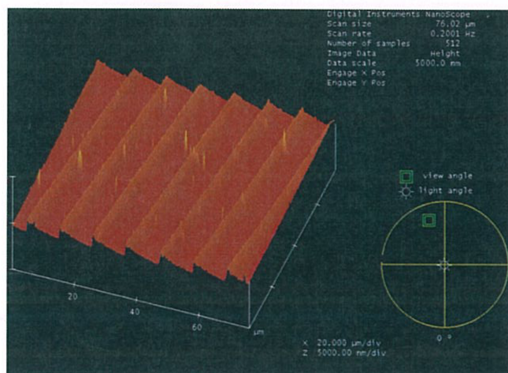

Fig. 8. (Color online) AFM picture of a portion of an off-axis Fresnel lens on quartz

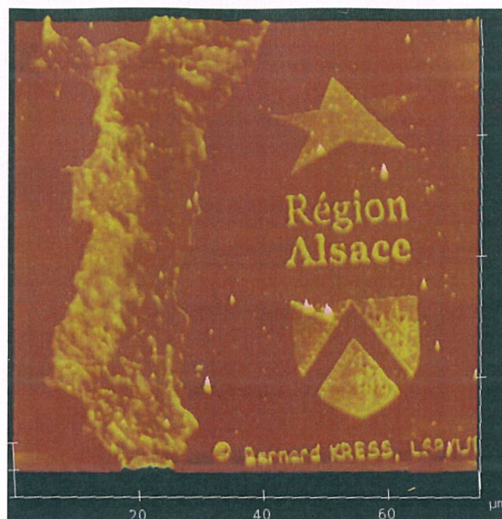

Fig. 9. (Color online) AFM picture of a 3-D topographic map on LAF.

6. Conclusion

The two-beam-current method has been demonstrated for e-beam writing in the fabrication of our new gray-scale mask. This method gives a larger e-beam exposure dynamic range than the one-beam-current method. It also saves much e-beam writing time, lowering the costs of gray-scale masks to an affordable level when the writing area is large.

Since our gray-scale mask is on a carbon-based light modulating material, it can work in the DUV and UV wavelength ranges for device production, instead of being restricted to i-line or longer wavelengths. Higher resolution components and devices can be made when shorter wavelength optical lithography can be applied.

Gray-scale technology will help to lower the production costs for devices with multiple depth levels in many fields of application, since it requires only one optical lithography and dry-etching iteration, while binary technology requires multiple iterations. However, more careful monitoring is required in mask fabrication, optical lithography, and dry-etching processes to preserve the gray scale, when

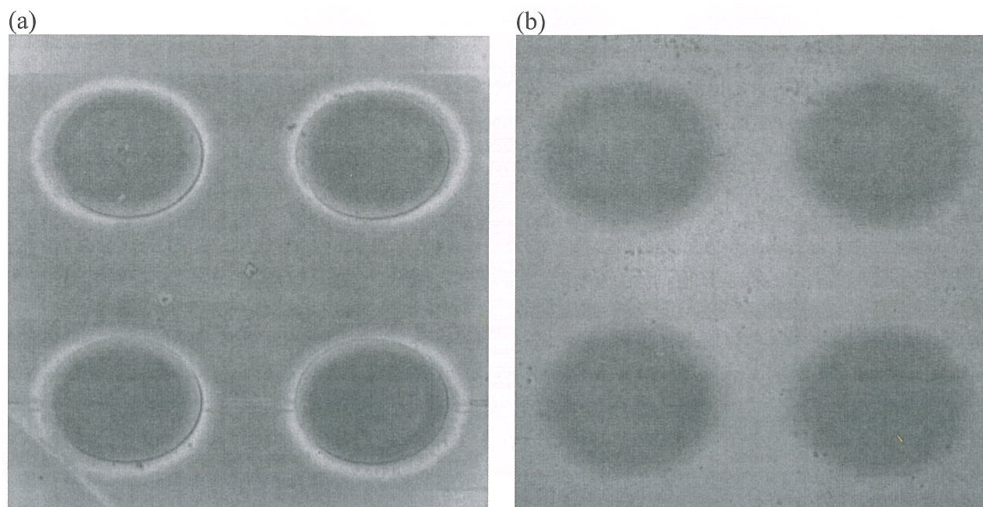

Fig. 10. (a) Microscopic pictures of axicons on the gray-scale mask; (b) the microscopic pattern on PMGI resist (enlarged four times to show the disappearance of the curved line due to stitching error).

gray-scale technology is applied. This will be summarily discussed in another paper, where the applications of our gray-scale mask to fabricate devices with deeper microstructures (greater than a couple micrometers) will be reported.

This project was funded by the National Science Foundation grant ECS 00-00170. We gratefully acknowledge Gray Scale Technologies (GST), Inc. for making the mask blanks with the new light-attenuation film [4] available to us. The e-beam writing was performed at the Cornell NanoScale Science and Technology Facility (CNF), a member of the National Nanotechnology Infrastructure Network, supported by the National Science Foundation (grant ECS 03-35765). Great appreciation is given to Bernard Kress for helping us to design the pattern files for our e-beam writing. We also greatly appreciate Alan Bleier at Cornell University for his valuable help with various aspects of our experiments.

References

1. Z. Zhou and S. H. Lee, "Fabrication of an improved gray-scale mask for refractive micro- and meso-optics," Opt. Lett. **29**, 457–458 (2004).
2. Leica VB Parameter Calculator, http://www.research.ibm.com/people/r/rooks/calc.html
3. C. Wu, "Method of making high energy beam sensitive glasses," U.S. patent 5,078,771 (7 January 1992).
4. S. H. Lee, M. S. Jin, and M. L. Scott, "Method for fabricating continuous space variant attenuating lithography mask for fabrication of devices with three-dimensional structures and microelectronics," U.S. patent 6,534,221 (18 March 2003).

Appendix B, in full, is a reprint of the material as it appears in Applied Optics, Vol. 47 (19), 2008. The dissertation author was the first author of the paper.

Appendix C

C1 – An e-beam job file example

```
;       FILENAME: 4thNSF.JOB
;           DATE: 7/2/2004
;    DESCRIPTION: Axicon & SEMISPHERE
;       MATERIAL: ZEP7000A(11/00)
; E-BEAM SETTINGS: 0.75nA, 40Kev
;   Beam Diameter: 50nm
;   PIXEL SPACING: 50nm
;
; START JOB FILE: 4thNSF.JOB
KEY 1
; open log file
LOF
LOG UCSD2001
LON
; JOB FROM UCSD 4thNSF.JOB STARTS AT:
TIM
LOF
;      Start job file,
;      Initialization:
;        voltage: 40KV
;     field size: 1.6384mm
;    beam current: 0.75nA
; @START1P6
;
LON
FLD 1.6384
;
MOV FC
SBC 0.75E-9 FC
LOF
;      Calibration
@CALIB
;      Height mapping 3 inches square
@HTS3SQR
;
; define A3 at Cell 1
;
SPO A3 -20 -20
```

```
MOV A3
; map relative to A3
RMP REL P9 A3
;
LOA CALIACK16.JOB
LOA CALIHCK8.JOB
LOA AXIACKA.JOB
LOA AXIACKB.JOB
LOA AXIACKC.JOB
LOA SEMIBCKA.JOB
LOA SEMIBCKB.JOB
LOA SEMIBCKC.JOB
LOA AXICCKA.JOB
LOA AXICCKB.JOB
LOA AXICCKC.JOB
LOA AXIDCKC.JOB
LOA SEMIECKA.JOB
LOA SEMIECKB.JOB
LOA SEMIECKC.JOB
LOA SEMIFCKC.JOB
;
; ==============================================
; AAA
; ==============================================
LON
; Begin time for PATTERN A
TIM
LOF
;
; CELLS 1-4
MEX 0 0
&AXIACKA.JOB
%AXIA0.BPD
&AXIACKB.JOB
%AXIA10.BPD
&AXIACKC.JOB
%AXIA20.BPD
MEX 34.6 0
&AXIACKA.JOB
%AXIA0.BPD
&AXIACKB.JOB
%AXIA10.BPD
&AXIACKC.JOB
```

```
%AXIA20.BPD
MEX 34.6 34.6
&AXIACKA.JOB
%AXIA0.BPD
&AXIACKB.JOB
%AXIA10.BPD
&AXIACKC.JOB
%AXIA20.BPD
MEX 0 34.6
&AXIACKA.JOB
%AXIA0.BPD
&AXIACKB.JOB
%AXIA10.BPD
&AXIACKC.JOB
%AXIA20.BPD
;
LON
; Ending time for PATTERN A
TIM
LOF
; ============================================
; BBB
; ============================================
LON
; Begin time for PATTERN B
TIM
LOF
;
; CELLS 1-4
MEX 0.62 0
&SEMIBCKA.JOB
%SEMIB0.BPD
&SEMIBCKB.JOB
%SEMIB10.BPD
&SEMIBCKC.JOB
%SEMIB20.BPD
MEX 35.22 0
&SEMIBCKA.JOB
%SEMIB0.BPD
&SEMIBCKB.JOB
%SEMIB10.BPD
&SEMIBCKC.JOB
%SEMIB20.BPD
```

```
MEX 35.22 34.6
&SEMIBCKA.JOB
%SEMIB0.BPD
&SEMIBCKB.JOB
%SEMIB10.BPD
&SEMIBCKC.JOB
%SEMIB20.BPD
MEX 0.62 34.6
&SEMIBCKA.JOB
%SEMIB0.BPD
&SEMIBCKB.JOB
%SEMIB10.BPD
&SEMIBCKC.JOB
%SEMIB20.BPD
;
LON
; Ending time for PATTERN B
TIM
LOF
; ============================================
; CCC
; ============================================
LON
; Begin time for PATTERN C
TIM
LOF
;
; CELLS 1-4
MEX 1.2 0
&AXICCKA.JOB
%AXICD0.BPD
&AXICCKB.JOB
%AXICD10.BPD
&AXICCKC.JOB
%AXICD20.BPD
MEX 35.8 0
&AXICCKA.JOB
%AXICD0.BPD
&AXICCKB.JOB
%AXICD10.BPD
&AXICCKC.JOB
%AXICD20.BPD
MEX 35.8 34.6
```

```
&AXICCKA.JOB
%AXICD0.BPD
&AXICCKB.JOB
%AXICD10.BPD
&AXICCKC.JOB
%AXICD20.BPD
MEX 1.2 34.6
&AXICCKA.JOB
%AXICD0.BPD
&AXICCKB.JOB
%AXICD10.BPD
&AXICCKC.JOB
%AXICD20.BPD
;
LON
; Ending time for PATTERN C
TIM
LOF
; ==============================================
; DDD
; ==============================================
LON
; Begin time for PATTERN D
TIM
LOF
;
; CELLS 1-4
MEX 1.2 0.26
&AXICCKA.JOB
%AXICD0.BPD
&AXICCKB.JOB
%AXICD10.BPD
&AXIDCKC.JOB
%AXICD20.BPD
MEX 35.8 0.26
&AXICCKA.JOB
%AXICD0.BPD
&AXICCKB.JOB
%AXICD10.BPD
&AXIDCKC.JOB
%AXICD20.BPD
MEX 35.8 34.86
&AXICCKA.JOB
```

```
%AXICD0.BPD
&AXICCKB.JOB
%AXICD10.BPD
&AXIDCKC.JOB
%AXICD20.BPD
MEX 1.2 34.86
&AXICCKA.JOB
%AXICD0.BPD
&AXICCKB.JOB
%AXICD10.BPD
&AXIDCKC.JOB
%AXICD20.BPD
;
LON
; Ending time for PATTERN D
TIM
LOF
; ==============================================
; EEE
; ==============================================
LON
; Begin time for PATTERN E
TIM
LOF
;
; CELLS 1-4
MEX 1.8 0
&SEMIECKA.JOB
%SEMIE0.BPD
&SEMIECKB.JOB
%SEMIE10.BPD
&SEMIECKC.JOB
%SEMIE20.BPD
MEX 36.4 0
&SEMIECKA.JOB
%SEMIE0.BPD
&SEMIECKB.JOB
%SEMIE10.BPD
&SEMIECKC.JOB
%SEMIE20.BPD
MEX 36.4 34.6
&SEMIECKA.JOB
%SEMIE0.BPD
```

```
&SEMIECKB.JOB
%SEMIE10.BPD
&SEMIECKC.JOB
%SEMIE20.BPD
MEX 1.8 34.6
&SEMIECKA.JOB
%SEMIE0.BPD
&SEMIECKB.JOB
%SEMIE10.BPD
&SEMIECKC.JOB
%SEMIE20.BPD
;
LON
; Ending time for PATTERN E
TIM
LOF
; ================================================
; FFF
; ================================================
LON
; Begin time for PATTERN F
TIM
LOF
;
; CELLS 1-4
MEX 1.8 0.23
&SEMIECKA.JOB
%SEMIF0.BPD
&SEMIECKB.JOB
%SEMIF10.BPD
&SEMIFCKC.JOB
%SEMIF20.BPD
MEX 36.4 0.23
&SEMIECKA.JOB
%SEMIF0.BPD
&SEMIECKB.JOB
%SEMIF10.BPD
&SEMIFCKC.JOB
%SEMIF20.BPD
MEX 36.4 34.83
&SEMIECKA.JOB
%SEMIF0.BPD
&SEMIECKB.JOB
```

```
%SEMIF10.BPD
&SEMIFCKC.JOB
%SEMIF20.BPD
MEX 1.8 34.83
&SEMIECKA.JOB
%SEMIF0.BPD
&SEMIECKB.JOB
%SEMIF10.BPD
&SEMIFCKC.JOB
%SEMIF20.BPD
;
LON
; Ending time for PATTERN F
TIM
LOF
;==============================================
; Calibration Patterns
;==============================================
LON
; Begin time for Calibration Patterns
TIM
LOF
;
; Calibration Pattern for A
CELLS 1-4
MEX 0 0.62
EXI 34.6 34.6
EXN 2 2
&CALIACK16.JOB
%CALI16.BPD
;
; Calibration Pattern for C
CELLS 1-4
MEX 0 1.62
EXI 34.6 34.6
EXN 2 2
&AXICCKA.JOB
%CALI16.BPD
;
CELLS 1-4
MEX 0 2.62
EXI 34.6 34.6
EXN 2 2
```

```
&AXICCKB.JOB
%CALI16.BPD
;
CELLS 1-4
MEX 0 3.62
EXI 34.6 34.6
EXN 2 2
&AXICCKC.JOB
%CALI16.BPD
;
; Calibration Pattern H
;
CELLS 1-4
MEX 0 5.3
EXI 34.6 34.6
EXN 2 2
&CALIHCK8.JOB
%CALI8.BPD
;
;
LON
; Ending time for Calibration Patterns
TIM
LOF
;
;
;============================================================
=====
; G1-G10: Binary Grating (Period varies from 0.1 to 1 micron)
; G11: Cylinder Blazes (8 phase levels, 0.15 to 0.4 micron/phase)
;============================================================
=====
LON
; Begin time for G1-G11 Patterns
TIM
LOF
;G1-G10
;
CELLS 1-4
MEX 0 4.62
CLK 1 1E6
CLK 2 1E6
EXI 34.6 34.6
```

```
EXN 2 2
%BINARY01.BPD
;
CELLS 1-4
MEX 0.11 4.62
CLK 1 1E6
CLK 2 1E6
EXI 34.6 34.6
EXN 2 2
%BINARY02.BPD
;
CELLS 1-4
MEX 0.22 4.62
CLK 1 1E6
CLK 2 1E6
EXI 34.6 34.6
EXN 2 2
%BINARY03.BPD
;
CELLS 1-4
MEX 0.33 4.62
CLK 1 1E6
CLK 2 1E6
EXI 34.6 34.6
EXN 2 2
%BINARY04.BPD
;
CELLS 1-4
MEX 0.44 4.62
CLK 1 1E6
CLK 2 1E6
EXI 34.6 34.6
EXN 2 2
%BINARY05.BPD
;
CELLS 1-4
MEX 0.55 4.62
CLK 1 1E6
CLK 2 1E6
EXI 34.6 34.6
EXN 2 2
%BINARY06.BPD
;
```

```
CELLS 1-4
MEX 0.66 4.62
CLK 1 1E6
CLK 2 1E6
EXI 34.6 34.6
EXN 2 2
%BINARY07.BPD
;
CELLS 1-4
MEX 0.77 4.62
CLK 1 1E6
CLK 2 1E6
EXI 34.6 34.6
EXN 2 2
%BINARY08.BPD
;
CELLS 1-4
MEX 0.88 4.62
CLK 1 1E6
CLK 2 1E6
EXI 34.6 34.6
EXN 2 2
%BINARY09.BPD
;
CELLS 1-4
MEX 0.99 4.62
CLK 1 1E6
CLK 2 1E6
EXI 34.6 34.6
EXN 2 2
%BINARY10.BPD
;
;
; G11
CELLS 1-4
MEX 1.1 4.62
EXI 34.6 34.6
EXN 2 2
&CALIHCK8.JOB
%BLAZE.BPD
;
;
LON
```

```
; Ending time for G1-G11 Patterns
TIM
LOF
; ============================================
; END OF EXPOSURE
; ============================================
; CLEAN UP
;
DLT CALIACK16.JOB
DLT CALIHCK8.JOB
DLT AXIACKA.JOB
DLT AXIACKB.JOB
DLT AXIACKC.JOB
DLT SEMIBCKA.JOB
DLT SEMIBCKB.JOB
DLT SEMIBCKC.JOB
DLT AXICCKA.JOB
DLT AXICCKB.JOB
DLT AXICCKC.JOB
DLT AXIDCKC.JOB
DLT SEMIECKA.JOB
DLT SEMIECKB.JOB
DLT SEMIECKC.JOB
DLT SEMIFCKC.JOB
;
;
LON
; *******************************************
;       4THNSF.JOB STOPS AT:
TIM
; *******************************************
LOF
;
; === END OF THIS JOB FILE ===
!DONE
@CC
```

C2- Clock files used in C1 job file

```
; Clock file: AXIACKA
; for ZEP7000A resist(11/00)
; 16 levels
; Generated by Joe Zhou
; Date: 7/2/04
;
CLK 1 9.663E6
CLK 2 6.874E6
CLK 3 5.950E6
CLK 4 5.422E6
CLK 5 5.062E6
CLK 6 4.725E6
CLK 7 4.483E6
CLK 8 4.286E6
CLK 9 4.121E6
CLK 10 3.979E6
CLK 11 3.857E6
CLK 12 3.749E6
CLK 13 3.711E6
CLK 14 3.606E6
CLK 15 3.514E6
CLK 16 3.432E6

; Clock file: AXIALKB
; for ZEP7000A resist(11/00)
; 16 levels
; Generated by Joe Zhou
; Date: 7/2/01
;
CLK 1 3.357E6
CLK 2 3.292E6
CLK 3 3.232E6
CLK 4 3.178E6
CLK 5 3.138E6
CLK 6 3.100E6
CLK 7 3.065E6
CLK 8 3.032E6
CLK 9 3.001E6
CLK 10 2.972E6
CLK 11 2.944E6
CLK 12 2.919E6
```

```
CLK 13 2.891E6
CLK 14 2.838E6
CLK 15 2.789E6
CLK 16 2.742E6

; Clock file: AXIACKC
; for ZEP7000A resist(11/00)
; 16 levels
; Generated by Joe Zhou
; Date: 7/2/01
;
CLK 1 2.699E6
CLK 2 2.658E6
CLK 3 2.620E6
CLK 4 2.584E6
CLK 5 2.550E6
CLK 6 2.517E6
CLK 7 2.486E6
CLK 8 2.457E6
CLK 9 2.429E6
CLK 10 2.402E6
CLK 11 2.377E6
CLK 12 2.352E6
CLK 13 2.329E6
CLK 14 2.307E6
CLK 15 2.285E6
CLK 16 2.265E6
```

---The End---

References

1. G. J. Swanson and W. B. Veldkamp, "High-efficiency, multi-level diffractive optical elements," U.S. patent 4,895,790 (January 23, 1990)

2. G. J. Swanson, "Binary optics technology: theoretical limits on the diffraction efficiency of multi-level diffractive optical elements," Tech. Rep. 914 (MIT, Cambridge, Mass., 1991)

3. E. B. Kley, "Continuous profile writing by electron and optical lithography", Microelectronic Engineering, Vol. 34, 261-298 (1997)

4. W. Daschner, R. Stein, P. Long, C. Wu, and S. H. Lee, "One step lithography for mass production of multilevel diffractive optical elements using high energy beam sensitive (HEBS) gray-level mask", Proc. SPIE 2689, 153–155 (1996).

5. R. E. Fisher, B. T. Galeb and P. R. Yoder, "Optical system design", 2nd edition, McGraw-Hill (2008)

6. B. Kress and P. Meyrueis, "Digital Diffractive Optics: An Introduction to Planar Diffractive Optics and Related Technology", Wiley (2000)

7. D. Daly, R.F. Stevens, M.C. Hutley, N. Davies, "The manufacture of micro-lenses by melting photoresist", Meas. Sci Techn. 1, pp 759-766 (1990)

8. C. M. Waits, A. Modafe and R. Ghodssi, "Investigation of gray-scale technology for large area 3D silicon MEMS structures," J. Micromech. Microeng., vol. 13, pp. 170–177 (2003)

9. B. Morgan, C. M. Waits, J. Krizmanic and R. Ghodssi, "Development of a Deep Silicon Phase Fresnel Lens Using Gray-Scale Lithography and Deep Reactive Ion Etching", J. Microelectromechanical Systems, Vol. 13, No. 1, pp. 113–120 (2003)

10. Z. Zhou and S. H. Lee, "Fabrication of an improved gray-scale mask for refractive micro- and meso-optics", Optics Letters, Vol. 29, No. 5, 457-458 (2004)

11. J. D. Rogers, A. H. O. Kärkkäinen, T.Tkaczyk, J. T. Rantala and M. R. Descour, "Realization of refractive micro-optics through grayscale lithographic patterning of photosensitive hybrid glass", Optics Express, Vol. 12, No. 7, 1294-1303 (2004)

12. M.T. Gale, G. K. Lang, J. M. Raynor and H. Schutz, “Fabrication of micro-optical elements by laser beam writing in photoresist”, Proc. SPIE 1506, 65-70 (1991)

13. V. P. Korolkov, R. K. Nasyrov and R. V. Shimansky, "Zone-boundary optimization for direct laser writing of continuous-relief diffractive optical elements," Appl. Opt. 45, 53-62 (2006)

14. M. Teschke, R. Heyer, M. Fritzsche, S. Stoebenau and S. Sinzinger, “Application of an interferometric phase contrast method to fabricate arbitrary diffractive optical elements”, Appl. Opt. 47, No. 14, 2550 (2008)

15. L. Mosher, C. M. Waits, B. Morgan and R. Ghodssi, “Double-Exposure Grayscale Photolithography”, J. Microelectromech. Syst., vol. 18, 308-315, 2008.

16. L. Jiang, P. Nath and N. S. Korivi, “Arbitrary three-dimensional micro-fabrication by polymer grayscale lithography”, Proc. SPIE, Vol. 7274, 72742L (2009)

17. S. Akbar, E. Imhoff and F. Kub, “Gray-scale lithography of photosensitive polyimide and its graphitization”, Proc. SPIE, Vol. 6519, 65191I (2007)

18. T. Dillon, M. Zablocki, J. Murakowski and D. Prather, “Processing and modeling optimization for gray-scale lithography”, Proc. SPIE, Vol. 6923, 69233B (2008)

19. B. Morgan, X. Hua, T. Iguchi, T. Tomioka, G. S. Oehrlein and R. Ghodssi, “Substrate interconnect technologies for 3-D MEMS packaging”, Microelec. Eng. 81, 106–116 (2005)

20. B. Morgan, J McGee and R. Ghodssi, “Automated Two-Axes Optical Fiber Alignment Using Grayscale Technology”, J. Microelectromech. Syst., vol. 16, 102–110 (2006)

21. Y. Yamanishi, S. Sakuma, Y. Kihara and F. Arai, “Fabrication and Application of 3D Magnetically Driven Microtools”, IEEE Transactions on Mechatronics, to be published (2009)

22. M. LeCompte, X. Gao and D. W. Prather, “Photoresist characterization and linearization procedure for the gray-scale fabrication of diffractive optical elements”, Applied Optics, Vol. 40 (32), pp.5921-5927 (2001)

23. A. Kovalskiy, M. Vlcek, H. Jain, A. Fiserova, C.M. Waits and M. Dubey, “Development of chalcogenide glass photoresists for gray scale lithography”, Journal of Non-Crystalline Solids, 352, 589–594 (2006)

24. W. Daschner, P. Long, R. Stein, C. Wu, and S. H. Lee, “Cost-effective mass fabrication of multilevel diffractive optical elements by use of a single optical exposure with a gray-scale mask on high-energy beam-sensitive glass”, Appl. Opt. 36, 4675 (1997)

25. W. Daschner, P. Long, R. Stein, C. Wu, and S. H. Lee, “General aspheric refractive micro-optics fabricated by optical lithography using a high energy beam sensitive glass gray-level mask”, J. Vac. Sci. Technol. B 14**,** 3730 (1996)

26. C. Wu, “Method of making high energy beam sensitive glass,” U.S. patent 5,078,771 (January 7, 1992)

27. “Properties of HEBS-Glass,” (Canyon Materials, Inc., San Diego, Calif.), retrieved March 10, 2003, http://www.canyonmaterials.com/prop_hebs1.html

28. M. R. Wang and H. Su, “Multilevel diffractive micro-lens fabrication by one-step laser-assisted chemical etching upon high-energy-beam sensitive glass”, Opt. Lett. **23,** 876 (1998)

29. E. B. Kley, M. Cumme, L. C. Wittig, and C. Wu, “Adapting existing e-beam writers to write HEBS-glass gray-scale masks”, Proc. SPIE **3633,** 35 (1999).

30. C. Gimkiewicz, D. Hagedorn, J. Jahns, E. B. Kley, and F. Thoma, “Fabrication of microprisms for planar optical interconnections by use of analog gray-scale lithography with high-energy-beam–sensitive glass”, Appl. Opt. **38,** 2986 (1999)

31. S. H. Lee, M. S. Jin, and M. L. Scott, “Method for fabricating continuous space variant attenuating lithography mask for fabrication of devices with three-dimensional structures and microelectronics,” U.S. patent 6,534,221 (March 18, 2003)

32. Z. Zhou and S. H. Lee, “Two-beam-current method for e-beam writing gray-scale masks and its application to high-resolution micro-structures”, Applied Optics, Vol. 47 (17), pp.3177-3184 (2008)

33. Leica VB Parameter Calculator, http://www.research.ibm.com/people/r/rooks/calc.html

34. B. G. Eynon and J. B. Wu, “Photomask Fabrication Technology”, McGraw-Hill Companies, Inc., the USA, 2005

35. G. J. Swanson, “Binary optics technology: theoretical limits on the diffraction efficiency of multi-level diffractive optical elements,” Tech. Rep. 914 (MIT, Cambridge, Mass., 1991)

36. Trion technical papers, http://www.triontech.com/techPapers/ICPSource.html

37. B. Bhushan and X. Li, “Micromechanical and tribological characterization of doped single-crystal silicon and polysilicon films for microelectromechanical systems devices”, J. mater. Res., Vol.12, No.1, 54-63(1997)

38. X. Xiao, K. K. Goel, J. C. Sturm and P. V.Schwartz, “Data transmission at 1.3 micron using silicon spatial light modulator”, Proceedings of SPIE, Optical technology for microwave applications V, Vol. 1476, 301-304(1991)

39. W. B. Rayton, “The practical application of parabolic surfaces in lens construction”, J. O. S. A. & R. S. I., VII, 197-202 (February, 1923)

40. J. Mukai, Y. Matsui, and I. Harumoto, "Effects of aspheric surfaces on optical performance and their application to lenses for 35mm Cinematography," J. SMPTE 88, 542-545 (1979)

41. W. J. Smith, Modern optical engineering, 3rd ed., McGraw-Hill (2000)

42. W. Smith, Modern Lens Design, McGraw-Hill (2005)

43. H.H. Barrett and S.F. Jacobs, "Retro-reflective Arrays as Approximate Phase Conjugators," Optics Letters, Vol. **4**, pp. 190-192 (1979)

44. US Naval Research Laboratory, http://mrr.nrl.navy.mil/

45. H. Holden and R. Charbonneau, “Predicting HDI design density” Circuit World, Vol. 26, No. 4, pp. 22-25 (2000)

46. J. D. Plummer, M. Deal and P. B. Griffin, “Silicon VLSI Technology (Fundamentals, Practice and Modeling)”, Prentice Hall, 2000

47. J. Karttunen, J. Kiihamäki and S. Franssila, “Loading effects in deep silicon etching”, Proceedings of SPIE. Vol. 4174, pp. 90–97 (2000)

48. E. W. Becker, W. Ehrfeld, G. Krieg, and W. Bier, "Method for producing seperating nozzle elements," US Patent 4,351,653, 1982.

49. J. Mohr, P. Bley, M. Strohrmann, and U. Wallrabe, "Microactuators fabricated by the LIGA process", Journal of Micromechanics and Microengineering, 2, 234-241 (1992)

50. C. H. Ho, K. P. Chin, C. R. Yang, H. M. Wu and S. L. Chen, "Ultrathick SU-8 mold formation and removal, and its application to the fabrication of LIGA-like micromotors with embedded roots", Sensors and Actuators, A102 130–138 (2002)

51. S. Y. Luo, T. H. Yu and Y. C. Hu, "Fabrication of micro nickel/diamond abrasive pellet array lapping tools using a LIGA-like technology", J. Micromech. Microeng., 17, 1130–1138 (2007)

52. Q. Wang, Y. Duan, Y. Ding, B. Lu, J. Xiang and L. Yang, "Investigation on LIGA-like process based on multilevel imprint lithography", Microelectronics Journal, 40 149–155 (2009)

53. J. J. Yang, Y. S. Liao and C. F. Chen, "Eight-Phase-Level Diffractive Microlens for Beam Splitting Using LIGA-Like Process", Jpn. J. Appl. Phys., Vol. 45, 2817–2823 (2006)

54. Y. C. Lee, C. M. Chen and C. Y. Wu, "Spherical and Aspheric Microlenses Fabricated by Excimer Laser LIGA-like Process", Journal of Manufacturing Science and Engineering, Vol. 129, 126-134 (2007)

55. J. U. Nockel, A. D. Stone and R. K. Chang, "Q spoiling and directionality in deformed ring cavities", Opt. Lett. 19, 1693-1695 (1994)

56. J. U. Nockel and A. D. Stone, "Chaotic Light: A Theory of Resonant Asymmetric Cavities, Optical Processes in Microcavities", edited by R. K. Chang and A. J. Campillo (World Scientific, Singapore, 1996).

57. F. Laermer and A. Urban, "Challenges, developments and applications of silicon deep reactive ion etching", Microelectronic Engineering, Vol. 67–68, pp. 349–355 (2003)

58. J. Ishikawa, H. Tsuji, K. Shibutani, H. Ikai and Y. Gotoh, "Comparison of Silicon Etching Properties between F- Negative Ion and SF_3^+ Positive Ion-Beam Etchings", Proceedings of IEEE 1998 International Conference on Ion Implantation Technology, Volume: 2, pp. 716-719 (1998)

59. P. Kleimann, J. Linnros and R. Juhasz, "Formation of three-dimensional microstructures by electrochemical etching of silicon", Appl. Phys. Lett., Vol. 79(11), 1727 (2001)

60. A. Chelnokov, S. David, K. Wang, F. Marty and JM. Lourtioz, "Fabrication of 2D and 3D silicon photonic crystals by deep etching", IEEE Journal of Selected Topics in Quantum Electronics, Vol.8 , No. 4, pp. 919 – 927 (2002)

61. M. J. de Boer, J. G. E. Gardeniers, H. V. Jansen, E. Smulders, M. J. Gilde, G. Roelofs, J. N. Sasserath, M. Elwenspoek, "Guidelines for etching silicon MEMS structures using fluorine high-density plasmas at cryogenic temperatures", IEEE/ASME Journal of Microelectromechanical Systems, Vol.11 No. 4, pp. 385-401 (2002)

62. C. W. Waits, B. Morgan, M. Kastantin and R. Ghodssi, "Microfabrication of 3D silicon MEMS structures using gray-scale lithography and deep reactive ion etching", Sensors and Actuators, A 119, 245–253 (2005)

63. J. W. Bartha, J. Greschner, M. Puech and P. Maquin, "Low temperature etching of Si in high density plasma using SF_6/O_2", Microelec. Eng. 27, 453-456 (1995)

64. R. Legtenberg, H. Jansen, M. Boer and M. Elwenspoek, "Anisotrapic Reactive Ion Etching of Silicon Using $SF_6/O_2/CHF_3$ Gas Mixtures", J. Electrochem. Sac., 142, 2020-2028 (1995)

65. I. W. Rangelow and H. Loschner, "Reactive ion etching for microelectrical mechanical system fabrication", J. Vac. Sci. Technol. B 13, 2394-2399 (1995)

66. H. C. Liu, Y. H. Lin and W. Hsu, "Sidewall roughness control in advanced silicon etch process", Microsystem Technologies, 10, 29–34 (2003)

67. T. Lagarde, J. Pelletier and Y. Arnal, "Parametric study of the etching of SiO_2 in SF_6 plasmas: Modeling of the etching kinetics and validation", J. Vac. Sci. Technol., B17, 118-126 (1999)

68. S. K. Ray, C. K. Maiti and S. K. Lahiri, "Chemically Assisted Ion Beam Etching of Silicon and Silicon Dioxide Using SF_6", Plasma Chemistry and Plasma Processing, Vol. 15, 711-720 (1995)

69. S. L. Lai, D. Johnson and R. Westerman, "Aspect ratio dependent etching lag reduction in deep silicon etch processes", J. Vac. Sci. Technol. A24, 1283-1288 (2006)

70. B. Bai, J. An and H. H. Sawin, "Silicon and silicon oxide etching rate enhancement by nitrogen containing gas addition in remote perfluorocarbon plasmas", Appl. Phys. Lett. 88, 101504 (2006)

71. B. E. E. Kastenmeier, P. J. Matsuo and G. S. Oehrlein, "Highly Selective Etching of Silicon Nitride Over Silicon and Silicon Dioxide", J. Vac. Sci. Technol. A, 17(6), pp. 3179-3184 (1999)

72. D. Zhang, S. Rauf, T. G. Sparks and P. L. G. Ventzek, “Integrated equipment-feature modeling investigation of fluorocarbon plasma etching of SiO2 and photoresist”, Journal of Vacuum Science & Technology B: Microelectronics and Nanometer Structures, Vol. 21(2), pp. 828-836 (2003)

73. C. Reyes-Betanzo, S. A. Moshkalyov, J. W. Swart and A. C. S. Ramos, “Silicon nitride etching in high- and low-density plasmas using SF6/O2/N2 mixtures”, J. Vac. Sci. Technol. A, Vol. 21, No. 2, pp. 461-469 (2003)